Active Sensing and Repair Composites

THÈSE N^{O} 4409 (2009)

PRÉSENTÉE LE 5 JUIN 2009

À LA FACULTÉ SCIENCES ET TECHNIQUES DE L'INGÉNIEUR
LABORATOIRE DE TECHNOLOGIE DES COMPOSITES ET POLYMÈRES
PROGRAMME DOCTORAL EN SCIENCE ET GÉNIE DES MATÉRIAUX

ÉCOLE POLYTECHNIQUE FÉDÉRALE DE LAUSANNE

POUR L'OBTENTION DU GRADE DE DOCTEUR ÈS SCIENCES

PAR

Eva KIRKBY

acceptée sur proposition du jury:

Prof. C. Hébert, présidente du jury
Prof. J.-A. Månson, Dr V. Michaud, directeurs de thèse
Dr I. Bond, rapporteur
Dr K. Nelson, rapporteur
Prof. R. Salathé, rapporteur

ÉCOLE POLYTECHNIQUE
FÉDÉRALE DE LAUSANNE
Suisse
2009

Abstract

This thesis describes the development of a smart carbon fibre polymer composite that is capable of sensing its own damage and self-healing. Structural composites are used in the aerospace and marine industries, for example. During their lifetime impact events are inevitable, which can result in extensive internal damage. Once damaged, the only options to date are manual repair or replacement. If self-sensing and self-healing properties could be imparted to the next generation of structural composites, this would bring greater safety and reduced maintenance costs for aircraft, as well as an extended operational lifetime for equipment such as satellites.

The concept of the new material is to embed three additional components into a fibre-reinforced composite material: (i) microcapsules containing a liquid healing agent, together with a solid catalyst in the matrix, (ii) optical fibre Bragg grating (FBG) strain sensors and (iii) woven shape memory alloy (SMA) wire actuators. An impact event causes a crack to propagate at the damage site, rupturing the microcapsules in its path. This releases the liquid healing agent into the crack, where it comes into contact with the catalyst and begins to polymerise. The strain shock pulse radiating out from the impact site is detected by a sparse array of FBG sensors, which locate the impact position by time-of-flight. With this information, the SMA wires in the impact region are thermally activated using resistive heating, causing them to contract and exert a compressive force, closing the crack. The SMA wires then remain activated during the polymerisation period of the healing agent.

The new material is developed in several stages. In the first stage, SMA wires and microcapsules are combined in an epoxy matrix. The addition of SMA wires results in a significant improvement in healing efficiency; the healed fracture toughness approaches that of the virgin material. The improvement results both from crack-closure and also from the heating effect of the wires, which increases the degree of polymerisation of the healing agent. In the second stage, a liquid composite moulding cure schedule that allows straightforward integration of the SMA wires during composite fabrication is developed. With this process, the SMA wires do not need to be maintained in place with an external frame, even though the peak post-cure temperature exceeds the activation temperature of the wires. The wires remain bonded to the matrix both during processing and subsequent activation. In the third stage, impact sites are localised on composite plates to a precision of a few centimetres using three FBG sensors spaced several tens of centimetres apart. In the final stage, a prototype self-healing carbon-fibre composite with embedded microcapsules, Grubbs' catalyst and woven SMA wires is fabricated and tested.

While the results presented in this thesis represent only a first step towards a fully-functional Active Sensing and Repair Composite, they successfully demonstrate the advantages of combining the three components in a single material, as well as validate the scientific concept of the system.

Keywords: smart material, self-healing, self-sensing, microcapsule, shape memory alloy wire actuator, fibre Bragg grating sensor.

Version abregée

Cette thèse présente le développement d'un matériau composite intelligent, capable de détecter son endommagement et de s'auto réparer. Les composites structurels sont utilisés dans les industries aérospatiale et maritimes, par exemple. Au cours de leur utilisation, des impacts sont inévitables, et peuvent créer des dégâts internes. Une fois que ceci c'est produit, les seuls options sont la réparation manuelle ou le remplacement de la pièce. Si des propriétés d'auto-détection et d'auto-réparation pouvaient être incorporées dans une nouvelle génération de composites, cela permettrait d'apporter plus de sécurité et de réduire les coûts de maintenance des avions, ainsi que de prolonger la vie opérationnelle d'équipements tels que les satellites.

Le concept présenté dans ce travail est d'incorporer trois composants supplémentaires dans un matériau composite structurel : (i) des microbilles contenant un agent réparateur, et un catalyseur, dans la matrice, (ii) des fibres optiques avec réseau de Bragg (FBG) et (iii) des fils tissés d'alliage à mémoire de forme (AMF). A la suite d'un impact, une fissure se propage à ce site, ce qui casse les microbilles se situant dans son chemin. L'agent réparateur s'écoule alors depuis les microbilles dans la fissure, où il entre en contact avec le catalyseur, et peut commencer à polymériser. En parallèle, l'onde qui se propage dans la pièce depuis le site de l'impact est détectée par un réseau de capteurs FBG, qui localisent l'impact par des mesures de temps de vol. Avec cette information, on peut alors activer thermiquement par effet Joule les fils d'alliages à mémoire de forme déformés qui se situent dans la zone d'impact. Lors du passage de leur température d'activation, les fils se contractent, refermant la fissure. Les fils restent actifs et exercent une force de fermeture sur la fissure pendant la durée de polymérisation de l'agent réparateur.

Ce nouveau matériau est développé en plusieurs étapes. Dans la première, les fils AMF et les microbilles sont intégrés dans une matrice époxy. Il est montré que l'addition des fils augmente l'efficacité de réparation; la ténacité du matériau réparé s'approche de celle du matériau d'origine. L'amélioration provient de la fermeture de la fissure, et aussi du fait de chauffer les fils, ce qui augmente le degré de polymérisation de l'agent réparateur. Dans la deuxième étape, un cycle de post-cuisson permettant l'intégration des fils AMF dans un matériau composite est déterminé. Avec ce type de cuisson, le besoin d'utiliser un cadre externe pour maintenir les fils en place est éliminé, même si la température maximale de post-cuisson est bien au-delà de la temprature d'activation des fils. Les fils restent liés à la matrice pendant toute la fabrication, ainsi que lors de leur activation. Dans la troisième tape, on a développé la méthode de détection et de localisation des impacts dans une plaque composite avec un réseau de capteurs FBG, placés a plusieurs dizaines de centimètres l'un de l'autre. La localisation se fait alors avec une précision de quelques centimètres. L'étape finale consiste à fabriquer et tester le concept global, avec des prototypes de composites auto réparant, contenant des microbilles, du catalyseur et des fils AMF tissés.

Les résultats présentés dans cette thèse constituent un premier pas vers un matériau qui peut détecter, localiser et réparer des impacts de manière autonome. Ils démontrent les avantages d'incorporer ces trois composants dans un matériau, tout en proposant des solutions de mise en oeuvre et en validant le concept scientifique du matériau.

Mots clés: matériau intelligent, auto-réparation, auto-détection, microbille, fil d'alliage a mémoire de forme, fibre optique avec capteur de Bragg.

Acknowledgements

Although I was the one who had the task of putting pen to paper and writing this thesis, it would not have seen the light of day without the help and contributions of many. In particular, I would like to express my gratitude to Prof Jan-Anders Månson, my thesis director, for giving me the opportunity to complete this work in his laboratory, and for his sustained support. I would also like to especially thank Dr. Véronique Michaud, my thesis supervisor, for giving me sufficient freedom in my research, for her enthusiasm, and for always being available for discussions and guidance.

Without the collaboration with the Autonomic Materials Systems Group, headed by Prof. Scott White, at the University of Illinois at Urbana-Champaign, no doubt I'd still be in the lab trying to make microcapsules. Thank you all for welcoming me for three months, for the help and effort that followed, and for the fruitful collaboration.

Due to the interdisciplinary nature of my thesis, I often found myself trawling the EPFL website in search of expert advice. I was continually impressed by the willingness of people to help. Thank you to all of you, be it for training me on or loaning me laboratory equipment, allowing me to use the facilities in your laboratory, or discussions in the corridor and over coffee. Thank you also to the workshop at the IMX, and to Prof. Jean-Pascal Reymondin at the Haute Ecole d'Ingénierie et de Gestion du Canton de Vaud.

I would especially like to thank the members of the Laboratory of Composite and Polymer Technology, who have made the four years I have spent there enjoyable, both on a professional and a personal level. Thank you to Rui for putting up with me, and for actually teaching me some useful stuff. I'd like to express my gratitude to Seb and Fabio. And naturally thank you to Claire, for taking time out of her day to baby-sit me at the scanning electron microscope. It was also a pleasure to supervise Lucien Germond, Michael Stuer and Douglas Watson in their undergraduate projects, and of Julie O'Keane in her Master's thesis.

Many thanks are extended to my thesis committee: Prof. Jan-Anders Månson, Dr. Véronique Michaud, Prof. René Salathé, Dr. Ian Bond and Dr. Karl Nelson.

All my fantastic friends in Geneva and elsewhere in the world: here's to you.

Finally, love to my dear Mum, Dad and Lowry, my sister, who are truly incredible, who make me proud, and who also know how a few words on the end of a page would not do justice to all they bring to my life.

This research was made possible by the financial support of the Swiss National Science Foundation (contract no. 200020-1-5169).

Contents

List of Figures

List of Tables

List of symbols

Symbol	Quantity
a	compact tension sample pre-crack length
a	wire radius
A	TDCB sample crack area
A_0	amplitude
A_f	austenite finish temperature
A_{ij}	in-plane stiffness
A_s	austenite start temperature
b	effective radius
b	three-point bend sample beam width
B	compact tension sample width
c_e	extensional mode group velocity
c_f	flexural mode group velocity
d	three-point bend sample beam thickness
d_c	microcapsule diameter
d_f	fibre diameter
D	three-point bend sample deflection
D_h	amount of DCPD delivered per unit crack area
D_{ij}	bending stiffness
E, E'	Young's modulus, elastic modulus
E''	visco-elastic modulus
E_f	fibre Young's modulus
E_m	matrix Young's modulus
f	linear frequency
F_d	pull-out test debond force
F_r	restoration force
F_s	activation force
F_u	force felt by U-holder
G'	elastic shear modulus
G''	viscous shear modulus
h	sample thickness
ΔH_a	heat of austenitic transformation
ΔH_m	heat of martensitic transformation
k	wavenumber

Symbol	Quantity
k	U-holder spring constant
K	contribution of internal thermoelastic stresses to intrinsic interfacial shear strength
K_{IC}	fracture toughness
K_{IC_v}	virgin fracture toughness
K_{IC_h}	healed fracture toughness
l_e, l_{emb}	embedded wire length
l_0	original sample length
L	three-point bend sample support span
M_f	martensite finish temperature
M_s	martensite start temperature
n	effective refractive index
p_e	strain-optic tensor
p_{11}, p_{22}	strain-optic coefficients
P_C	critical fracture load
P_{C_v}	virgin fracture load
P_{C_h}	healed fracture load
Q_{ij}	elastic stiffness coefficients
r_f	fibre radius
S	three-point bend sample maximum fibre stress
t	time
T	temperature
T_g	glass transition temperature
V_c	volume of healed TDCB crack
V_f	fibre volume fraction
V_h	volume of healing agent delivered
V_m	matrix volume fraction
w	TDCB crack face separation
W	compact tension sample distance between loading slot and back of sample
u	displacement in the x-direction
v	displacement in the y-direction
w	displacement in the z-direction
α	geometric term for TDCB fracture toughness
α	thermal expansion coefficient
α	term accounting for the cylindrical geometry of a wire in the pull-out test
α_f	fibre thermal expansion coefficient
α_i	particle direction cosines
α_m	matrix thermal expansion coefficient
ϵ	strain
ϵ_f	flexural strain

Symbol	Quantity
ϵ_u	U-holder strain
η	viscosity
η	TDCB healing efficiency
γ	fill factor of DCPD
λ_B	Bragg wavelength
$\Delta\lambda_B$	shift in Bragg wavelength
Λ	Bragg grating pitch
ν, ν_{ij}	Poisson ratio
ν_m	matrix Poisson ratio
ξ	thermo-optic coefficient
ρ	density
ρ_h	DCPD density
ρ_s	TDCB matrix density
σ	stress; recovery stress
σ_{act}	stress due to SMA activation
σ_i	stress due to thermal contractions
σ_p	stress due to SMA wire prestrain
τ	interfacial shear stress
τ_{exp}	experimental interfacial shear strength
τ_i	intrinsic interfacial shear strength
ϕ	microcapsule weight fraction
ω	angular frequency

Chapter 1

Introduction

1.1 Motivation

Composite materials have been developed over the last 40 years to meet the need for high-performance materials that are strong and light. These can have a tensile strength comparable to mild steel, yet have about half the density of aluminium [1, 2]. They are widely used in the aerospace, automotive, marine and sports industries, for example, due to their capacity to withstand harsh loading conditions. For instance, the new Boeing 787 Dreamliner is composed of about 50 % composite materials, including the wings and the fuselage [3]. Due to the ever-increasing demands on these materials, however, it is no longer sufficient simply to make incremental improvements in their properties. Recently, therefore, interest has focused on developing new composites with added functionality—so-called smart composites—with embedded sensors and actuators, controlled by microprocessors. The research presented in this thesis concerns the development of one such smart composite material.

While composites have a high specific strength and stiffness in the direction of the reinforcing fibres, they have relatively poor properties in the transverse direction, with notably low resistance to impact, due to their anisotropic nature. Impact events are inevitable during the lifetime of a composite structure, occurring during both service and maintenance, in the form of collisions. Such events can cause extensive internal delaminations, where two adjacent laminas become de-bonded. This damage, while often difficult or even impossible to detect at the surface of the material, severely degrades the load-bearing capacity of the structure, which eventually either wears out or fails as a result. Once this has occurred the only options at present are manual repair or replacement.

In stark contrast with the progressive degradation of engineering materials over time, the materials of living organisms have the ability to detect their own mechanical damage—such as a skin abrasion or a bone fracture—and to self-heal. This unique regenerative property allows a living organism to recover from injuries, greatly extending its lifetime. If analogous *in situ* self-sensing and self-healing capabilities could be provided for composite structures, there would be many potential uses. Although commercial applications for self-healing materials are still many years away, the first would likely be in the aerospace sector. Aircraft fuselage and wings are susceptible to impacts from birds, rocks or hailstones, and the ability to actively sense damage and self-repair in-flight would bring an additional safety

margin. Furthermore, it would lead to cost savings through both reduced maintenance time and increased component lifetime. In the case of satellites, structural repair of damage after launch is presently not possible. Composite panels that could self-repair after impacts with small meteorites could significantly extend the operational lifetime of the valuable equipment on board the satellite. Sports equipment manufacturers could also be early users of this technology, for example in applications involving critical composite structures such as masts. Materials for sports equipment are often operated close to their failure limit to provide the highest possible performance-to-weight ratio. A material that can sense its own damage and self-repair could provide a competitive edge by being operated with an even smaller tolerance to failure.

1.2 Concept

The work presented here concerns the development of a novel smart material—an Active Sensing and Repair Composite (ASRC; Fig. 1.1)—with the ability to detect and locate its own damage, and subsequently self-heal. The new material comprises a carbon fibre reinforced polymer composite with three additional components embedded in the matrix:

1. **Microcapsules containing a liquid healing agent, together with a solid catalyst**, both dispersed in the polymer matrix, to effect the repair. A crack formed by a damage event ruptures the capsules in its path. The healing agent is subsequently released and exposed to the catalyst, causing it to polymerise.

2. **Fibre Bragg grating (FBG) strain sensors** to locate the damage site. Upon impact, a strain shock pulse radiates from the site and is detected by several sensors. Precise ($\sim$1 μs) measurement of the arrival time of the shock pulse at each sensor allows the damage site to be located by time-of-flight.

3. **Shape memory alloy (SMA) wire actuators** to close the cracks at the damage site during the polymerisation period of the healing agent, to maximise healing efficiency.

White *et al.* have pioneered self-repairing materials involving liquid healing agent enclosed in microcapsules [4]. Their studies have typically involved microcapsule diameters of 100–200 μm, and loading fractions in the matrix of about 10–20 wt%. Recently, Rule *et al.* have found that the material's ability to heal substantially deteriorates at low microcapsule sizes and concentrations, due to the failure to completely fill the crack volume with healing agent [5]. A technique is, therefore, required to reduce the crack size during the healing period of the material, to allow the entire crack to be filled with healing agent. Such a process would in turn allow capsule size and loading fraction to be further reduced. There is considerable interest to do so because the smallest cracks that can be repaired are set by the microcapsule size, meaning further reductions would allow the repair of correspondingly smaller microcracks. Furthermore, smaller microcapsules are necessary in materials where

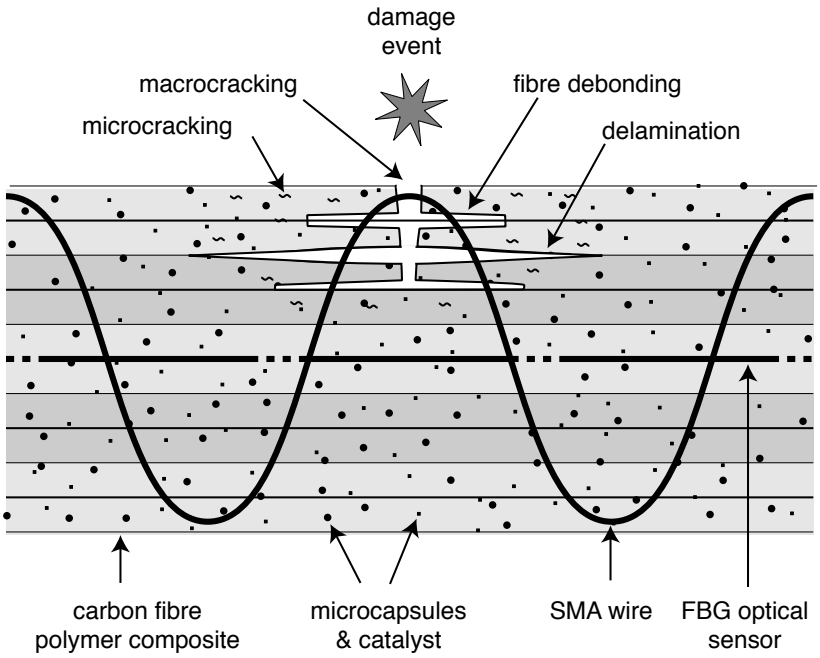

Figure 1.1: Schematic drawing of the Active Sensing and Repair Composite (ASRC), which combines three additional components within a fibre-reinforced polymer composite: (1) microcapsules containing a liquid healing agent, and a solid catalyst, both in the matrix, (2) fibre Bragg grating (FBG) strain sensors and (3) shape memory alloy (SMA) wire actuators. The vertical dimension of the drawing is exaggerated with respect to the horizontal dimension.

the characteristic dimensions are below 100 μm. Finally, this would allow for better processing, such as improved dispersion within the matrix, and would reduce the influence of the capsules on the final properties of the material.

Shape memory alloy (SMA) wires are well-suited to this application. They exhibit a thermoelastic martensitic phase transformation and, if initially prestrained or if they exhibit what is known as two-way shape memory, contract above their transformation temperature and exert large recovery stresses of up to 800 MPa when constrained at both ends [6]–[10]. The generation of recovery stresses in unembedded SMA wires is well-characterised. However, the use of embedded SMA wires, for example in an epoxy matrix, to close internal cracks is barely explored. Rogers *et al.* have shown that when an SMA wire is embedded within an epoxy matrix, the full recovery force acts at its free edges [11]. Therefore, an SMA wire bridging a crack should induce a large closure force on the crack.

The third component—the fibre Bragg grating (FBG) sensors—is a relatively new development for non-destructive structural health monitoring. FBGs are fibre optic strain sensors, capable of highly-sensitive measurements. They provide an attractive alternative to existing test methods such as tap testing, X-radiography, ultrasonic testing and acoustic microscopy, since they can be used to monitor the component while it is in service. Optical fibres typically have a diameter of 250 μm and can, therefore, be easily embedded within a composite without affecting its

structural integrity [12]–[15]. They are robust, lightweight, corrosion-resistant, have high maximum operating temperature, require no electrical power at the sensing point and are immune to electromagnetic interference, eliminating the need for electrical shielding [16]. In a conventional strain measurement with FBG sensors, the sampling rate is often limited to a few Hertz. However, strain pulses generated by impact events typically have frequencies of several tens or hundreds of kilo-Hertz, and travel at several thousand metres per second, meaning that the sampling rate needs to be substantially higher. In the present work, a simple and elegant read-out system that allows high-speed interrogation of the FBGs [17, 18] is implemented. The technique is used in a new manner, to create an array of high-speed sensors mounted on the surface of a composite plate. By precisely measuring the arrival time of the strain shock pulse at several FBG sensors, it should be possible to precisely determine the location of the impact. With this information, the SMA wires could be activated at the time of occurrence of the damage event and in the exact region where the damage occurred, to optimise the healing process.

To the author's knowledge, this work represents the first time that these three components are incorporated into a single composite material. Moreover, the components, in particular the shape memory alloy wires and the fibre Bragg grating sensors, are developed and implemented in relatively novel ways.

1.3 Thesis organisation

This thesis is organised as follows. A review of the related literature is given in Chapter 2. The materials used and their preparation are described in Chapter 3. The results are then presented in the subsequent chapters: Chapter 4—SMA wires are integrated in the self-healing polymer and their influence on the healing performance is evaluated; Chapter 5—a liquid composite moulding processing route is developed that is compatible with integration of both the SMA wires and the self-healing system in the epoxy matrix; Chapter 6—impacts on carbon fibre composite plates are remotely detected and located using a novel setup employing a sparse array of FBG sensors; Chapter 7—the microcapsule self-healing system and woven SMA wires are integrated in carbon-fibre composite samples and initial self-healing tests are carried out. Finally, the conclusions are presented in Chapter 8.

Chapter 2

State of the art

This chapter provides a review of the state of the art of the three technologies for the Active Sensing and Repair Composite: self-healing polymers, shape memory alloy wire actuators and fibre Bragg grating sensors.

2.1 Self-healing polymers

A number of self-healing techniques have been developed over the course of the last ten years. Comprehensive reviews are given in [19]–[25], for example. Broadly-speaking, self-healing techniques can be divided into those based on a liquid healing agent and those involving solid-state healing. The majority of research to date has been on liquid-based methods, which are the focus of this review. A short overview of solid-state healing, however, is also given.

2.1.1 Microcapsules

Concept

The first successful self-healing epoxy was developed by White *et al.* [4]. In their system, self-healing was achieved by embedding a micro-encapsulated healing agent (dicyclopentadiene – DCPD) [26] and a live catalyst (Grubbs' first generation catalyst) within an epoxy matrix (Fig. 2.1). Upon damage, a crack propagated through the material and ruptured the microcapsules along the fracture plane. Subsequently, the low-viscosity healing agent was released and covered the crack plane by capillary action. On contact with the catalyst, ring-opening metathesis polymerisation (ROMP) occurred and the crack was healed after 24 hr at ambient temperature. Microcapsules of the appropriate size and shell-wall thickness were found to be robust and did not rupture easily during manufacture; Keller and Sottos found that the urea-formaldehyde capsule walls had an average Young modulus of 3.7 GPa, and that a capsule with a diameter of 187 μm had a failure strength of 240 kPa [27]. Since the initial work, further developments of the microencapsulated self-healing system have lead to healing under dynamic loading [28]–[31], smaller capsule sizes [5, 32], improved catalysts [33, 34] and alternative self-healing chemistries [35]-[38], including systems where the healing agent was phase-separated in the epoxy matrix

[39], and where the microcapsules contained epoxy healing agent as an alternative to DCPD [40, 41].

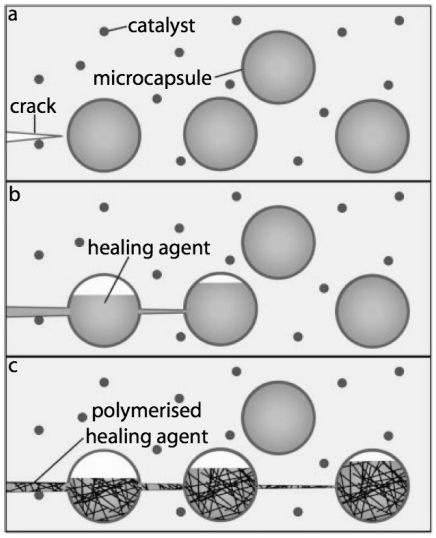

Figure 2.1: The self-healing mechanism [4]. The composite matrix contains a microencapsulated healing agent and a catalyst for its polymerisation. (a) A crack forms where damage occurs. (b) The path of a propagating crack is incident on a microcapsule, causing it to rupture and release healing agent into the crack. (c) The healing agent polymerises on contact with the catalyst.

Cure kinetics of dicyclopentadiene

DCPD exists as two stereo-isomers: endo- and exo-DCPD. Kessler *et al.* studied the cure kinetics of these two isomers with Grubbs' catalyst using differential scanning calorimetry (DSC) [42, 43]. Figure 2.2 shows their DSC measurements for (a) endo-DCPD and (b) exo-DCPD, respectively, reacted with a 'high' catalyst concentration of 2.67 mg ml^{-1}. Both reactions were highly exothermic due to the relief of ring strain. However, the endo-isomer exhibited a single exothermic peak, whereas the more reactive exo-isomer exhibited two. This difference was primarily due to stearic reasons [44]; the ROMP reaction occurs in two steps, and in the case of exo-DCPD the first of these two steps occurs more readily, leading to two distinguishable peaks (Fig. 2.2 b). Finally, they also observed that the activation energy of the reaction increased significantly after 60% cure, due probably to the decrease in molecular mobility at the gel point.

In understanding the reaction kinetics of the DCPD/Grubbs' catalyst ROMP reaction, and how variables such as catalyst concentration and temperature affect it, the cure rate can be optimised for a specific application. For example, Mauldin *et al.* showed that although the polymerisation rate of exo-DCPD with Grubbs' catalyst was 20 times faster than that of endo-DCPD, the final healing efficiency was lower [45]. This was because the rate of exo-DCPD polymerisation was much faster than the rate of Grubbs' catalyst dissolution. The catalyst, therefore, became encapsulated in cured DCPD, stopping the reaction prematurely.

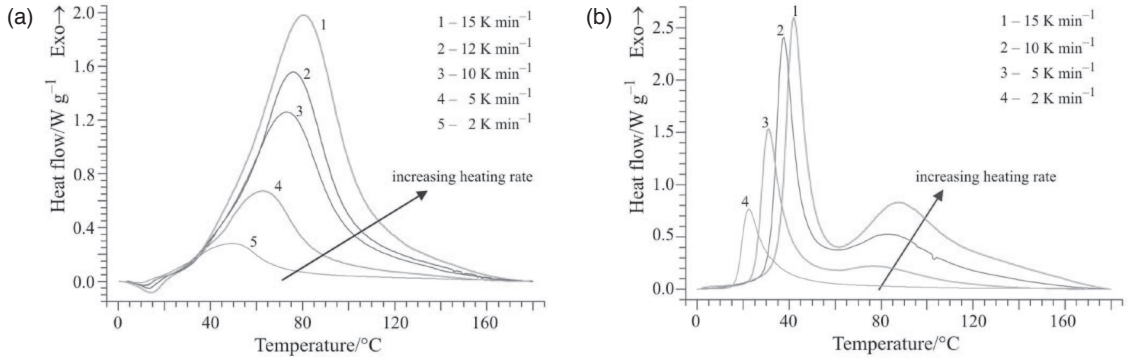

Figure 2.2: Differential scanning calorimetry curves for (a) endo-DCPD and (b) exo-DCPD polymerised with a Grubbs' catalyst concentration of 2.67 mg ml^{-1} [43].

Polymer/microcapsule samples

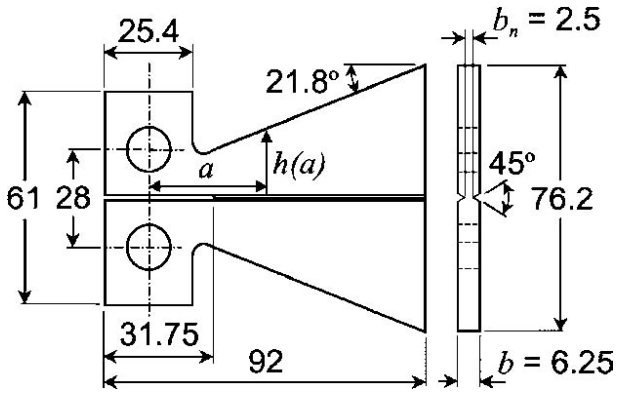

Figure 2.3: Tapered double cantilever beam sample geometry [46]. Dimensions are in mm.

The healing efficiency of the microcapsule system presented in [4] was assessed using a protocol based on measured plane strain fracture toughness (K_{IC}) values, established by White *et al.* [4]. The focus of their studies was the repair of fractured tapered double cantilever beam (TDCB) specimens [46, 47] (Fig. 2.3). The TDCB geometry, developed by Mostovoy *et al.* [48], provides a crack-length-independent measure of fracture toughness, K_{IC} (MPa m$^{1/2}$):

$$K_{IC} = \alpha P_C \tag{2.1}$$

where P_C (N) is the critical fracture load and α (m$^{-3/2}$) is an experimentally-determined geometric term. The efficiency of crack healing in static fracture was based on the ability of a healed sample to recover its K_{IC} fracture toughness. The healing efficiency (η) is given by

$$\eta = \frac{K_{IC_h}}{K_{IC_v}} = \frac{P_{C_h}}{P_{C_v}} \tag{2.2}$$

where K_{IC_v} and K_{IC_h} are the virgin and healed fracture toughness, respectively, and P_{C_v} and P_{C_h} are the virgin and healed peak loads prior to unstable fracture, respectively.

Brown *et al.* compared the fracture toughness of samples with microcapsule concentrations ranging between 5 and 20 wt% to that of neat epoxy samples [47]. The virgin fracture toughness of the epoxy was 0.55 ± 0.04 MPa m$^{1/2}$, and the epoxy specimens containing microcapsules yielded an average virgin fracture toughness that was 127% of this (Fig. 2.4). The virgin fracture toughness varied as a function of microcapsule concentration and diameter, with smaller microcapsules giving a maximum toughening effect at lower concentrations. Scanning electron microscope observations indicated that the source of this counter-intuitive result was a combination of localised plastic deformation and a crack-pinning toughening mechanism by the microcapsules [47]. After the virgin fracture test, the specimens were unloaded, externally clamped to close the crack, and allowed to heal for 24 hours, at which point they were re-tested. The healed fracture toughness increased steadily with microcapsule concentration to a plateau at about 20 wt% (Fig. 2.5), and the healing efficiency depended significantly on capsule diameter (Fig. 2.6).

Brown *et al.* also measured the evolution of the healing efficiency with time. Samples containing 10 wt% of 180 μm diameter capsules and 2.5 wt% of catalyst were tested at time intervals ranging from 10 min to 72 hr after the initial test (Fig. 2.7) [46]. A significant healing efficiency was obtained after about 25 min, corresponding closely with the gel time of the polyDCPD.

Rule *et al.* studied the influence of microcapsule size and concentration on the self-healing properties [5]. They performed tests with three different microcapsule diameters—65, 151 and 386 μm—as well as a control where a known amount of DCPD was manually injected into the crack. They found that the healed peak load for all samples followed the same curve (Fig. 2.8) which depended only on the amount of DCPD delivered per unit crack area, D_h (g cm^{-2}), given by,

$$D_h = \rho_s \, \phi \, d_c \tag{2.3}$$

where ρ_s is the density of the matrix (1.16 g cm^{-3}), ϕ is the weight fraction of microcapsules and d_c (cm) is the diameter of the microcapsules [5]. The healed peak load (Fig. 2.8) showed two main characteristics. Firstly, a plateau of about 38 N was achieved at large values of delivered DCPD, corresponding to a healing efficiency of around 50% compared to the virgin material. Secondly, at lower values of delivered DCPD (below 5 mg cm^{-2}) the healed peak load rapidly decreased. The onset of this reduced performance occurred when the total crack volume exceeded the volume of healing agent delivered, resulting in only partial crack filling.

Fibre-reinforced polymer composite/microcapsule samples

Kessler *et al.* performed self-healing tests on a fibre-reinforced polymer matrix composite [49, 50]. Three types of sample were prepared with a double cantilever beam (DCB) geometry. These were referred to as *reference* and *self-activated* composites, which were experimental controls involving manual injection, and *self-healing* composites, in which healing was autonomic (Fig. 2.9). The reference specimens represented ideal mixing of the catalyst and the healing agent, and so defined the

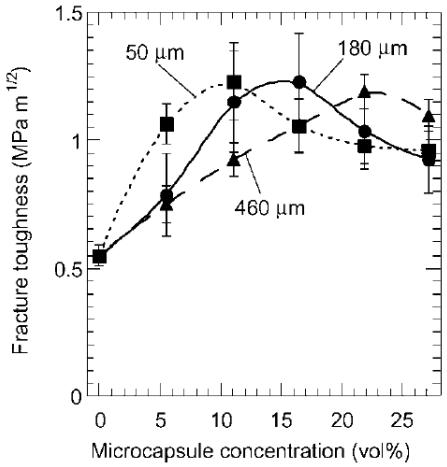

Figure 2.4: Virgin fracture toughness for epoxy with embedded microcapsules [47].

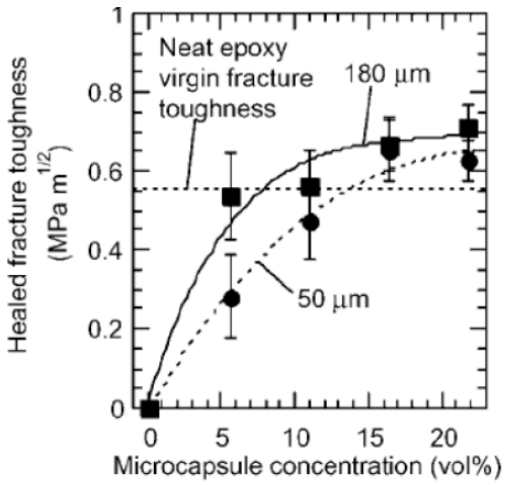

Figure 2.5: Healed fracture toughness after 24 hr for epoxy with embedded microcapsules [47].

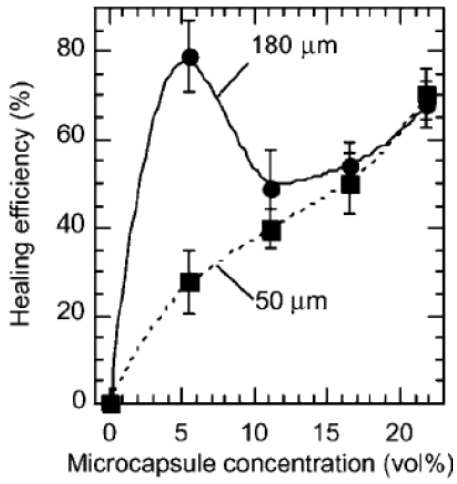

Figure 2.6: Healing efficiency (Eq. 2.2) after 24 hrs for epoxy with embedded microcapsules [47].

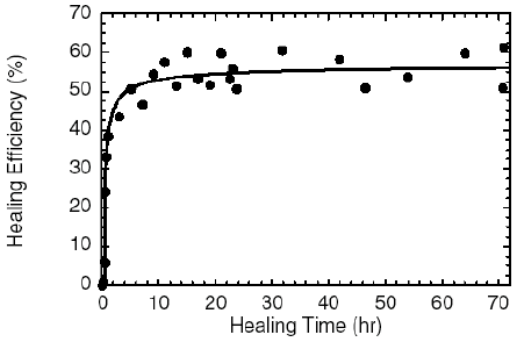

Figure 2.7: Evolution of the room temperature healing efficiency with time [46].

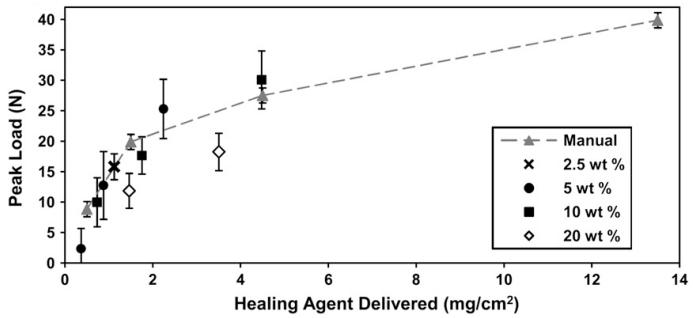

Figure 2.8: The average peak force required to fracture healed TDCB samples [5].

upper limit of the healing efficiency. The self-activated specimens were a control, confirming the embedded catalyst was still active after processing the composite. All specimens were fractured and allowed to heal for 48 hours, whilst externally clamped closed. The measured healed fracture toughnesses are summarised in Table. 2.1. The self-activated specimens had a lower average healing efficiency than both of the reference specimens, due to non-ideal mixing in the crack. The healing efficiency was increased substantially upon heating, due to both an increased rate of polymerisation and degree of polymerisation of the healing agent.

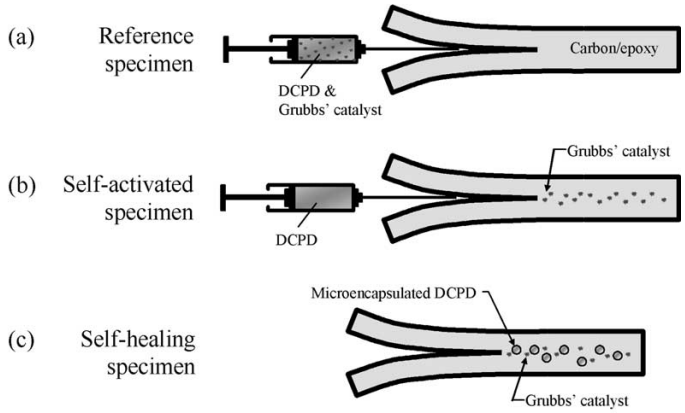

Figure 2.9: The three types of DCB test specimens used by Kessler *et al.* [50]. (a) reference specimen: the healing agent was manually mixed with catalyst and then injected into the crack; (b) self-activated specimen: the catalyst was embedded in the epoxy and the healing agent was manually injected; (c) self-healing specimen: both the catalyst and the microencapsulated healing agent were embedded within the epoxy.

Table 2.1: Summary of the healing efficiencies for self-healing composite DCB samples [50].

Specimen type	K_{IC} virgin ave. [MPa $m^{1/2}$]	K_{IC} healed ave. [MPa $m^{1/2}$]	K_{IC} healed max. [MPa $m^{1/2}$]	η ave. [%]	η max. [%]
Reference	3.58	3.54	3.82	99	107
Self-activated	2.54	1.86	2.09	73	82
Self-healing (25°C)	2.85	1.08	1.29	38	45
Self-healing (80°C)	2.79	1.83	2.23	66	80

2.1.2 Hollow glass fibres

Following some initial work by Dry [51] and Dry and Sottos [52], Bond *et al.* developed another approach to self-heal composite samples. They used hollow glass fibres infused with either healing agent or curing agent (Cycom 823 two-part system) [53]–[56]. These fibres had an outer and inner diameter of 60 μm and 45 μm, respectively, and were placed at critical damage interfaces in a carbon or glass fibre composite.

When the composite was impacted, the healing fibres ruptured, releasing the healing agent into the damage zone. The healing resin, containing a UV dye penetrant, was seen to penetrate effectively throughout the structure (Fig. 2.10). The samples were then healed at 100°C for 2 hr.

The healing performance was quantified with flexural strength and stiffness measured using a four-point bend test (Fig. 2.11). The results were compared with the values for the standard composite, not containing any self-healing components. With this technique, they were capable of restoring the full strength of the undamaged composite. However, the hollow glass fibres caused an intrinsic reduction in flexural strength (around 10–20%) compared with the standard composite. Moreover, the damage event drained the healing agent and catalyst from an area considerably larger than the damaged region alone, rendering an excessive area inactive for following repairs.

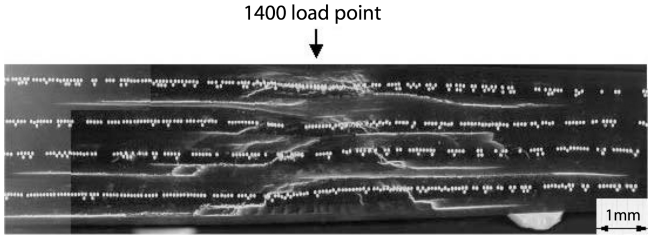

Figure 2.10: Cross-section of an impacted composite laminate containing self-healing capillaries. The laminate had a $[0°/+45°/90°/\text{-}45°]_{2s}$ layup, and the self-healing layers were placed at the +45°/90° and -45°/90° interfaces. The healing resin was Cycom 823, and contained a UV dye penetrant [54].

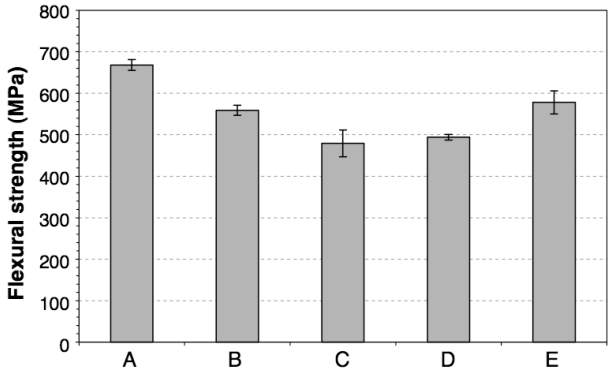

Figure 2.11: Flexural strength of (A) the standard composite, not containing any self-healing components, before damage (B) the self-healing composite before damage (C) the standard composite after damage (D) the self-healing composite after damage and (E) the self-healing composite after damage and repair (2 hr at 100°C) [54].

2.1.3 Microvascular network

Polymer coatings

A third approach was developed by Toohey *et al.* in which a bio-inspired embedded vascular network was used to store and deliver the healing agent(s) [57]. They used the same ROMP-based healing system as in ref. [4]. Periodic three-dimensional scaffolds were created by depositing a fugitive organic ink in a layer-by-layer build sequence [58], which were then infiltrated with an epoxy resin. The resin was cured and the ink was subsequently removed under light vacuum by heating to modest temperatures to liquefy the ink. An epoxy coating containing Grubbs' catalyst particles was then deposited on top of the network, and the network was filled with healing agent. The sample was loaded in four-point bend until crack initiation occurred in the coating, where the stress concentration was the greatest. Healing agent from the substrate wicked into the cracks in the coating, and polymerised on contact with the Grubbs' catalyst. Repeated healing of up to seven four-point bend fracture-heal cycles was demonstrated (Fig. 2.12).

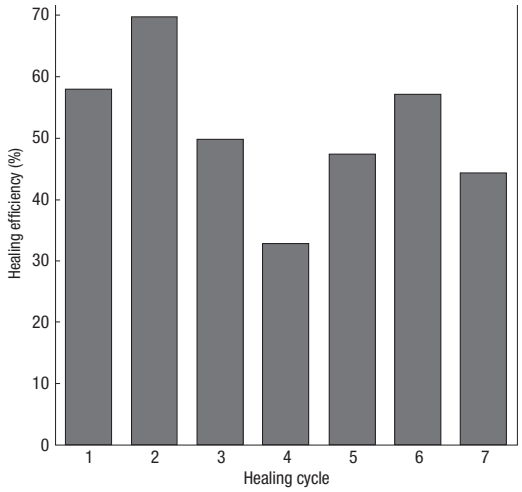

Figure 2.12: Healing efficiency for successive loadings of the coated microvascular beam specimen (10 wt% Grubbs' catalyst in the coating) [57].

Composite sandwich structures

Williams *et al.* investigated the use of a microvascular network to heal core damage in composite sandwich structures [59, 60]. Their sandwich structure consisted of a polymethacrylimide closed-cell foam core with $[0°,90°]_s$ E-glass/913 epoxy prepreg skins (Hexcel), of thickness 10.5 mm and 0.5 mm, respectively. The vascular network consisted of horizontal PVC tubing runners of 1.5 mm and 2.5 mm inner and outer diameter, respectively, embedded near the mid-plane of the core, in combination with 1.5 mm vertical drill holes, connecting to the runners. This network had negligible influence on the mechanical properties of the structure.

They cut a series of four-point bend samples (300 mm × 30 mm × 10.5 mm) from this material, and prepared them in two separate ways for impact testing. In

the first, the network was filled with pre-mixed healing agent (Ampreg 20 epoxy laminating resin (SPSystem) and slow hardener). In the second, the healing resin and the hardener were each contained within their own network, and thus mix *in situ* at the time of damage. Both types of sample were then impacted with an energy of either 3 J or 3.6 J using a 50 mm diameter tip, resulting in core-only damage. The samples were allowed to heal at 20°C for 36 hours, after which they were tested in four-point bend. The pre-mixed samples showed repeated recovery of the original flexural strength (Fig. 2.13). Full healing was also observed for 50% of the self-healed samples (Fig. 2.14). For the other 50%, where no healing was observed, either the resin or the hardener network had not been breached upon impact.

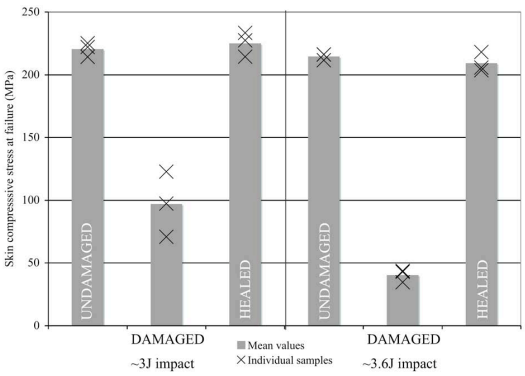

Figure 2.13: Four-point bend data for composite sandwich beam samples healed with pre-mixed resin [59].

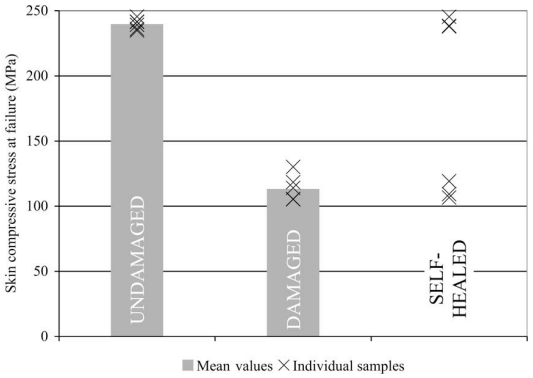

Figure 2.14: Four-point bend data for composite sandwich beam samples healed with two-part resin [59].

2.1.4 Solid state healing

Thermally-remendable polymers

Chen *et al.* have developed a matrix containing a weak chemical bond which breaks preferentially upon damage and reforms when heated [61, 62]. This process is based on the reversible Diels-Alder reaction, involving the breaking and healing of covalent bonds. They have been capable of recovering 57% of the original fracture load of a compact tension sample. However, the system is not compatible with existing composite resins or manufacturing methods.

Thermoset/thermoplastic blend

Hayes *et al.* dissolved a linear thermoplastic resin in their thermoset matrix, to act as the healing agent [63, 64]. The solubility parameter of the thermoplastic was similar to that of the thermoset, so the material remained as a single phase. Compact tension samples were prepared and fractured. Heat was applied to the material after crack formation, which increased the mobility of the thermoplastic chains, permitting them to diffuse across the crack and effectively bond the two faces back together. Up to 60% of the original toughness was restored. An advantage of this

system is that is is compatible with conventional processing techniques. However, a drawback is that the healing event does not involve the formation of covalent bonds.

2.2 Shape memory alloy (SMA) wire actuators

2.2.1 The shape memory effect

One-way shape memory

The shape memory effect (SME) is one of two special properties[1] of shape memory alloys (SMAs), whereby the material effectively 'remembers' its original shape upon thermal activation. Its origin is a diffusionless, solid-state martensitic transformation of the crystal structure, involving the co-ordinated shearing of atomic layers over distances less than an atomic spacing. When an SMA is cooled down from the cubic austenitic (parent) phase through its transition temperature, monoclinic martensitic variants form within the microstructure (Fig. 2.15). The shear of one variant is cancelled by another, and there is no macroscopic shape change. This is self-accommodated martensite (SAM). The interfaces between these variants are glissile, such that when an external stress is applied the most favourably oriented variants grow at the expense of those least favourably oriented (Fig. 2.15). This is preferentially-oriented martensite (POM). The original shape is restored by re-heating above the transformation temperature. The ability to recover seemingly irreversible strains by re-heating is the one-way shape memory effect.

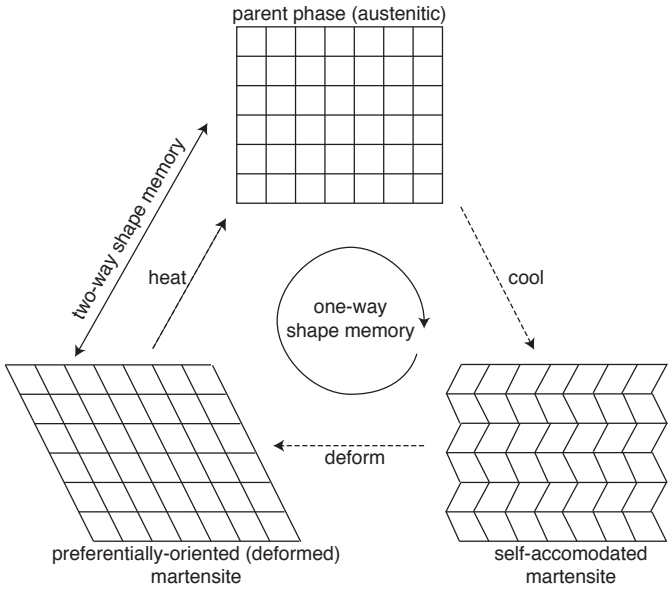

Figure 2.15: Microstructure changes in the one- and two-way shape memory effects [65].

[1]The second property is known as superelasticity. However, the resesarch presented in this thesis does not make use of this property, so it is not discussed further.

Two-way shape memory

In one-way shape memory only the shape of the parent phase is remembered. However, the SMA can be trained to remember the shape of both the parent phase and the preferentially-oriented martensitic phase, such that a component can be cycled between two shapes simply by a temperature change (Fig. 2.15). This is achieved by introducing internal stresses into the material, by prior cyclic deformation of the material in its fully martensitic state, followed by a constrained heating above its austenitic transformation temperature, for example, or by introducing thermally-stable particles and precipitates, which influence a predominant martensitic variant to form on cooling.

Driving force

Thermally-induced martensitic transformations require a driving force, supplied by the difference in chemical free energies between the high- and low-temperature phases (Fig. 2.16). At high temperatures the austenitic phase has the lower Gibbs' free energy. On cooling, the martensitic phase change does not start until the undercooling is sufficient to overcome the elastic strain and interfacial energies, at the M_s temperature. The transformation then proceeds athermally until M_f, where it is complete. The process is similar for the reverse transformation, with a hysteresis of 10-50°C between the two pathways (Fig. 2.17) [65].

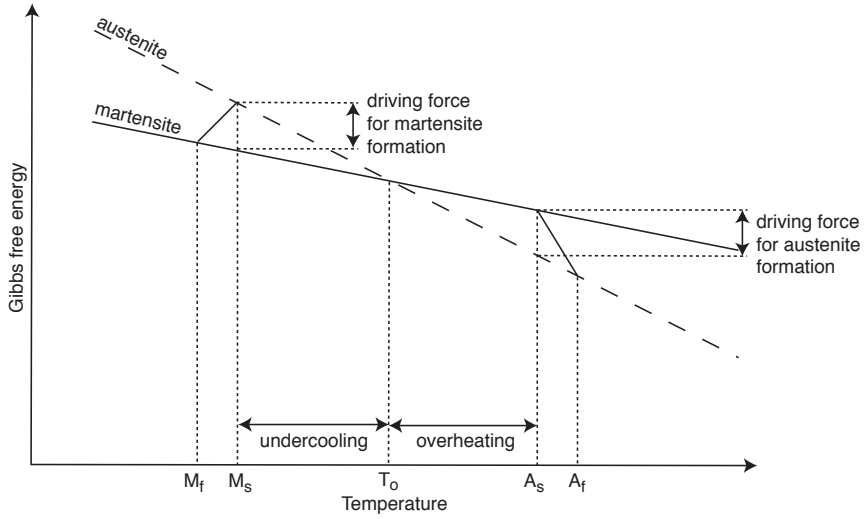

Figure 2.16: Gibbs' free energy diagram for the thermoelastic martensitic phase transformation in shape memory alloys. M_s and M_f are the martensite start and finish temperatures, respectively, and A_s and A_f are the austenite start and finish temperatures, respectively.

2.2.2 Nickel-titanium SMAs

The SME was first observed in 1932 in a gold-cadmium alloy [66], which is both expensive and toxic. Since the 1960s, however, nickel-titanium (Ni Ti)-based alloys,

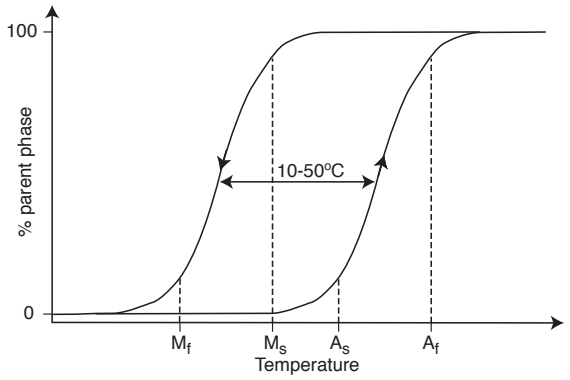

Figure 2.17: Schematic of the hysteresis curve for the thermoelastic martensitic transformation in shape memory alloys.

which are lower-cost and non-toxic, have attracted considerable attention [67]. When heated, these wires exhibit up to 8% recovery strains when free [68]. Numerous comprehensive reviews exist on the shape memory properties of free Ni Ti wires, for example [69]-[71]. However, one of the most important outcomes of the SME in prestrained Ni Ti-based SMA wires is the ability to generate recovery stresses of up to 800 MPa upon heating, when constrained at both ends [6]-[10]. Over the last ten years, several groups have studied methods of incorporating SMA wires into polymer-matrix composites [72]–[74], to meet the new and growing demand for composites with added functionality. The transformational and thermomechanical behaviour of constrained SMA wires are now discussed.

Transformational behaviour

When a prestrained SMA wire is embedded in a constraining matrix, its strain recovery is impeded, and its transformational behaviour subsequently altered. The effects of the constraining matrix on both the forward and the reverse transformations have been studied by measurements of the transformation heats and temperatures with differential scanning calorimetry (DSC). The effects of an epoxy or composite matrix [8],[75]-[77] and a metallic (Al) matrix [78] have been studied extensively, both yielding similar results. They found that increasing the SMA wire prestrain had no significant effect on the start temperature of the forward and reverse transformations—Tsoi observed a 5 K shift within a 0-6 % prestrain range—but did reduce the heat of transformation (Fig. 2.18). Furthermore, a recovery stress was generated even when there was no indication of a transformation on the DSC curve (Fig. 2.19).

These findings were explained by the difference between self-accommodated martensite (SAM) and preferentially-oriented martensite (POM) [75]. When an embedded wire composed of SAM and POM fractions is heated, the SAM is free to transform as it does not undergo a macroscopic shape change. The POM transformation, however, which is associated with a macroscopic shape change, is impeded by the surrounding matrix. A compressive force is exerted as a result. The magnitude of this force increases with increasing POM fraction. Moreover, the rate of transfor-

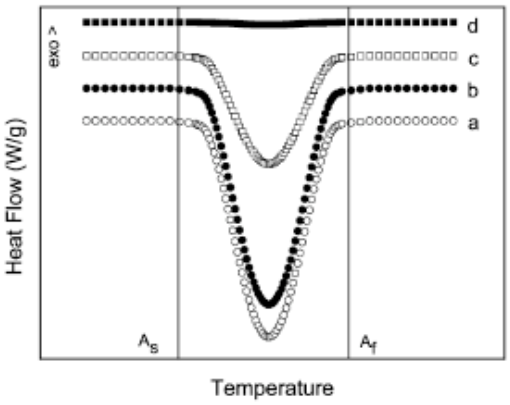

Figure 2.18: Schematic DSC curves for an SMA wire (a) in a free condition (b) embedded, with no prestrain (c) embedded, with an intermediate prestrain (d) embedded, with maximum prestrain [77].

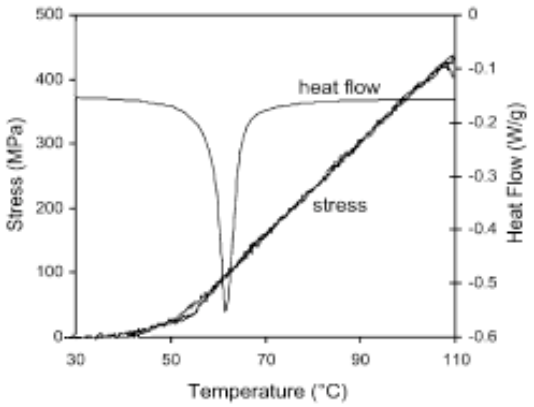

Figure 2.19: Recovery stress generation and heat flow of a 3% prestrained, constrained SMA wire [75].

mation of POM with temperature is small (∼0.2 vol%/K) and constant [75, 76], so the POM transformation is not detected by DSC. The peak in the DSC curves is associated with the transformation of the SAM, and the recovery stress with the impeded strain recovery of the POM.

Thermomechanical properties

While a lot of work has been done on the thermomechanical behaviour of SMA composites, a full understanding of their functional properties has yet to be achieved. At best, "basic design guidelines for SMA/epoxy smart samples" [79] can be given from experimental results, e. g. [68, 80, 81] . These are summarised as follows.

1. Ternary Ni Ti Cu wires are preferred over Ni Ti for adaptive composite application for their relatively small transformation hysteresis and their long-term cyclic stability.

2. The evolution of the recovery stress with temperature strongly depends on the wire prestrain level. A high prestrain induces a higher internal recovery stress and is, therefore, desirable to maximise the ability to close cracks. However, this is also found to result in a weaker interface and a lower maximum output strain. A moderate prestrain is, therefore, preferred.

3. The higher the prestrain, the lower the rate of recovery stress build-up with temperature.

4. For prestrains of ∼1%, the recovery stress does not start to build up until the transformation temperature is reached, whereas for higher prestrains it starts to build up instantaneously on heating, below the transformation temperature. It has been suggested that this is because Ni Ti Cu alloys in fact

undergo two martensitic transformations: a cubic (B2) to orthorhombic (B19) transformation over a small temperature range around room temperature, and, following this, an orthorhombic to monoclinic (B19') transformation. A highly-prestrained wire contains the stress-induced B19' phase, and it is the B19' to B19 transformation on heating that produces a recovery stress build-up below the A_s temperature.

5. The addition of reinforcing fibres with a negative thermal expansion coefficient (e.g. Kevlar fibres) can reduce the mismatch stress between the activated SMA wires and the matrix, shifting the debond temperature to a higher value.

2.2.3 SMA/epoxy interface

The recovery stress exerted by an embedded SMA wire modifies the structure's properties by generating compressive forces within the matrix via interfacial shear stress transfer. For effective stress transfer, therefore, the wire must remain well-bonded to the matrix during activation. A significant amount of work has been carried out in optimising the interfacial bonding, although no quantitative relation to the final activation efficiency exists. Lau *et al.* qualitatively investigated the influence of SMA wire prestrain on the extent of interfacial debonding [82]. They prestrained wires to 4, 6, 8 and 10%, embedded wire lengths of 20 mm in epoxy, and heated them to 78°C (A_f = 75°C). After 5 min at 78°C the wires prestrained to 4% and 6% both remained well-bonded (Fig. 2.20 a), whereas the 8% and 10%-prestrained wires became debonded (Fig. 2.20 b).

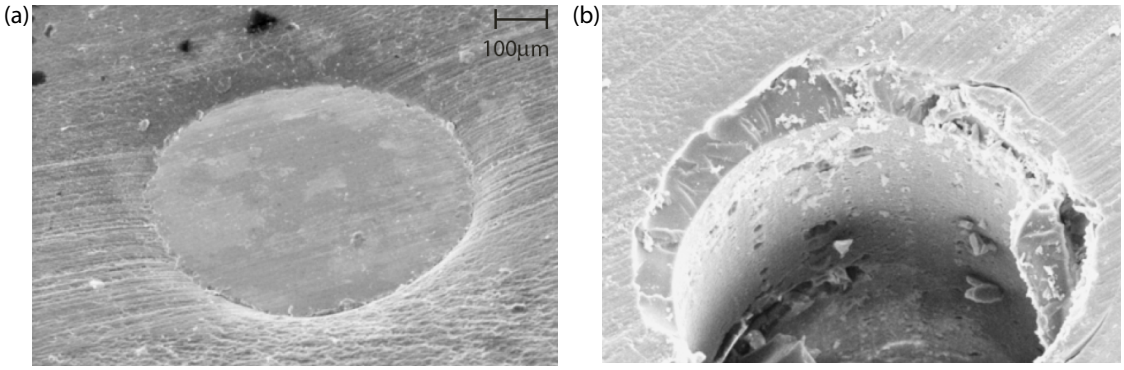

Figure 2.20: Embedded SMA wire prestrained to (a) 6% and (b) 8%, and activated at 78°C [82].

Interfacial strength

The most popular method to date to quantify interfacial strength is the single fibre pull-out test, first described by Kelly in 1970 [83]. A reinforcing fibre is embedded in a cylinder of epoxy resin, with an end of the fibre left exposed. A load is then applied to this end, until the fibre is debonded from, and then fully pulled out of the matrix. Figure 2.21 illustrates variations on the standard fibre pull-out test [84].

The fibre embedded length must be short enough so that it does not break before pulling free. The microbond test (Fig. 2.21 b) was developed as a result, and has been shown to be a reproducible and fairly simple test method [85, 86].

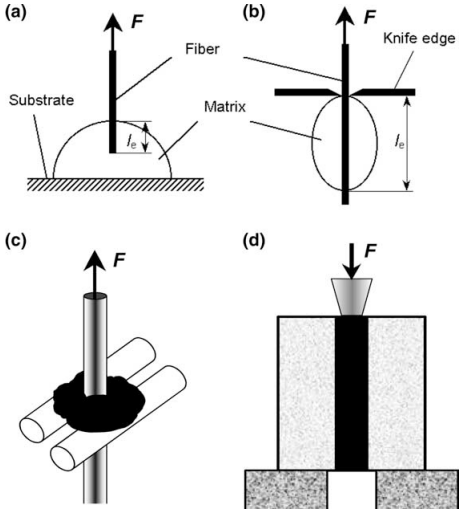

Figure 2.21: Methods to measure interfacial strength [84]. (a) The standard pull-out test, using a hemisphere of epoxy rather than a cylinder, (b) the microbond test [85, 87], (c) the three-fibre test [88] and (d) the push-out test [89].

The strength of the interface can be characterised by the experimental interfacial shear strength, τ_{exp} (Pa) [85]:

$$\tau_{exp} = \frac{F_d}{\pi d_f l_e} \tag{2.4}$$

where F_d (N) is the force at debonding, d_f (m) is the fibre diameter and l_e (m) is its embedded length. Typical τ_{exp} values for a 10 μm diameter fibre embedded in an epoxy matrix are 33 MPa, 38 MPa and 57 MPa for E-glass, Kevlar 49 and carbon fibres, respectively [85]. However, Eq. 2.4 considers the *average* interfacial properties rather than the local ones, and assumes a perfect interface, and so only gives a general comparative idea of the interfacial quality. Both stress-controlled [88, 90] and energy-controlled [91]-[93] debonding models have been developed to more-accurately characterise the interfacial quality. In the stress-controlled models the ultimate interfacial shear strength (τ_d)—the local shear stress at the propagating tip—is assumed to be constant throughout the experiment and does not depend on crack length. The energy-controlled models assume that the debonding zone extends when the energy release rate (G) attains its critical value (G_{IC}). Zhandarov *et al.* [84] compared both of these approaches, based on single fibre micromechanical tests, and concluded that both criteria can successfully be used as interfacial parameters. The most important experimental parameter in calculating both τ_d and G_{IC} is F_d, and must, therefore, be determined as accurately as possible [94].

Mechanical bonding

Baltá investigated the influence of the surface morphology of SMA wires with a diameter of 150 μm on the interfacial adhesion [95]. He found that the maximum interfacial shear stress before failure increased with the thickness of the surface oxide layer. Rough oxide surfaces resulted in cohesive failure, with $\tau_{exp} = 10.7$ MPa, while etched surfaces resulted in adhesive failure, with $\tau_{exp} = 2.1$ MPa [95].

Modifying the surface roughness of SMA wires has been investigated by Paine *et al.* [96], Jonnalagadda *et al.* [97] and Gabry *et al.* [98]. They used wires with diameters of 380 μm, 150 μm and 200 μm, respectively. The surface of the wires were either acid etched, hand sanded or sand blasted, and the wires were then embedded in an epoxy resin. Their pull-out performances were compared with that of an untreated wire. Sand blasting increased the debond strength by almost 200%, whereas hand sanding and acid etching reduced it by 10% and 25%, respectively (Fig. 2.22) [97]. Moreover, sand-blasted wires exerted the highest recovery stress when activated as they were well-constrained in the matrix.

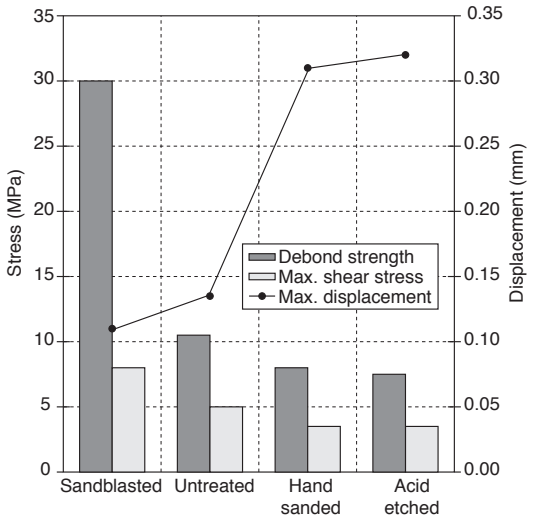

Figure 2.22: Average interfacial debond strength, maximum shear stress induced in the matrix and maximum displacement of the embedded SMA wire, for different wire surface treatments [97].

Lau *et al.* [99] and Umezaki *et al.* [100] increased the interfacial bond strength by manually twisting SMA wires in the martensitic state, with a diameter of 500 μm, to increase their surface roughness. The bond strength was characterised by a standard wire pull-out test of the NiTi wires embedded in epoxy (Fig. 2.23) [99]. The pull-out stress increased significantly with the number of turns: Lau *et al.* found that the force required to pull out an untwisted wire was 20 N, while that to pull out a wire with 40 turns was 150 N (Fig. 2.24); Umezaki's spiral wires pulled out at 120–200 N, and ruptured for embedded lengths above 70 mm, whereas his linear wires pulled out at 30 N, regardless of length. Lau *et al.* observed their wires in a scanning electron microscope and found that twisting produced helical patterns, which produced macroscopic grooves and caused the surface oxide to crack and roughen. The number of turns was, however, limited to a maximum of 15 for their

specimen geometry, as irreversible plastic strain occurred with more. Nonetheless, 15 turns raised the pull-out force by 150%, relative to the untwisted wires.

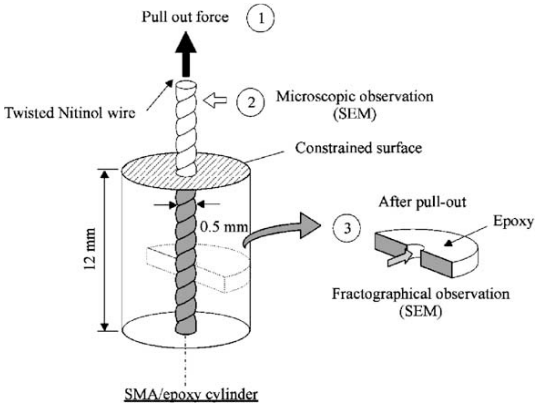

Figure 2.23: Schematic of the twisted-wire pull-out test [99].

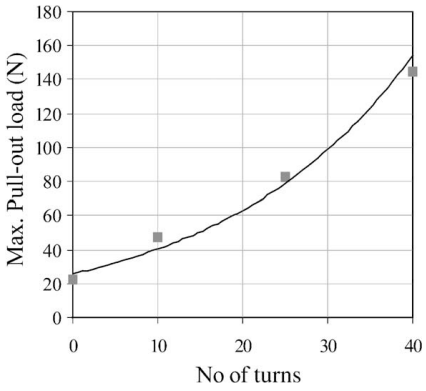

Figure 2.24: SMA wire pull-out load as a function of number of turns in the wires [99].

Chemical bonding

Chemical bonding between epoxy resin and continuous fibres with a diameter of 100 μm has been investigated as an alternative method of increasing interfacial strength [101]. This is an adhesion-enhancing technique, achieved by covering the wires with a silane coupling agent. The silane group forms a covalent bond with the metal oxide on the wire surface, and the other free end is capable of polymerising in conjunction with the matrix, due to their similar (3-acryloxypropyltrichlorosilane; APTS), or even identical (trimethoxysylylproplmethacrylate; MPS) structure. This is an interfacial bridging mechanism that forms chemical bonds at both extremities.

The standard tensile wire pull-out test was used. The absolute adhesion strength was calculated by normalising the force required for the wire to slip in the matrix by its embedded length. Typically, the untreated wires had an adhesion strength of 7-8 N/mm, which was increased by 91% and 85% for the APTS- and MPS-silane-coated specimens, respectively (Fig. 2.25). Control tests were carried out with n-octltrichlorosilane (OTS) silane, which has similar structure to the APTS and MPS silane, but cannot be incorporated into the polymerisation of the matrix. The average adhesion strength of these samples decreased 11% relative to that of the untreated wires (Fig. 2.25), confirming that the improved adhesion for the APTS and MPS silane samples was due to chemical interactions.

2.2.4 SMA wire actuators for smart structures

Shape memory alloy wires can be mounted on the surface of, or embedded within, standard composite structures, imparting added functionality to the material. When actuated, these wires are capable of modifying properties such as structural shape [102]-[104], stiffness and modal frequency of the composite, e. g. [105]-[113]. For

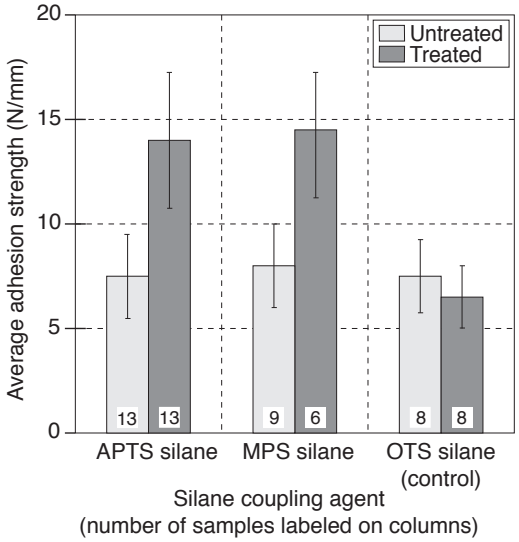

Figure 2.25: Average interfacial adhesion strength for SMA wires coated with APTS, MPS and OTS silane coupling agents and embedded in an epoxy matrix. The number of samples per measurement is shown at the base of each bar [101].

example, Scherrer *et al.* have integrated Cu Zn Al plates—chosen for their transition temperatures around 0°C—into the sandwich structure of an alpine ski, to enhance damping in hard snow conditions [110, 111].

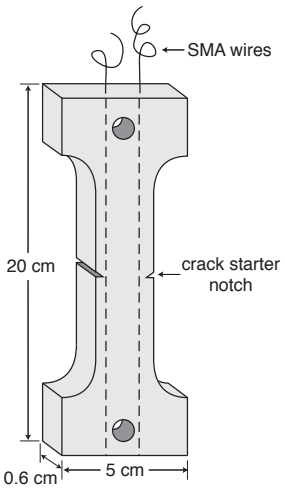

Figure 2.26: Photoelastic epoxy test specimen with embedded SMA actuators to reduce the stress intensity factor at the crack tip [11].

Shape memory alloy wires can also be used in damage control of composites—a field which is still in its infancy. Preliminary studies on the use of SMA wires to prevent crack propagation have been made by Rogers *et al.* [11] and Shimamoto *et al.* [114, 115]. Two approaches have been reported. In the first, martensitic SMA wires were pre-strained to 5% and embedded in tensile specimens of photoelastic epoxy resin with two starter notches at a central location (Fig. 2.26) [11]. The

wires were then activated and crack-tip stress intensities were determined from the fringe patterns in the epoxy. The stress intensity factor was 11.2 $\mathrm{N\,mm^{-3/2}}$ before activation and 8.5 $\mathrm{N\,mm^{-3/2}}$ afterwards, corresponding to a reduction of almost 25%, which impeded crack propagation. Shimamoto *et al.* [114, 115] found this reduction to increase with prestrain.

The second approach involved embedding austenitic (superelastic) SMA actuators with zero prestrain [11]. The idea was for the propagating crack to locally impart a large thermomechanical strain on the wire, transforming the austenite into stress-induced martensite in this region. An instantaneous crack closure force would consequently be exerted locally around the crack tip. However, Rogers found this method was ineffective since the brittle, elastic epoxy could not induce sufficient strain in the wire required to reach the stress plateau.

2.3 Fibre Bragg grating (FBG) sensors

In many fields and applications—aerospace, construction, oil and gas pipelines and sporting goods, for example [116]—it is important to routinely monitor the structural 'health' of parts. An *in situ* measurement not only improves safety and reliability, but also reduces the need for regular maintenance, and consequently down-time. Recently, non-destructive methods of *in situ* structural health monitoring, via measurements of the internal strain state, have been developed. Several sensing technologies, including fibre optic systems, silicon and hybrid MEMS and piezoelectric systems, have been investigated [65]. A small-diameter probe that can be easily embedded within the structure and that does not alter structural integrity is necessary for spatial strain mapping within composites. Consequently, optical fibres—with a typical diameter of 250 μm—are the preferred method, and have been the most extensively explored.

Numerous comprehensive reviews have been written on fibre optic sensing techniques, such as fibre Bragg grating (FBG) sensing, interferometric sensing, distributed fibre optic sensing and luminescent optical fibre sensing, e.g. [117]-[118]. The key advantages of optical fibres are that they are robust, lightweight, small and easily placed between composite plies, they are corrosion resistant and have a high maximum operating temperature, they require no electrical power at the sensing point and they are immune to electromagnetic interference, eliminating the need for costly and heavy shielding [16]. Of the optical fibre sensing techniques, FBGs are the most studied for non-destructive health monitoring. This is because their interrogation is relatively simple, and it is the only technology that can measure over several tens of kilometres: a single optical fibre can monitor dozens of points along its length, e. g. [65].

2.3.1 FBG principle of operation

A fibre Bragg grating sensor is a longitudinal periodic modulation of the refractive index of the core of an optical fibre. Optical fibres are made from silica doped with germanium, which is photosensitive in the ultra-violet range. The fabrication of FBGs is based on this property. A mask of the desired pitch—usually around

0.5 μm [117]—is placed over a finite length of the fibre—typically 1-20 mm [118]—and is then illuminated with a UV light source, creating an interference pattern. The refractive index of the sections of the fibre that are exposed to constructive interference zones is modified, producing a grating with a periodic set of bands of two differing refractive indices—n_1 and n_2—along the longitudinal axis of the fibre core (Fig. 2.27). When the fibre is illuminated along its axis with a broadband source, light is partially reflected at each interface. The interference of the reflected signal is destructive, except for the single wavelength for which it is perfectly in phase. This is the Bragg wavelength, given by the Bragg condition:

$$\lambda_B = 2n\Lambda \tag{2.5}$$

where λ_B (nm) is the Bragg wavelength, n is the effective refractive index of the core and Λ (nm) is the grating pitch. Schematic intensity plots of the incident, reflected and transmitted signals are shown in Fig. 2.28.

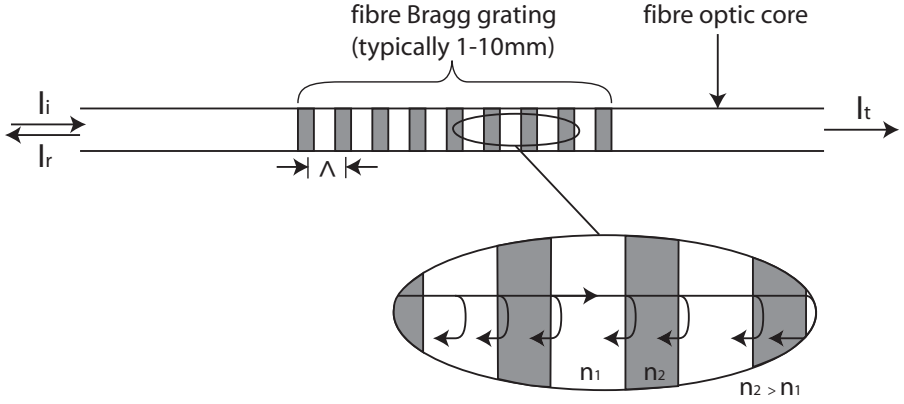

Figure 2.27: Schematic of a fibre Bragg grating sensor. A broadband light source is incident along the axis of the fibre (I_i). Most of the signal passes unaffected (I_t), and only the wavelength satisfying the Bragg condition is strongly reflected (I_r).

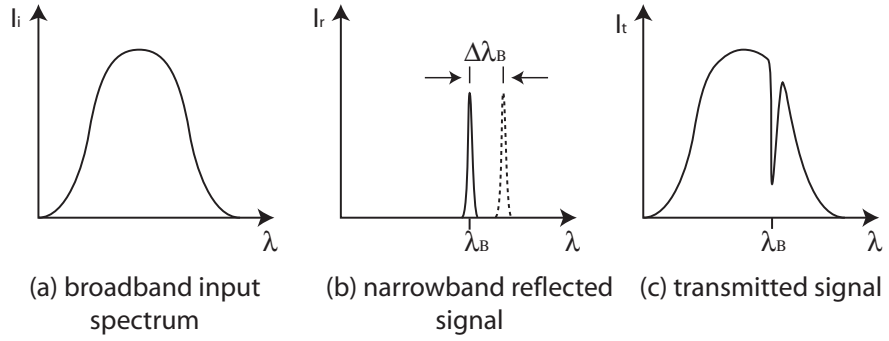

Figure 2.28: Schematic of (a) incident, (b) reflected and (c) transmitted optical signals for a fibre Bragg grating illuminated with a broadband light source.

An FBG, therefore, is a wavelength-selective filter. The reflected narrowband component has a typical bandwidth of 0.05-0.3 nm [117]. Altering the period of the

grating, by applying a strain to the fibre, shifts the Bragg wavelength (Fig. 2.28 b). The variation in λ_B is linear with strain. Thus, in monitoring $\Delta\lambda_B$, the strain at the location of the sensor can be determined. However, λ_B is also affected by temperature changes.

2.3.2 Effect of stain and temperature

Strain dependence

The response of an FBG to strain is governed by its physical elongation and by a change in the core refractive index due to photoelastic effects. Assuming a uniform strain field,

$$\frac{\Delta\lambda_B}{\lambda_{B,0}} = (1 - p_e) \cdot \epsilon \tag{2.6}$$

where $\Delta\lambda_B$ is the shift in the Bragg wavelength, $\lambda_{B,0}$ is the Bragg signal at zero applied strain, ϵ is the applied axial strain and p_e is the experimentally-determined strain-optic tensor:

$$p_e = \frac{n^2}{2}\left(p_{12} - \nu\left(p_{11} + p_{12}\right)\right) \tag{2.7}$$

where n is the effective refractive index of the unstrained fibre core, ν is the Poisson ratio of the fibre and p_{11} and p_{12} are strain-optic coefficients. Figure 2.29 shows the strain response of a 1.3 μm FBG for 0-2,000 applied microstrain, at constant temperature. From the plot the normalised response is

$$\frac{1}{\lambda_B}\frac{\delta\lambda_B}{\delta\epsilon} = 0.78 \times 10^{-6}\mu\epsilon^{-1} \tag{2.8}$$

So, for a 1.3 μm grating pitch, a 1 pm shift in wavelength corresponds to an applied strain of the order of $1\mu\epsilon$.

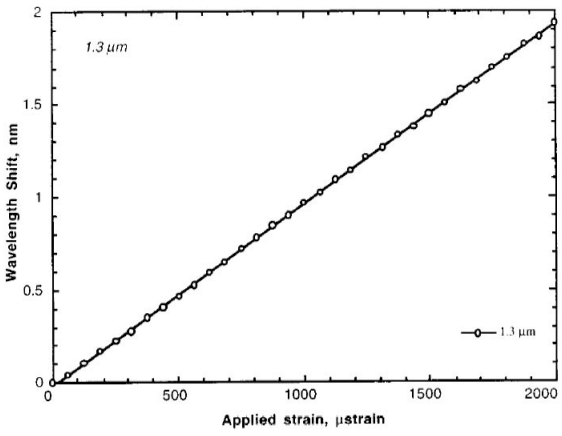

Figure 2.29: Strain response of a 1.3 μm FBG for 0–2,000 applied microstrain [117].

Temperature dependence

The response of an FBG to temperature is governed both by thermal strain and the variation of refractive index with thermal strain and temperature. This is expressed as

$$\frac{\Delta\lambda_B}{\lambda_{B,0}} = \left(\frac{(d\Lambda/dT)}{\Lambda} + \frac{(dn/dT)}{n} \right) \cdot \Delta T \tag{2.9}$$

where $(d\Lambda/dT)/\Lambda$ is the normalised thermal expansion coefficient (α), $(dn/dT)/n$ is the normalised thermo-optic coefficient (ξ)—relating to the thermal dependence of the refractive index—and ΔT is the temperature change. Figure 2.30 shows the temperature response of a 1.3 μm FBG at zero strain in the range 5-90°C. From the plot the normalised response is

$$\frac{1}{\lambda_B}\frac{\delta\lambda_B}{\delta T} = 6.67 \times 10^{-6}\,^{\circ}\mathrm{C}^{-1} \tag{2.10}$$

So, for an FBG with a 1.3 μm grating period, a shift of 1 pm in the Bragg wavelength corresponds to a temperature change of 0.1°C.

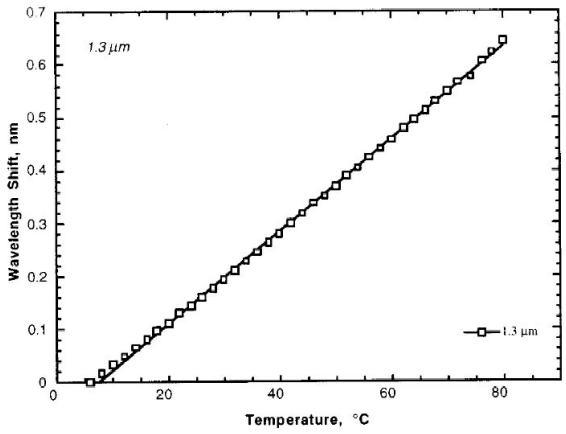

Figure 2.30: Temperature response of a 1.3 μm FBG for the range 5-90°C [117].

Strain and temperature discrimination

Combining the strain and temperature dependencies in Eqs. 2.6 and 2.9 gives the total fractional change in Bragg wavelength with strain and temperature:

$$\begin{aligned} \frac{\delta\lambda_B}{\lambda_{B,0}} &= (1 - p_e)\,\epsilon + (\alpha + \xi)\,\Delta T \\ &= K_\epsilon \epsilon + K_T \Delta\, T \end{aligned} \tag{2.11}$$

where $K_T \sim \xi$ for silica glass. K_ϵ and K_T values of a single grating are determined as described above. However, this information alone is insufficient to solve for ϵ and ΔT; a second equation of the form of Eq. 2.11 is required. This is achieved by

writing a second FBG, with a different Bragg wavelength, onto the same fibre optic core. This gives a second set of equations. In matrix form:

$$\frac{1}{\lambda_{B,0}} \begin{pmatrix} \Delta\lambda_{B1} \\ \Delta\lambda_{B2} \end{pmatrix} = \begin{pmatrix} K_{\epsilon 1} & K_{T1} \\ K_{\epsilon 2} & K_{T2} \end{pmatrix} \cdot \begin{pmatrix} \Delta\epsilon \\ \Delta T \end{pmatrix} \tag{2.12}$$

The inverse of Eq. 2.12 gives $\Delta\epsilon$ and ΔT:

$$\begin{pmatrix} \Delta\epsilon \\ \Delta T \end{pmatrix} = \frac{1}{\Delta} \cdot \begin{pmatrix} -K_{T2} & K_{T1} \\ K_{\epsilon 2} & -K_{\epsilon 1} \end{pmatrix} \cdot \begin{pmatrix} \Delta\lambda_{B1} \\ \Delta\lambda_{B2} \end{pmatrix} \tag{2.13}$$

where Δ—the determinant of the K matrix—is $K_{T2}K_{\epsilon 1}$-$K_{T1}K_{\epsilon 2}$. For this method to be valid, Δ must be non-zero; the two FBGs must have either different strain responses ($K_{\epsilon 1} \neq K_{\epsilon 2}$), temperature responses ($K_{T1} \neq K_{T2}$), or both. A number of methods to discriminate between strain and temperature effects exist, including using a reference grating, where one of the FBGs is bonded to a substrate while the other is not [119]-[122], dual wavelength interrogation, where the two sensors have a large pitch separation [123], dual diameter gratings with closely-centered pitches [124] and fibre doping to decrease the refractive index of one of the sensors [125]-[129]

2.3.3 *In situ* structural monitoring with FBG sensors

Cure monitoring

One application of FBGs is in monitoring the stresses that arise within a composite during its cure cycle, after its gelation point [130]-[132]. These stresses are a result of thermal strain mismatch between the fibres and the matrix, and have a significant influence on the final mechanical properties of the composite, such as compressive and buckling strength, and fracture strength and toughness [133]. By monitoring the development of internal strain, the cure schedule can be tailored to achieve optimal and reproducible mechanical properties [134]. Different curing cycles result in significantly different final internal strain levels. For example, in an experiment conducted by O'Dwyer *et al.* [134], the residual strain was $\sim 900\mu\epsilon$ for a rapid cooling rate of ~ 7°C/min from 180°C, which is reduced to $\sim 333\mu\epsilon$ by using a relatively slow cooling rate of 1°C/min from the same temperature.

Damage detection with FBG sensors

Damage such as delaminations and matrix fatigue cracking significantly reduce the strength of a composite structure [135]. It is, therefore, important to routinely monitor the structural health of parts. Fibre optic sensing technologies are the most suitable for structural integration, offering a method for continuous, non-destructive evaluation of the structural health of a component [136]. For example, FBGs have successfully been used to detect transverse cracks and delaminations in carbon-fibre reinforced polymers [137]-[140]. Furthermore, they have the advantage of being easily multiplexed in series along the length of an optical fibre [141, 142], where each sensor is assigned to a different characteristic wavelength (Fig. 2.31). The health of a composite structure can then be monitored with structural strain mapping.

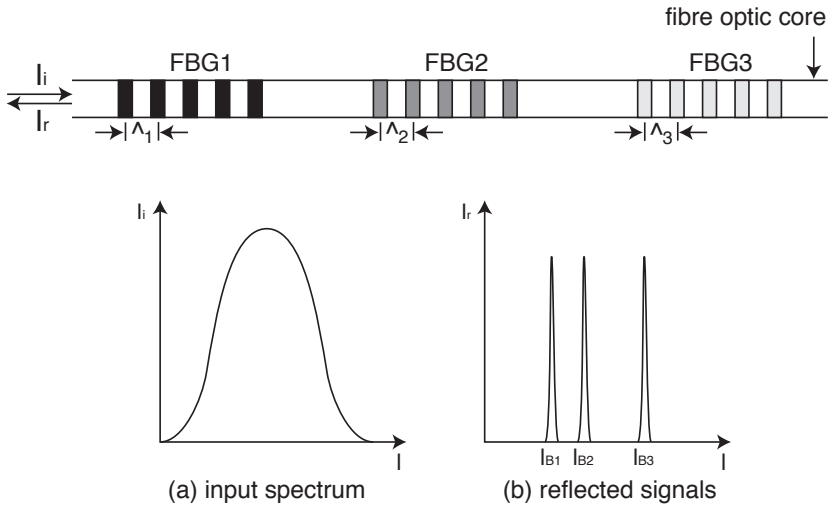

Figure 2.31: Wavelength-division addressing of fibre Bragg gratings in series in a single fibre.

An interesting new application of FBG sensors is for *remote* sensing of impact damage. Tsutsui *et al.* subjected composite samples containing several FBGs to impact damage, causing shock pulses to propagate through the sample (Fig. 2.32) [139]. The optical intensity reflected by each sensor as the strain pulse passed was recorded and converted into a strain (Fig. 2.33). The response of the FBG sensors was found to agree closely with that of a strain gauge (Fig. 2.33). The discontinuity in the signal, occurring in this case around 6 ms, represented the initiation of impact damage. Damage events could be detected up to 0.5 m away from the impact location, implying that a large composite panel can be monitored with a sparse density of FBG sensors.

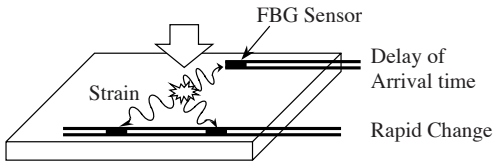

Figure 2.32: Schematic showing the principle of remote impact damage detection with FBG fibre sensors [139]. The impact causes a shock wave which propagates outwards from the impact site. By measuring the arrival time of the strain pulse at several FBG sensors, the impact can be detected and its location determined.

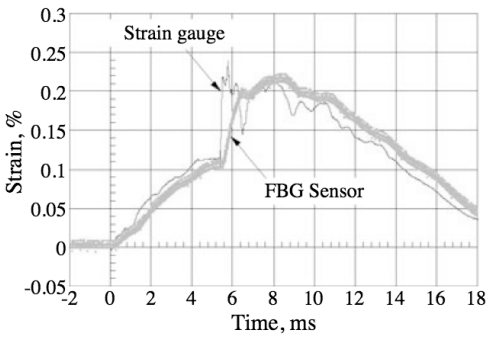

Figure 2.33: The strain response measured by a remote-sensing FBG sensor in the setup shown in Fig. 2.32 [139]. The FBG strain measurement is in close agreement with a strain gauge located at the same position.

However, the waves generated upon impact are ultrasonic, with frequencies of several tens or hundreds of kilo-Hertz, and travelling at velocities of the order of 1,000-7,000 $\mathrm{m\,s^{-1}}$ in polymer composites. This implies that remote sensing of impact events with FBG sensors requires high-speed interrogation of the FBG sensors. The timing of the leading edge of the strain pulse needs to be measured to about 1 μs, implying a sampling rate of at least 1 MHz. Ultrasonic sensing with FBGs is a relatively new field; a review of the state-of-the-art is given in [143, 144], for example. Betz *et al.* made the first steps toward acousto-ultrasonic sensing with fibre Bragg grating sensors [145]–[147]. In their initial work, they glued both piezoceramic transducers (PZTs) and FBG sensors (1 mm gauge length) on the surface of a perspex plate. The FBG sensors were interrogated using a narrow linewidth laser diode, whose wavelength was tuned to the wavelength at full-width half-maximum of the FBG spectrum (Fig. 2.34). The PZT was then used to generate 150 kHz Lamb waves, which propagated through the plate. The strain pulse caused the FBG sensor spectrum to shift, resulting in a modulation of the measured reflected optical intensity. With this method, they were capable of detecting the arrival time of the first symmetric mode Lamb wave (S_0).

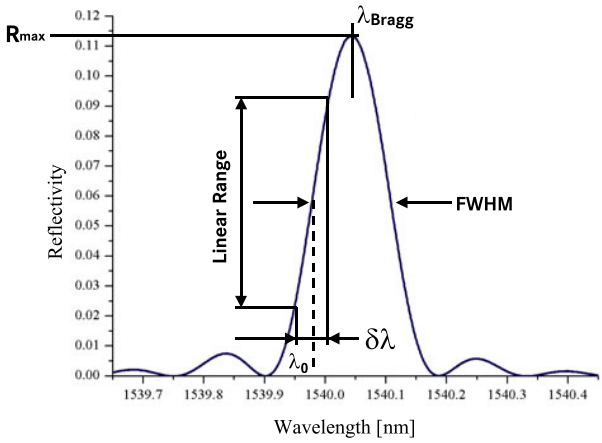

Figure 2.34: Interrogation of an FBG with a narrowband tunable laser diode. The wavelength of the laser was set to the value at the full-width at half-maximum of the FBG. Any shift in the FBG's spectrum due to a strain resulted in a modulation of the measured optical light intensity.

The method by Betz *et al.* requires a tunable laser diode. Tsuda *et al.* have developed a conceptually similar scheme that is simple and elegant, using a second FBG sensor (acting as an analyser) and a broadband light source in the place of the laser diode (Fig. 2.35) [17, 18, 148]. They mounted both PZT transducers and FBG sensors (10 mm gauge length) on the surface of a composite panel, and excited 250 kHz Lamb waves in the material using a PZT. The propagating waves were detected by both a PZT and an FBG located next to one another on the plate, and the two types of sensors had similar responses.

The extent of damage was evaluated by comparing the shape of the detected pulse with the shape of a previously-recorded signal from an undamaged area. They found that internal delaminations altered both the shape and arrival time of the detected

signal and were, therefore, able to locate the delaminations and determine their size. These differences exist because Lamb wave group velocity varies as $(E/\rho)^{1/2}$, where E is the Young's modulus and ρ is the density. This implies that a Lamb wave passing through a delaminated region—where the modulus is lower than an intact region—will, therefore, be slowed down. Several other groups have performed similar tests, either with FBG or PZT sensors, or a combination, with similar outcomes [147],[149]-[151]. An alternative approach was proposed by Diamanti *et al.* [152], who used a PZT array to generate a relatively uniform wavefront in a composite panel, and monitored reflections from internal damage.

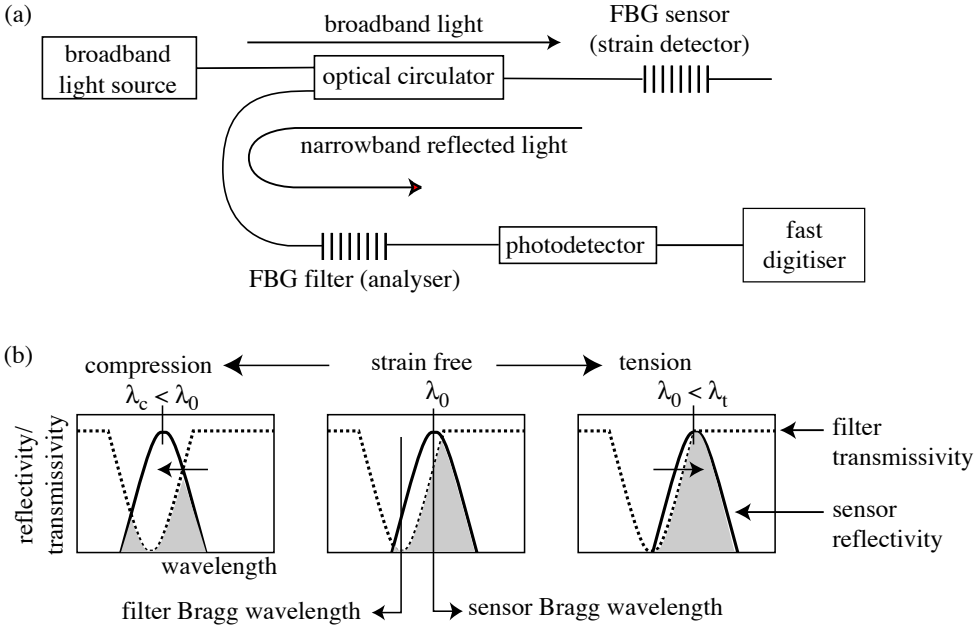

Figure 2.35: Principle of operation of the proposed FBG high-speed interrogation scheme [17, 18]. (a) The broadband light passes through an optical circulator which allows the narrowband reflected signal to be routed into an FBG filter, designed with a peak light transmission of a slightly lower Bragg wavelength. The light transmitted through the filter is detected by a high-speed photodetector and the signal is recorded by a fast-sampling digital oscilloscope, or data acquisition card and PC. (b) The amount of light reaching the photodetector depends on the overlap between the sensor reflectivity (solid curve) and the filter transmissivity (dashed curve). When a strain pulse passes the FBG sensor, it causes a small shift of the reflected wavelength under compression (left panel) or tension (right panel). This changes the intensity of the light transmitted through the filter (grey shaded area) and is recorded as a fast electrical pulse from the photodetector by the digital oscilloscope.

2.4 Summary

This literature review has described the state-of-the-art of each of the three components for the proposed Active Sensing and Repair Composite. Namely, these are

the microcapsule self-healing system, the shape memory alloy wire actuators and the fibre Bragg grating strain sensors. While these three components have not been combined before in a single material, each individual component has been sufficiently developed to justify doing so.

Of the three components, FBG sensors have been the most extensively developed. Many of their properties when free or embedded, and their dependence on strain and temperature have been investigated in detail. FBG sensors are promising candidates for *in situ* non-destructive health monitoring. In the case of SMA wires, the generation of recovery stresses in free and embedded wires is also reasonably well-characterised. However, the use of SMA wires to close internal cracks is barely explored. So far, most applications of SMA wires have concerned properties such as macroscopic shape change or modification of resonant vibrational frequency to control stiffness. Finally, when this research was initiated in 2004, self-healing materials was the least well-known of the three technologies. At the time, microcapsules that were ruptured by a propagating crack were primarily being developed by just one group, White *et al.*, who had nevertheless already demonstrated the feasibility of the concept [4]. However, their development had not yet included active sensing, or an active method of bringing the two crack faces back into contact, without the need for manual intervention.

Chapter 3

Materials

This chapter describes the materials used in this work, including their relevant properties and their preparation.

3.1 Microcapsule self-healing system

3.1.1 Requirements

The self-healing system should comprise a monomer and an agent that will lead to its polymerisation. The requirements are that

- the monomer in the microcapsules should have a low enough viscosity to flow over the crack plane,
- the polymerisation should be stoichiometry-independent,
- the constituents should not need thorough mixing,
- the polymerised film should have minimal cure shrinkage, to avoid the build-up of residual stresses, and
- the constituents should have a long lifetime once embedded in the material [153].

All of these requirements are met by reacting dicyclopentadiene (DCPD; $C_{10}H_{12}$) monomer and Grubbs' first generation catalyst[1]. DCPD is a colourless liquid at room temperature. PolyDCPD is used commercially in carbon-fibre reinforced materials for sporting equipment and aerospace applications, as well as for more regular household objects such as bath tubs. It is inexpensive, and forms a tough final material. Grubbs first generation' catalyst is a ruthenium-based carbene complex, and is a purple powder [154]. It is a live catalyst, and will operate at monomer-to-catalyst weight loading ratios of 10,000:1. It is readily synthesised from $RuCl_2(PPh_3)_4$, phenyldiazomethane and tricyclohexylphosphine [155]. It is, however, reactive with oxygen, and so must be stored in an anoxic environment.

The Grubbs' catalyst initiates ring opening metathesis polymerisation (ROMP) of the DCPD, whereby double carbon (alkene) bonds are cleaved open (Fig. 3.1).

[1]IUPAC name: (benzylidene-bis(tricyclohexylphosphine)dichlororuthenium)

The driving force for this polymerisation is the relief of ring strain. The resulting polymer has excellent mechanical properties and little cure shrinkage [156]. In this work, both the DCPD and the Grubbs' catalyst are supplied by Sigma-Aldrich.

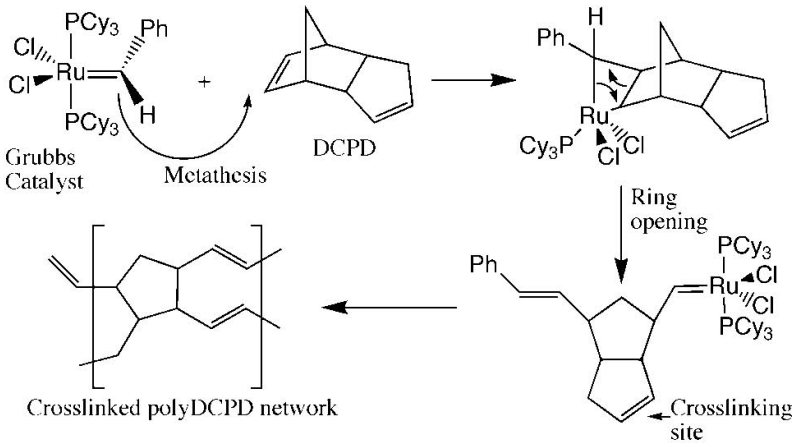

Figure 3.1: Ring-opening metathesis polymerisation of dicyclopentadiene [153].

3.1.2 Dicyclopentadiene (DCPD) healing agent

DCPD distillation

The dicyclopentadiene was distilled before encapsulation to remove any impurities. The distillation was performed under partial vacuum, so the DCPD boiled below its degradation temperature. 200 ml of DCPD were measured out into a 500 ml round-bottomed flask. This was then connected to a standard distillation setup, consisting of a Vigreux column, a three-way distilling head, a Liebig condenser, a vacuum adapter and two receiving flasks. All tapered joints were lightly greased to ensure a good seal. The flask containing the DCPD was immersed in an oil-bath, which was in turn set on a hot plate. The hot plate was set to 175°C, and the oil bath was stirred with a magnetic stirrer. The pressure was then lowered from 760 mm Hg to 20 mm Hg. The first 10% of the distillate consisted of lower molecular weight cyclopentadiene, and was collected in the first receiving flask and discarded. The DCPD then boiled over at around 48°C, and was collected in the second receiving flask. Finally, the last 10% of the liquid left in the original flask was also discarded.

Microcapsule fabrication

The microcapsules were made by an *in situ* polymerisation method in an oil-in-water emulsion [26]. The apparatus consisted of a beaker containing the mixture, a water bath, a hot plate and a mechanical mixer and stir blades (Fig. 3.2). 200 ml of deionised water and 50 ml of 2.5 wt% ethylene maleic anhydride copolymer (Zeeland Chemicals) were added to a 500 ml beaker. The beaker was placed in the water bath and the mechanical mixer blades were immersed in the mixture. The mixer was set to the desired agitation rate. The dependence of final microcapsule diameter on

agitation rate has been previously determined (Fig. 3.3) [26]. 5.0 g urea, 0.5 g ammonium chloride and 0.5 g resorcinol (all Sigma-Aldrich) were added to the mixture, in that order. The pH was measured at this point, and was between 2.5 and 2.8. The pH was then brought to just above 3.5 by a drop-wise addition of sodium hydroxide solution (Sigma-Aldrich), and then brought to 3.5 exactly by adding drops of 1 N hydrochloric acid solution (Sigma-Aldrich). 2-3 drops of octanol (Sigma-Aldrich) were added to eliminate surface bubbles. At this point, 60 ml of DCPD were added in a slow stream, and the droplets were allowed to stabilise for 10 min. Finally, 12.67 g of 37% formaldehyde solution (Fisher Scientific) was added and the beaker was covered with foil. The probe target temperature was set to 55°C at a heating rate of 1°C/min. A timer was set to switch off both the mechanical stirrer and hot plate after 4 hr. After this time the capsules were filtered, rinsed with deionised water, and dried in air for 24 hr and then in an oven at 80°C for an additional 2 hr, to remove residual water. An image of the resulting microcapsules is shown in Fig. 3.4

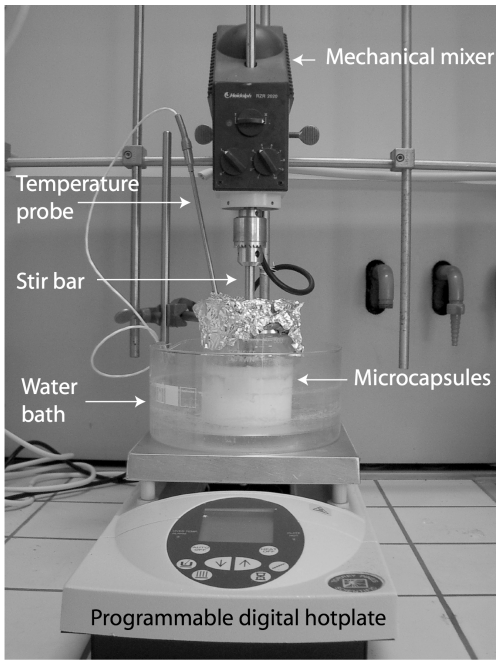

Figure 3.2: Setup for microcapsule preparation.

3.1.3 First generation Grubbs' ruthenium catalyst

Complete coverage of the crack plane with polyDCPD is needed for a successful healing event. Equally as important is the availability of the catalyst, determined by its size, crystal morphology and dissolution kinetics. Smaller particles dissolve faster in the DCPD, but their reactivity can be significantly reduced when exposed to the hardener of the matrix material in which it is embedded [153]. Jones *et al.* have optimised the morphology of the catalyst via a recrystallisation method [157]. In addition, Rule *et al.* have developed a wax encapsulation procedure to further protect the catalyst from deactivation [33].

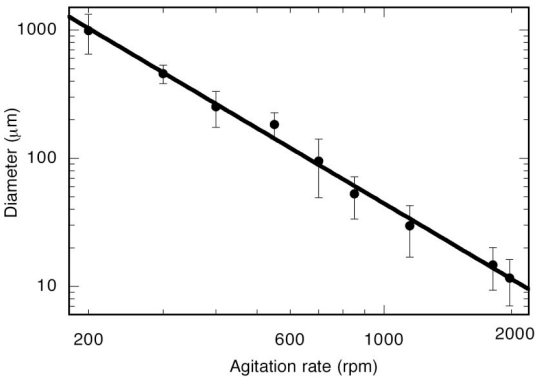

Figure 3.3: Dependence of final microcapsule diameter on agitation rate [26].

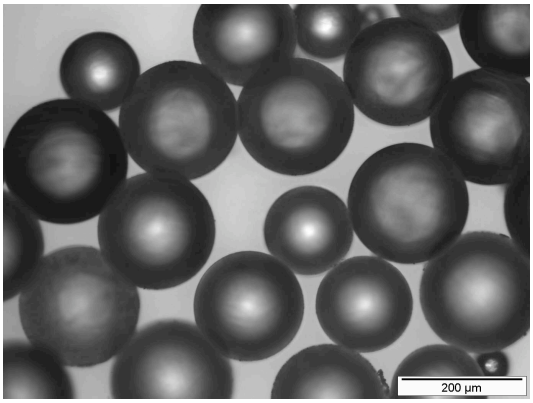

Figure 3.4: Optical microscope image of the DCPD microcapsules.

Recrystallisation

The Grubbs' catalyst (Sigma-Alrdich) was recrystallised using a non-solvent addition method, to produce a finer-scale average particle size [157]. The Grubbs' catalyst used in this work had a rod-like morphology with an average length of 150 μm and a cross section of $40 \times 50\,\mu\text{m}^2$. When recrystallised, it had the same rod-like dimensions, but the average length was reduced to about 10 μm (Fig. 3.5).

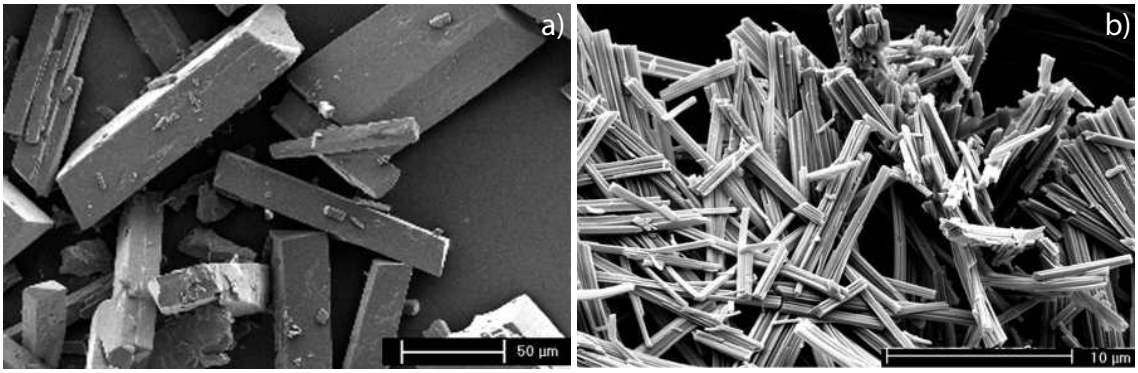

Figure 3.5: Scanning electron microscope images of the Grubbs' catalyst (a) before and (b) after precipitation from CH_2Cl_2/acetone solution [157].

The recrystallisation process was carried out under nitrogen. One gram of catalyst was weighed into a 500 ml round-bottomed flask, which was then sealed with a rubber septum. Fourteen millilitres of methylene chloride (Sigma-Aldrich) were then added to the flask with a syringe. The solution was stirred over a magnetic stirrer until the catalyst was fully dissolved. The flask was then placed in an ice water bath, over the magnetic stirrer, and the solution was allowed to cool. Once cooled, 10 ml of acetone was added to the solution in a drop-wise manner, causing the catalyst to precipitate out of solution. Once the recrystallisation was completed, the solution was filtered and the Grubbs' catalyst was collected and rinsed with ace-

tone. Finally, the catalyst was transferred to small vials, which were then sealed with a permeable lid and placed under vacuum to dry.

Wax encapsulation

The Grubbs' catalyst was encapsulated in paraffin wax particles before it was embedded in the epoxy matrix [33], to protect it from chemical attack by the matrix material hardener [153]. The wax, while insoluble in the hardener, is soluble in DCPD, meaning that the catalyst can still polymerise the DCPD and heal a crack. Furthermore, wax encapsulation allowed for a finer dispersion of the catalyst.

The procedure for wax encapsulation was as follows. 9 g of paraffin wax (Sigma-Aldrich) were added to 1 g of catalyst in a small vial. The vial was sealed with a rubber septum and placed in an 85°C water bath, to melt the wax. 50 ml of 1 % poly-vinyl-alcohol solution (Sigma-Aldrich) was added to 150 ml of deionised water in a beaker, which was also placed in the water bath to heat. The mechanical mixer blades were immersed in the solution and set to 700 rpm. Once the wax had melted, the vial was removed from the water bath, the septum was removed and the wax/catalyst mixture was carefully poured into the solution in the beaker, where it formed droplets under agitation. After a few minutes, the solution was quenched with 600 ml of ice water. Finally, the catalyst/wax microspheres were filtered, rinsed with deionised water and placed under vacuum to dry.

3.2 Shape memory alloy wire actuators

The SMA wires were ternary Ni:Ti:Cu with composition 44.86:45.08:10.06, a diameter of 150 μm and an intrinsic two-way shape memory effect of 1.2% [95] (Furukawa Electric). All SMA wires were held in an oven at 100°C for 10 min prior to testing, to remove any strain history.

3.2.1 Transformation temperatures

The transformation temperatures of the SMA wire were evaluated with conventional differential scanning calorimetry (DSC). A sample with a mass of about 3 mg was sealed in an aluminium crucible and placed in the measurement chamber, alongside a reference. The sample and reference were heated a first time to 120°C, cooled back to 30°C and heated a second time to 120°C, all at a rate of 10°C/min, under a continuous gaseous nitrogen purge with a flow rate of 25 ml/min. The test was repeated three times. An example measurement is shown in Fig. 3.6. The lower peak represents the martensite to austenite transformation (heating), and is endothermic. The upper peak represents the austenite to martensite transformation (cooling), and is exothermic. The average transformation temperatures and heats of reaction for the three tests are summarised in Table 3.1. The measurements confirm that this SMA wire is suitable for integration with the self-healing system described in §3.1: the A_f temperature remains sufficiently below the 130°C deactivation temperature of the Grubbs' catalyst and the transformation hysteresis is relatively narrow, which permits good on/off control.

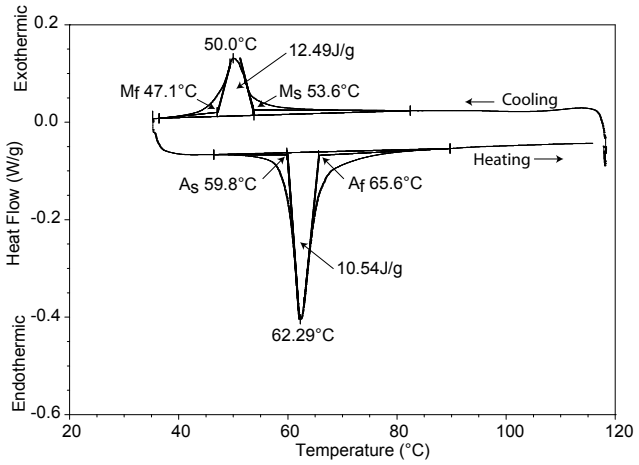

Figure 3.6: Differential scanning calorimetry curve for the unconstrained, unprestrained SMA wire.

Table 3.1: SMA wire transformation temperatures and heats. M_s and M_f are the start and finish temperatures of the martensite to austenite (forward) transformation, respectively, and A_s and A_f are the start and finish temperatures of the austenite to martensite (reverse) transformation, respectively.

M_s [°C]	M_f [°C]	$\triangle H_M$ [J/g]	A_s [°C]	A_f [°C]	$\triangle H_A$ [J/g]
53.6	47.1	10.2	59.8	65.6	11.0

3.2.2 Tensile properties

A single SMA wire was mounted in a tensile tester and pulled in tension at a rate of 1 mm per minute, until failure. A representative stress-strain curve for a single wire is shown in Fig. 3.7. This test was repeated four times on different samples. The tensile properties are summarised in Table 3.2. The Young's modulus of the wire in the martensitic state was given by the initial gradient of the curve in Fig. 3.7, in the strain range 0-0.05%.

Table 3.2: Room-temperature tensile properties of the SMA wire.

Young's modulus	[GPa]	19.0
Elastic limit	[%]	5.7
Tensile strength	[MPa]	977
Elongation at failure	[%]	7.4

The relatively high tensile strength and elongation before failure mean that the wire will remain intact when a propagating crack intersects it. Moreover, the elastic limit of 5.7%, coupled with localised debonding between the wire and the matrix when a crack propagates, will ensure that the wire is not plastically deformed.

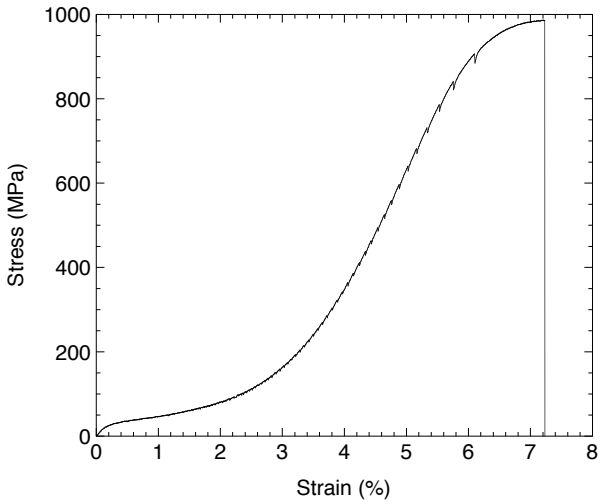

Figure 3.7: Stress-strain plot for a single SMA wire at room temperature.

3.2.3 Recovery stress

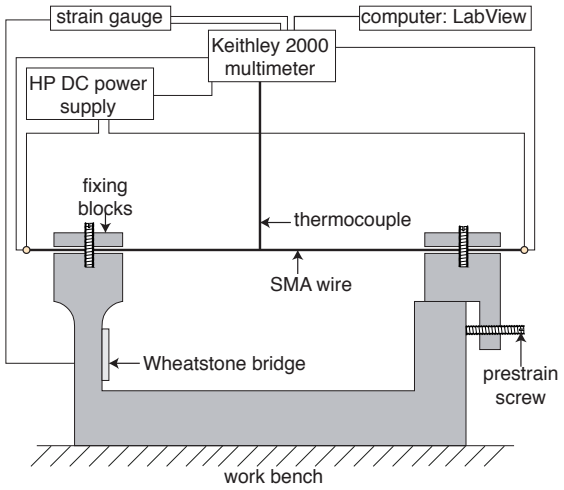

Figure 3.8: Schematic of the U-holder and its electrical connections.

The recovery stress exerted by a single SMA wire was experimentally-determined using the U-holder, developed at EPFL (Fig. 3.8) [158]. This setup measures the force—and therefore stress—generated per wire as a function of temperature. An SMA wire is held between the two clamps of the U-holder, and can be prestrained once fastened. The wire is activated by a current, ramped between 0 and 0.4 A, controlled externally by entering a heating program in LabView. The wire's temperature is measured with a thermocouple in close contact with its surface by means of conducting paste. A full Wheatstone bridge bonded to one of the arms measures strain, which is then converted into a corresponding force by the LabView program. The force and temperature data are recorded for offline analysis.

The recovery stress exerted by an activated SMA wire prestrained to 0, 2, 4

and 6% and activated twice between 0 A (room temperature) and 0.4 A (∼110°C) was measured (Fig. 3.9). The wire exerts between about 5 N (for a 0% prestrain) and 8 N (for a 6% prestrain) at 110 °C, corresponding to 280 MPa and 450 MPa, respectively. After the first cycle, the recovery stresses at room temperature were zero for all samples, due to the relaxation of some preferentially-oriented martensite into self-accommodated martensite [68]. The results of the second heating cycle are summarised in Fig. 3.10; subsequent heating/cooling cycles would follow these same curves.

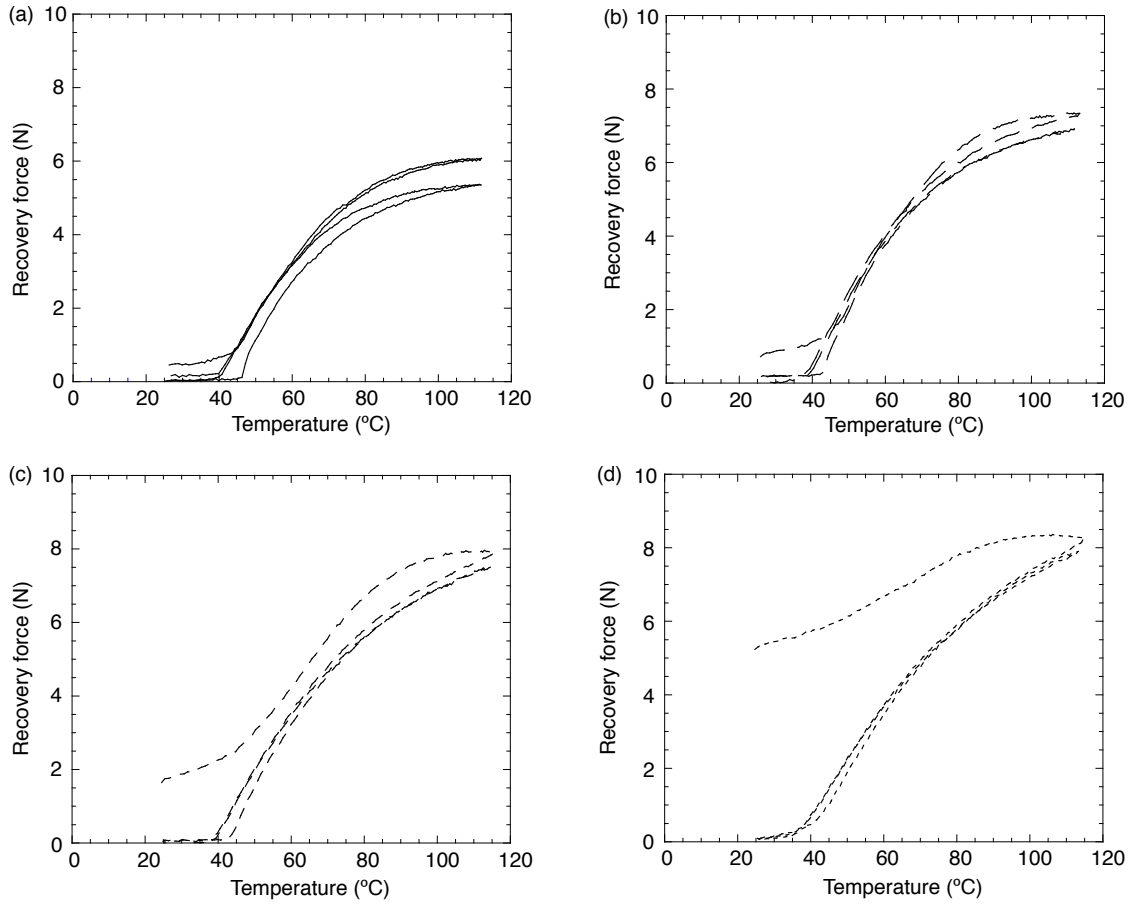

Figure 3.9: Recovery force generated by an SMA wire, constrained at both ends, with prestrains of (a) 0%, (b) 2%, (c) 4%, (d) 6%. Each curve shows two cycles between room temperature and about 110°C. The wire had 150 μm diameter, so 1 N force corresponds to a stress of 56.6 MPa.

3.2.4 Resistivity

The temperature dependence of the wire's resistivity was determined by measuring the voltage-current behaviour of a single, unembedded SMA wire with a simple circuit with a DC power supply. A thermocouple was attached to the wire's surface with conductive paste. The current was cycled twice between 0 A and 0.4 A. The wire exhibits two regimes of linear voltage-current behaviour—one below the

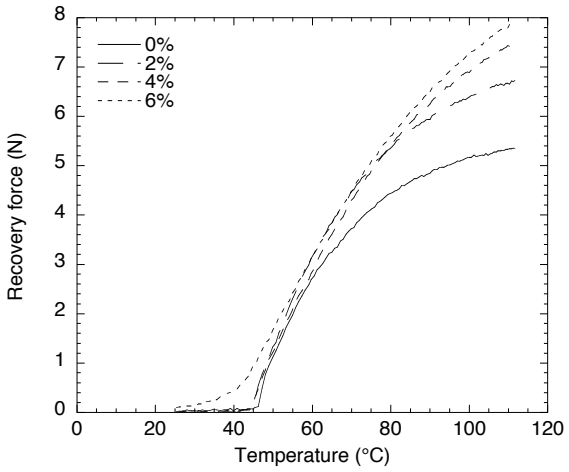

Figure 3.10: Comparison of the recovery forces generated by a constrained SMA wire prestrained by (a) 0% (b) 2% (c) 4% (d) 6%. The data are taken from Fig. 3.9.

transformation zone and one above it (Fig. 3.11). The resistivity of the wire changes from about $110\,\mu\Omega\,\mathrm{cm}$ to $100\,\mu\Omega\,\mathrm{cm}$ over this transformation region (Fig. 3.12), and is constant at $100 \pm 1\,\mu\Omega\,\mathrm{cm}$ above the transformation.

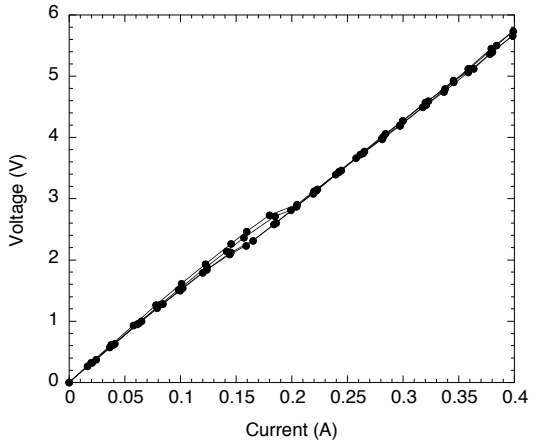

Figure 3.11: Voltage versus current for an unembedded SMA wire 25 cm long.

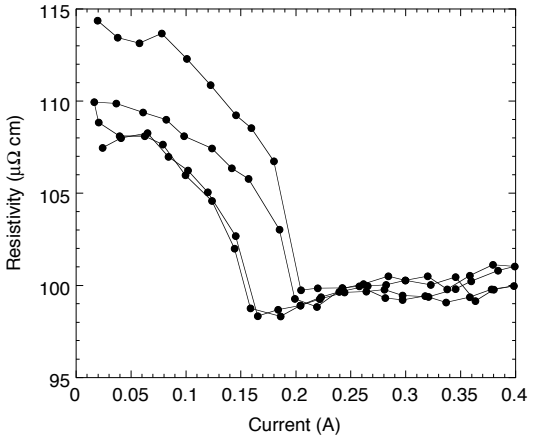

Figure 3.12: Resistivity of an unembedded SMA wire.

3.3 Fibre Bragg grating sensors

3.3.1 FBG fabrication

The FBG sensors were written on SMF28 silica-based optical fibre with $8\,\mu$m, $125\,\mu$m and $250\,\mu$m core, first cladding layer and second cladding layer diameters, respectively. To write an FBG, the second cladding layer—an acrylate layer—was first chemically stripped over a 10-15 mm length where the grating was to be written.

The region was cleaned with isopropanol, and the fibre was clamped in a support and aligned in front of a pulsed laser, with its long axis perpendicular to the direction of laser illumination. A phase mask was placed in front of the optical fibre, and was then illuminated with 193 nm light at 10 Hz, creating an interference pattern. The refractive index of the fibre sections exposed to constructive interference zones was modified. The evolution of the reflection and transmission spectra of the FBG sensor were monitored in real-time, and the laser was turned off once the FBG sensor had the desired reflectivity—typically 50-80%.

3.3.2 Strain dependence

A single optical fibre with an FBG written on its core was clamped at one end and mounted vertically. Weights were then progressively hung from the lower end of the fibre and the fibre strain was calculated assuming a Young's modulus of 72 GPa. A Micron Optics sm125 Sensing Interrogator was used both to interrogate the sensor and to monitor its Bragg wavelength. The shift in Bragg wavelength with strain is plotted in Fig. 3.13, which gives $K_\epsilon = 0.77 \times 10^{-6}\,^\circ\mathrm{C}^{-1}$, i. e. the Bragg wavelength shifts 1.2 pm per unit longitudinal microstrain.

3.3.3 Temperature dependence

A single optical fibre with an FBG written on its core was placed in an oven, and the temperature was increased in steps. The shift in Bragg wavelength was recorded once thermal equilibrium was reached. The shift in Bragg wavelength with temperature is plotted in Fig. 3.14, giving $K_T = 6.88 \times 10^{-6}\,^\circ\mathrm{C}^{-1}$, i. e. the Bragg wavelength shifts 10.6 pm per degree temperature change.

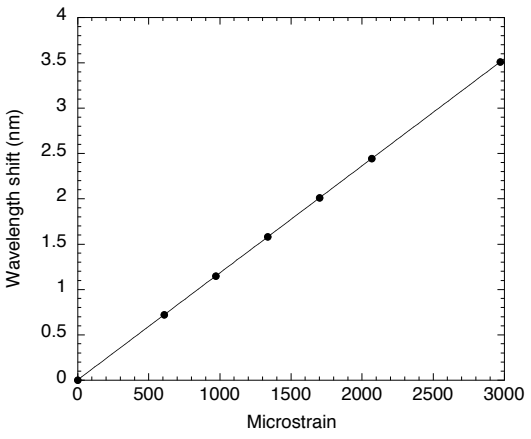

Figure 3.13: Strain response of a 1533.35 nm FBG with a 4 mm grating length, written on an SMF-28 optical fibre.

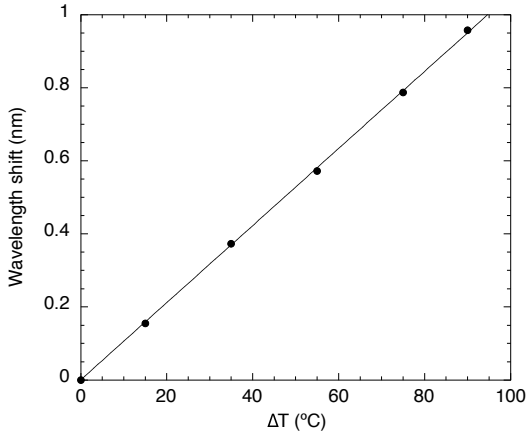

Figure 3.14: Temperature response of a 1533.35 nm FBG with a 4 mm grating length, written on an SMF-28 optical fibre.

3.4 Carbon fibre reinforced polymer

3.4.1 Matrix

The matrix was a two-part epoxy system consisting of EPON 828[2] monomer (Shell Chemicals) and diethylenetriamine (DETA) hardener (Sigma-Aldrich). EPON 828 is a diglycidyl ether of bisphenol A, referred to as DGEBA. An epoxy was chosen as the matrix material, due to the stability of Grubbs' catalyst in the presence of epoxide groups [159]. Furthermore, EPON 828 has relatively low thermal and electrical conductivity, and excellent mechanical properties. DETA was chosen as the hardener as it allows low-temperature curing and produces a brittle polymer that gives clean crack faces. The EPON 828 was mixed with the DETA in a 100:12 mass ratio.

3.4.2 Reinforcing fibre

A standard carbon-fibre non-crimp fabric (NCF; Saertex) made of Toray T-700 12K yarns was used as the reinforcing fibre bed. Carbon fibres were chosen as they are used in many structural commercial applications, for example in the aerospace industry, they are readily available and are relatively light and stiff. A [0°/90°] non-crimp fabric was chosen because of its superior drapability and good mechanical properties [160]. The fabric exists as a single 0° ply and a single 90°, bound together with polyester stitching thread. Details of the fibres are given in Tables 3.3 and 3.4.

Table 3.3: Data sheet for the biaxial [0°/90°] carbon-fibre non-crimp fabric used in this study.

Component	Areal weight [g/m^2]	Tolerance [±%]	Material
0° ply	150	5	carbon
90° ply	150	5	carbon
stitching	6	5	polyester

Table 3.4: Longitudinal physical properties of a unidirectional T700-12K carbon fibre ply.

Young's modulus	[GPa]	230
Tensile strength	[GPa]	4.9
Elongation	[%]	2.1
Density	[gcm^{-3}]	1.8

[2]European name: EPIKOTE 828

Chapter 4

Integration of self-healing polymer and SMA wires

4.1 Introduction

This section presents the integration of SMA wires in the self-healing polymer matrix, and evaluates the improvement that incorporating SMA wires has on the self-healing performance of the system. In previous studies of the self-healing polymer, e.g.[4], the faces of the fractured samples were brought back into contact manually. For samples containing SMA wires that bridge a crack, it should be possible to bring the two crack faces back into contact by activating the wires with a small current, thereby removing the need for manual intervention. Moreover, the closure force exerted by the SMA wires should lead to a reduced crack volume, which in turn should optimise the healing event.

Healing performance is evaluated here using an established protocol based on the fracture and re-fracture of tapered double cantilever beam (TDCB) fracture samples [46]. The influence of the SMA wires on the healing performance is first evaluated using samples where the healing agent is injected into the crack, which eliminates the variability of the delivery of the healing agent, and then using samples where the healing agent is delivered by embedded microcapsules.

4.2 Experimental techniques

4.2.1 Healing performance

The self-healing properties were investigated using samples with a tapered double cantilever beam geometry (Fig. 4.1), first developed by Mostovoy *et al.* [48]. This technique provides a measurement of the fracture toughness (K_{IC}; $\mathrm{MPam}^{1/2}$) that is independent of the initial crack length, i. e.

$$K_{IC} = \alpha P_C \tag{4.1}$$

where P_C (N) is the critical fracture load and α ($\mathrm{m}^{-3/2}$) is a geometric term—$11.2 \times 10^3\,\mathrm{m}^{-3/2}$ for the present geometry [46].

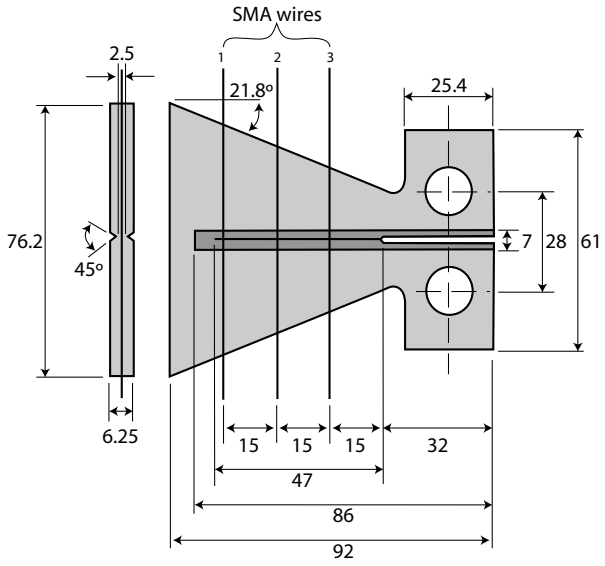

Figure 4.1: Tapered double cantilever beam (TDCB) sample geometry. Samples were prepared both without SMA wires and with three SMA wires embedded perpendicular to the crack plane and uniformly-spaced. The 7 mm-wide region around the crack plane indicates where the Grubbs' catalyst was localised. The distance units are mm.

Three SMA wires were each tensioned with a 50 g mass, corresponding to a prestress of about 28 MPa. Taking the wire's Young's modulus of 19 GPa (Table 3.2), this induces a strain of about 0.1% in the wires. While under tension, the wires were embedded at the mid-plane of the sample, perpendicular to the crack direction (Fig. 4.1). Two types of samples were prepared to test the polymer's self-healing. In the first, Grubbs' catalyst was embedded in the matrix and the DCPD healing agent was manually-injected into the crack, termed *injected* samples. These were to evaluate the effect of the SMA wires on the healing performance without the variability of the DCPD delivery. In the second, both the Grubbs' catalyst and microcapsules were embedded in the matrix, termed *microcapsule* samples.

Grubbs' first generation catalyst (Sigma-Aldrich) was recrystallised via a non-solvent addition method and wax-encapsulated for protection, to form 10 wt% Grubbs' catalyst in wax microspheres of 200 μm average size. The microspheres were added into the epoxy matrix in a 5 wt% concentration. In order to minimise costs, the microspheres were localised around the crack plane region (Fig. 4.1) [5]. For the microcapsule samples, microcapsules with typical diameters of 100-200 μm were prepared, containing DCPD healing agent. These were added into the epoxy matrix in a 5, 10 or 20 wt% concentration. The epoxy was degassed, cured in silicone rubber moulds for 24 hr at room temperature, and post-cured at 35°C for a further 24 hr. After post-curing, a sharp pre-crack was made by tapping a razor blade into the moulded starter-notch.

The TDCB samples were mounted in a load frame with two pins and loaded in tension at a constant displacement rate of 5 μm/s. At failure, a crack propagated horizontally along the side-grooves, along the full length of the specimen, fracturing

the sample in two halves and releasing healing agent from the microcapsules. The SMA wires have a tensile strength of 1 GPa, and a maximum elongation of 7% before failure, so they remained intact when the sample failed. The peak load at failure was recorded, and the virgin fracture toughness was calculated from it (Eq. 4.1).

The two sample halves were then removed together from the load frame. Following this, the SMA wires were mechanically clamped at the points where they exited the TDCB sample. This was achieved by placing them between two aluminium plates with dimensions of 70 mm by 20 mm, which were then clamped together using nuts and bolts. This eliminated any influence of the quality of the SMA interfacial bonding on the present measurements. The DCPD was delivered to the crack either by manual injection or by embedded microcapsules, depending on the sample type. The SMA wires were then activated with a DC current of 0.5 A per wire for 30 min (§4.2.2), corresponding closely with the room-temperature gel time of the DCPD (§4.2.2). During activation, the temperature of the wires and local matrix reached 80 °C, and each wire generated an axial recovery force of 4.5 N (240 MPa axial stress; (Fig. 3.10) which acted to close the crack faces. Following the activation period, the SMA clamps were removed and the sample left at room temperature for a further 24 hr.

After healing, the crack face separation of each sample was determined using an optical microscope. The crack opening was measured at three locations per sample and averaged. The SMA wires were then carefully debonded by manually applying a force to them, and fully removed from the matrix. The samples were then re-tested to failure under the same conditions as for the virgin material, and the healed peak load recorded.

The self-healing performance of the material can be quantified by the healing efficiency (Eq. 2.2). However, the virgin fracture toughness depends on microcapsule size and concentration, and so η does not reflect the healing performance alone. Following Rule *et al.* [5], healing performance was, therefore, evaluated by directly comparing the healed peak loads. However, average virgin peak load values are provided (Table 4.1) so that the healing efficiencies can be readily calculated.

4.2.2 SMA heat cycle

As stated in §4.2.1, the SMA wires in the TDCB samples were thermally-activated by resistive heating with a current. From Fig. 3.6, the wires should be heated to 80°C for full activation. To determine the current required to do so, a TDCB sample with three embedded SMA wires and a small thermocouple attached to each of the three wires, also embedded in the matrix, was made. Current was passed through the wires and the temperature was recorded over a period of time. This was repeated for different applied currents.

4.2.3 Fracture behaviour of polyDCPD healing agent

The fracture toughness of polyDCPD was evaluated by compact tension (CT) testing following ASTM standard D 5045–91a (Fig. 4.2). To prepare the samples, DCPD was mixed with 5 wt% Grubbs' catalyst wax microspheres and cast in an aluminium mould to form a polymer plate. Two types of samples were prepared to simulate

the different types of healing cycles. The first plate was allowed to polymerise at room temperature for 24 hr. The second plate was placed in an oven at 80°C for the first 30 min after mixing to simulate the effects of the heating cycle of the SMA wires (§4.2.2), and then left at room temperature for 24 hr.

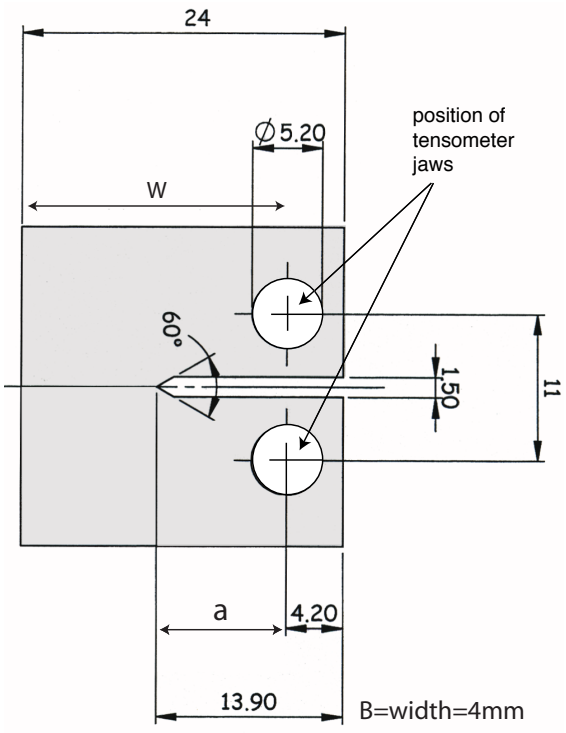

Figure 4.2: Compact tension (CT) sample geometry. All distance units are mm.

Four CT samples were machined from each plate. Each sample notch was sharpened by scoring with a razor blade, forming a pre-crack. The pre-crack length was measured for each sample, and was typically 0.1-0.3 mm. The samples were then individually mounted in a tensile tester and loaded in tension at a constant displacement rate of 5 μm/s, until failure, recording the force (P) as a function of time. The characteristics of the force displacement plots of the two sample types were then compared. The fracture characteristics of the two sample types were also compared with scanning electron microscope (SEM) images of the fracture planes.

For the samples that followed linear elastic fracture mechanics, their fracture toughness, K_{IC} (MPa m$^{1/2}$), was calculated from the expression

$$K_{IC} = \frac{P_C}{BW^{1/2}} f(x) \tag{4.2}$$

where, P_C (N) is the critical load for crack propagation, B (m) is the sample width, W (m) is the distance between the centre of the loading slot and the back end of the sample, and

$$f(x) = \frac{(2+x)(0.886 + 4.64x - 13.32x^2 + 14.72x^3 - 5.6x^4)}{(1-x)^{3/2}} \tag{4.3}$$

where $x = a/W$, $0.2 < x < 0.8$ and a includes the length of the pre-crack, as given by the ASTM standard D 5045–91a.

4.2.4 Microcapsule thermal stability

The thermal stability of the microcapsules was assessed by thermogravimetric analysis (TGA). Samples of microcapsules (10-20 mg) were weighed in a 150 μl ceramic crucible and then placed in the TGA. The TGA was heated from 25°C to 600°C at a rate of 10°C/min, under a controlled nitrogen environment, while continuously monitoring the sample mass.

4.3 SMA wire influence on virgin fracture toughness

In order to isolate the effect of SMA wires on healing performance it was first necessary to investigate their influence on the fracture toughness of the virgin epoxy material. TDCB samples were prepared and tested as described in §4.2.1. The mean peak loads of the virgin samples, and their corresponding fracture toughnesses (Eq. 4.1), are summarised in Table 4.1. The values for the samples with and without SMA wires are within one standard deviation of one another for all sample types. Thus, any improved self-healing performance reported here is due to improved healing of the crack, and not to any toughening effect of the embedded SMA wires.

Table 4.1: Effect of SMA wire presence on epoxy matrix properties. The values without SMA wires were obtained by Rule *et al.* [5]. The concentrations of DCPD microcapsules and Grubbs' microspheres in the matrix were 10 wt% and 5 wt%, respectively. Samples containing *localised* capsules means the capsules were located around the crack region only, about 3 mm on each side of the plane. Samples containing *non-localised* capsules means the capsules were present in the entire matrix.

Sample	With SMA wires		Without SMA wires	
	Virgin peak load [N]	K_{IC} [MPa $m^{1/2}$]	Virgin peak load [N]	K_{IC} [MPa $m^{1/2}$]
Epoxy	68.6	0.77 ± 0.10	77.7	0.87 ± 0.12
Epoxy/Grubbs'	78.5	0.88 ± 0.14	78.5	0.88 ± 0.10
Epoxy/Grubbs'/ localised capsules	131.7	1.47 ± 0.15	123.2	1.38 ± 0.10
Epoxy/Grubbs'/ non-localised capsules	95.4	1.07 ± 0.12	96.4	1.08 ± 0.15

4.4 SMA heat cycle

The TDCB sample with embedded thermocouples was tested as described in §4.2.2. Thermal equilibrium was achieved after about ten minutes, and a current of 0.5 A per wire was sufficient to raise the wire temperature to 80°C (Fig. 4.3). The resistivity of a single SMA wire at 80°C is 100 $\mu\Omega$ cm, corresponding to a resistance of 0.56 $\Omega\,cm^{-1}$. So, at 0.5 A current, a power of about 0.14 W/cm of wire is dissipated.

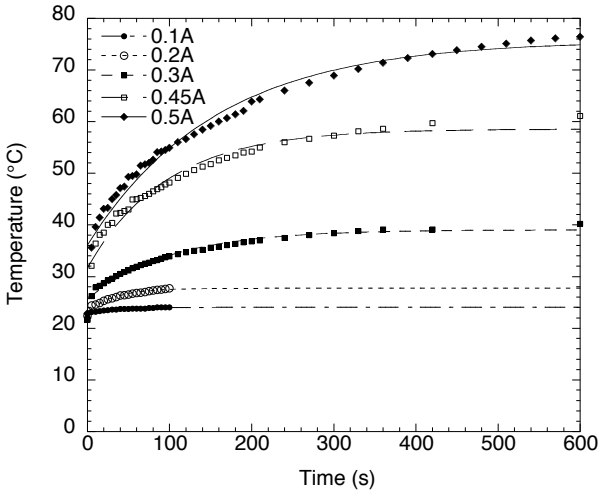

Figure 4.3: Equilibrium temperature of the activated SMA wires embedded within the TDCB sample, for different applied currents.

4.5 Optical measurements of crack closure

The crack face separation was measured by optical microscopy for several fractured TDCB samples containing SMA wires, both before and during the wire activation. A sample was placed under an Olympus BX61 optical microscope, and the wires were activated with 0.5 A current per wire. Images of the crack were recorded and the crack face separation was evaluated using the analySIS Image Processing software. An example image of a crack before and after SMA activation is shown in Fig. 4.4, and Fig. 4.5 shows (a) a measurement of the crack opening in a pure epoxy sample with SMA activation time, and (b) the corresponding percent reduction in crack opening. A large reduction of crack opening was achieved within approximately 60 s.

Two sets of samples were made: the first consisted of epoxy with SMA wires, and the second of epoxy and localised wax-protected Grubbs' catalyst microspheres ($360 \pm 40\,\mu$m diameter) with SMA wires. The samples were fractured in the standard fashion, and the crack opening was measured at each of the three wire locations. The average of the three measurements was taken for each sample, giving an average crack opening of $160 \pm 35\mu$m (range: 80–300 μm) before SMA activation. The SMA wires were then activated, and the crack opening re-measured at the same three locations. These measurements were repeated on four samples without catalyst microspheres and four samples with catalyst microspheres. Once the SMA wires were activated, the average crack opening was $15 \pm 3\,\mu$m (range: 8–23 μm) for samples without catalyst, and $18 \pm 4\,\mu$m (range: 3–35 μm) for samples with catalyst. Activation of the embedded SMA wires reduced the crack face separation by about an order of magnitude. After SMA activation, the crack volumes were 1.8 μl and 2.1 μl for the samples without and with Grubbs' catalyst, respectively. The reduction in crack volume suggests that full healing can be achieved with relatively small volumes of DCPD healing agent (around 2 mg cm^{-2}, c.f. Fig. 2.8).

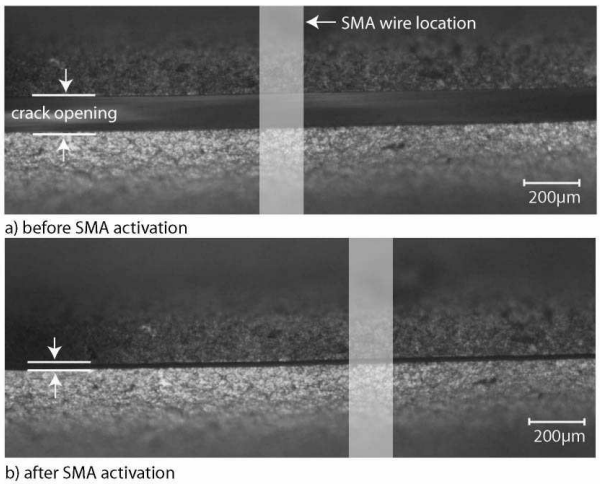

Figure 4.4: Optical microscope images of a crack in an epoxy/SMA TDCB sample, (a) before SMA wire activation and (b) after SMA wire activation. The crack opening at this location was reduced from 120 μm to about 17 μm.

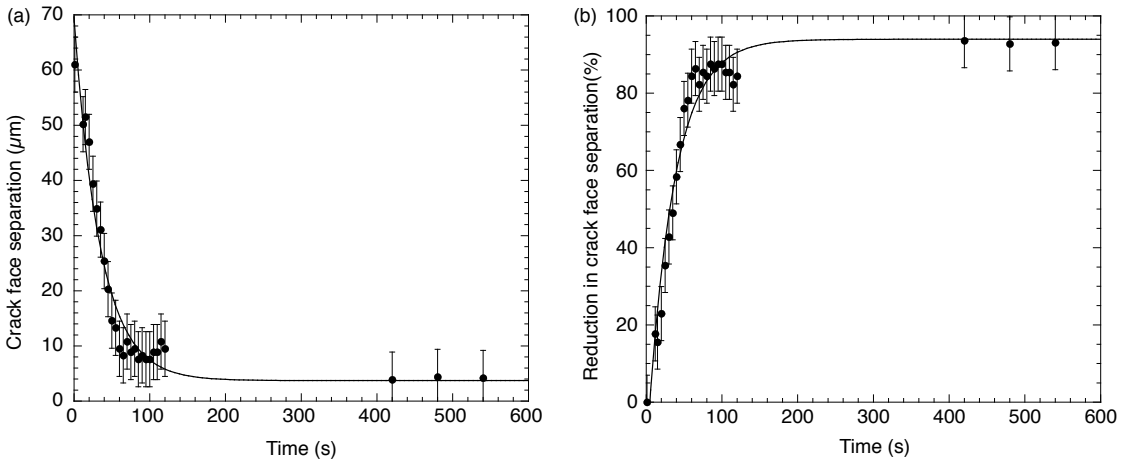

Figure 4.5: (a) Crack face separation versus SMA activation time and (b) percent reduction in crack face separation versus SMA activation time.

4.6 Fracture behaviour of PolyDCPD healing agent

A total of eight compact tension samples of DCPD polymerised with 5 wt% Grubbs' catalyst wax microspheres were prepared and tested. Of these, four were polymerised at room temperature for 24 hr, while the other four were initially placed in an oven at 80°C for 30 min. Figure 4.6 shows representative load-displacement results for each sample type. The samples polymerised at room temperature exhibited non-linear fracture behaviour, indicative of incomplete polymerisation, with an average fracture load of 89.0 ± 3.1 N. The samples polymerised at 80°C exhibited linear fracture characteristics, with an average fracture load of 123.0 ± 3.3 N, corresponding to a fracture toughness of $2.08 \pm 0.06\,\mathrm{MPa\,m^{1/2}}$ (Eq. 4.2).

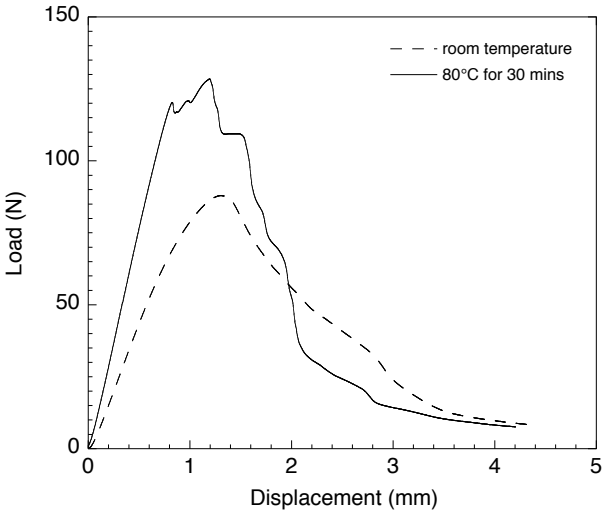

Figure 4.6: Representative load versus displacement compact tension tests of polyDCPD after polymerisation (a) at room temperature for 24 hr and (b) at 80°C for 30 min followed by 24 hr at room temperature.

In addition to an increased fracture load, the samples polymerised at 80°C exhibited a more brittle fracture behaviour. The load-displacement curve in Fig. 4.6 is linear up to the fracture point in comparison to that of the samples polymerised at room temperature. Figure 4.7 shows SEM images of the fracture surfaces of the two samples, taken with a Philips XL30 ESEM-FEG. The fracture surface of the room temperature sample is highly textured, with evidence of tearing and plastic deformation. In contrast, the fracture surface of the 80°C sample is smooth and glass-like, with relatively little texture. These SEM images support the findings in Fig. 4.6, and reinforce the conclusion that the heating effect of the SMA wires contributes significantly to the overall healing performance. However, no direct correlation between the properties of the bulk polyDCPD and the polyDCPD film formed *in situ* in TDCB samples can be drawn. Fracture toughness and associated mechanical performance in inherently dependent on the concentration of catalyst and the polymerisation temperature—two quantities that are uncontrolled during *in situ* healing. The measurements presented in this section, therefore, serve only as an indication of the influence of heating on the fracture behaviour.

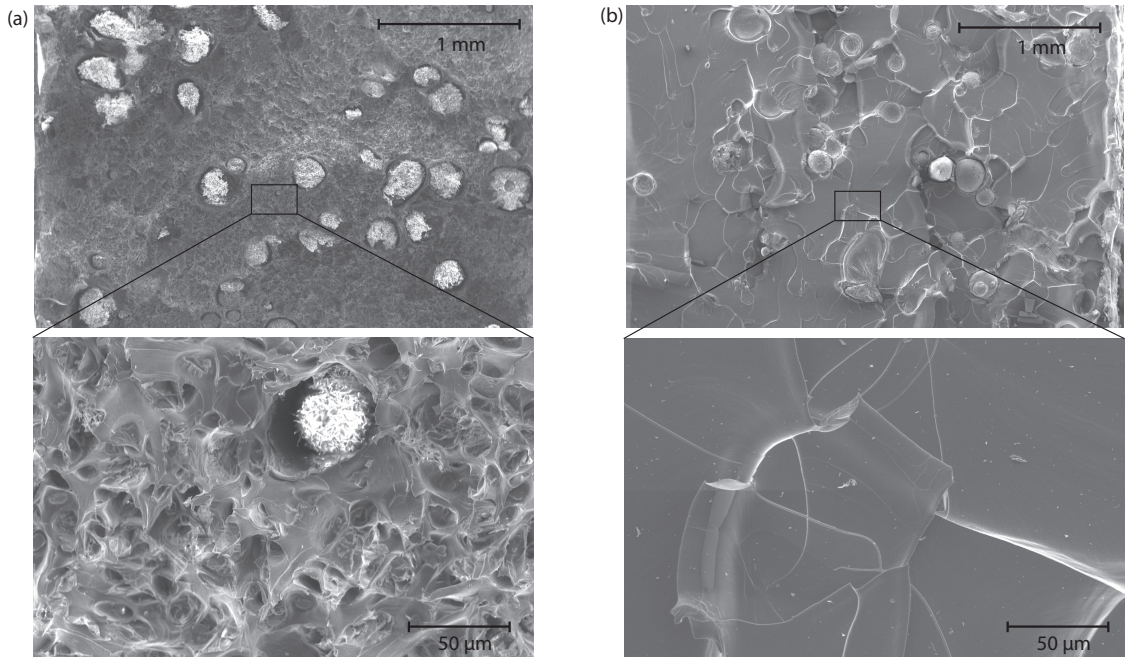

Figure 4.7: Scanning electron microscope images of the fracture surface of the poly-DCPD after polymerisation at (a) room temperature (20°C) for 24 hr and (b) 80°C for 30 min, followed by room temperature (20°C) for 24 hr. The fracture surface of the room-temperature sample is highly textured, with evidence of tearing and plastic deformation, while the surface of the sample cured at 80°C is smooth and glass-like, indicating a brittle fracture. The spherical features in both images are partially undissolved Grubbs' catalyst wax microspheres.

4.7 Injected samples

4.7.1 Healing performance

For these tests the TDCB samples included three SMA wires, wax-protected Grubbs' catalyst microspheres of $300 \pm 30\,\mu$m diameter and injected healing agent. A representative result is shown in Fig. 4.8. In the virgin test the pre-crack advanced slightly at about $700\,\mu$m displacement and 80 N load. The crack propagated unstably at about $850\,\mu$m displacement and 85 N load, before arresting at an SMA wire. Continued loading lead to a final rapid propagation of the crack through the entire sample at about $1170\,\mu$m displacement and 65 N load. After the virgin test, $20\,\mu$l of DCPD healing agent were injected into the crack. The SMA wires were then activated as described previously, and the sample allowed to heal for 24 h. They were then carefully debonded and removed from the matrix by hand. Upon re-testing, the sample had recovered a large fraction—about 98 %—of the virgin load-bearing capacity.

This procedure was repeated for a series of samples involving 0, 1, 2, 5, 10, 14 and $20\,\mu$l of injected DCPD. The averaged healed peak loads are shown in Fig. 4.9, together with the fit to the Rule *et al.* measurements for room temperature healing without SMA wires (Fig. 2.8). A clear improvement in healed peak load resulted when SMA wires were present; the healed peak loads were increased by about a factor 1.6 relative to the samples without SMA wires. Moreover, a dramatic improvement was achieved for the smallest quantities of healing agent delivered (1 and $2\,\mu$l), as anticipated from the reduced crack opening measurements.

Representative virgin and healed load-displacement curves for samples with a fill factor well above unity, both without and with SMA wires, are compared in Fig. 4.10. Consistent with results reported in [33], the sample healed without SMA wires—at room temperature—exhibited a non-linear stress-strain behaviour. This nonlinearity was attributed to incomplete polymerisation, and to a plasticisation of the polyDCPD film by the dissolved wax [33]. However, the samples healed with SMA wires—at elevated temperature—showed linear behaviour, similar to the virgin measurements (Fig. 4.10). The raised temperature in the SMA samples increased the rate and extent of dissolution of the wax, which in turn lead to a higher degree of polymerisation of the DCPD than at room temperature, producing a film with superior mechanical and adhesive properties. This is supported with scanning electron images of the fracture surfaces of samples healed without and with SMA wires (Fig. 4.11a and Fig. 4.11b, respectively). In the case of the sample healed at room temperature (Fig. 4.11a) the polyDCPD film appears flaky, and has become disconnected from the epoxy matrix in many locations. In contrast, the polyDCPD film in the sample healed with SMA wires (Fig. 4.11b) is more continuous, and remains well-adhered to the fracture plane. These findings are consistent with Fig. 4.7.

4.7.2 Effect of crack volume

The healing performance is expected to depend not only on the amount of healing agent delivered, but also on the total volume of the closed crack, which shows considerable variability from sample to sample. Thus, *fill factor* (γ) is defined as

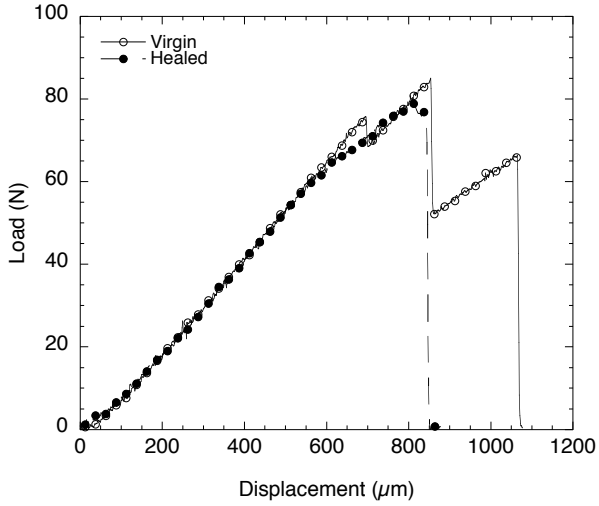

Figure 4.8: Example TDCB fracture test result for a sample with injected healing agent. The virgin sample was loaded in mode I to failure, and then removed from the load frame. After injecting 20 μl DCPD, the SMA wires were activated for 30 min. The sample then healed at room temperature for a further 24 hr, after which it was re-tested to failure. For this sample, about 98 % of the virgin peak load was restored.

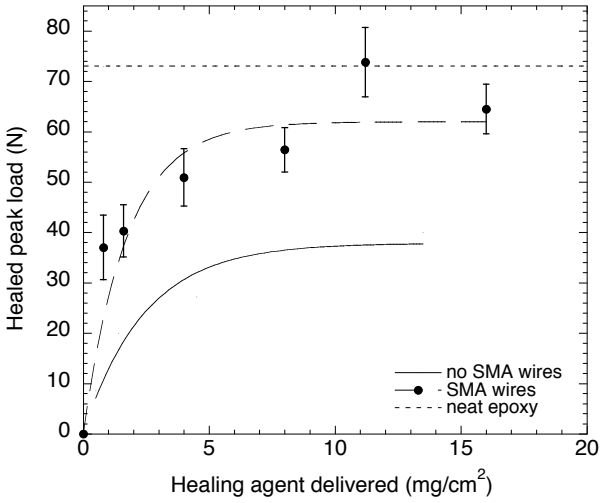

Figure 4.9: Summary of the healed peak loads of samples with injected healing agent (each data point represents the average of 4–10 identically-prepared samples). The circles denote average values for samples healed with embedded SMA wires. The wires were activated for 30 min following injection of the healing agent and then healing occurred for an additional 24 hr at room temperature. The solid curve is taken from Fig. 2.8, and represents healing without SMA wires at room temperature for 24 hr.

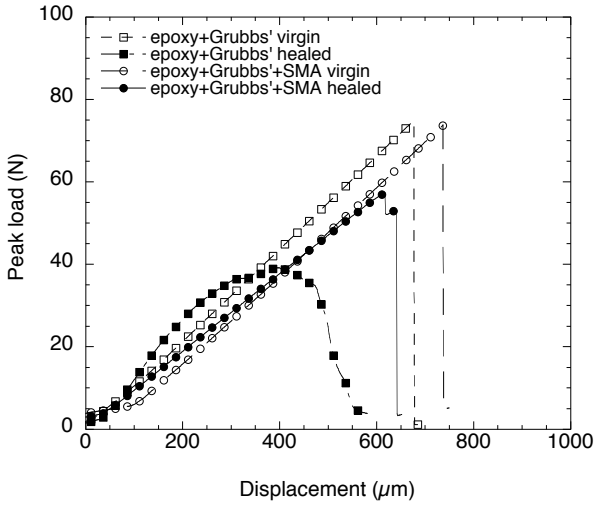

Figure 4.10: Representative healed load-displacement curves for TDCB samples, without and with embedded SMA wires.

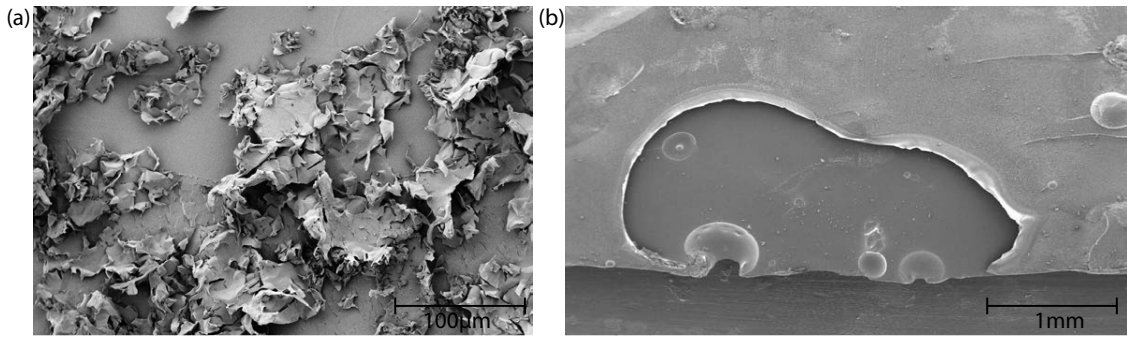

Figure 4.11: SEM image of a fracture surface of a TDCB sample injected with healing agent and healed at (a) room temperature, without SMA wires and (b) 80°C, with SMA wires.

the volume of delivered healing agent divided by the total healed crack volume, i. e.

$$\gamma = \frac{V_h}{V_c} \tag{4.4}$$

where V_h and V_c are the volume of the delivered healing agent and of the closed crack, respectively. The fill factor of each sample was determined as follows. The amount of healing agent delivered per unit crack area, D_h ($\mathrm{g\,cm^{-2}}$), is given by

$$D_h = \rho_m \, \phi \, d_c \tag{4.5}$$

where ρ_m is the density of the matrix ($1.16\,\mathrm{g\,cm^{-3}}$), ϕ is the weight fraction of microcapsules and d_c (cm) is the diameter of the microcapsules [5]. The volume of delivered healing agent is then $V_h = D_h \cdot A/\rho_h$, where A ($\mathrm{cm^2}$) is the crack area and ρ_h is the density of DCPD ($0.98\,\mathrm{g\ cm^{-3}}$). The crack volume is $V_c = A \cdot w$ where w (cm) is the crack separation, as measured by optical microscopy. The fill factor is then given by

$$\gamma = \frac{V_h}{V_c} = \frac{\rho_m \, \phi \, d_c}{\rho_h w} \tag{4.6}$$

The crack opening, and hence volume, was measured using optical microscopy[1]. In Fig. 4.12, the individual data for 1, 2, 5 and $10\,\mu$l of DCPD injected are plotted versus the calculated fill factors. Notwithstanding the large sample-to-sample variations, the healed peak load for all injection volumes show qualitatively similar behaviour, namely a plateau of the healed peak load around 50–60 N above a fill factor of unity. The $1\,\mu$l data do not reach complete fill and so do not show this plateau. The combined data for all cases are shown in Fig. 4.13. The general trend of increasing healed peak load up to a fill factor of unity is consistent across all the data.

4.7.3 Factors contributing to the improved performance of SMA samples

The results clearly indicate that improved self-healing performance is obtained with the addition of SMA wires and their activation during healing. Two main factors can be identified that lead to this improved performance. First, activation of the SMA wires leads to a large reduction in total crack volume and a corresponding increase in the fill factor (γ). In this case improvements in healed peak load could be expected for cases where $\gamma \leqslant 1$ without activation. Secondly, activation of the SMA wires by resistive heating raises the local temperature of the matrix and the healing agent in the crack. In this case the healed material in the crack may be more completely polymerised, with superior mechanical and adhesive properties.

To elucidate the relative impact of each of these factors separately, two further tests were performed. In the first, the effect of reduced crack volume was isolated by preparing TDCB samples identical to those used previously, but without SMA wires.

[1]Some of the data in Fig. 4.9 cannot be re-plotted versus fill factor since the crack opening is unknown.

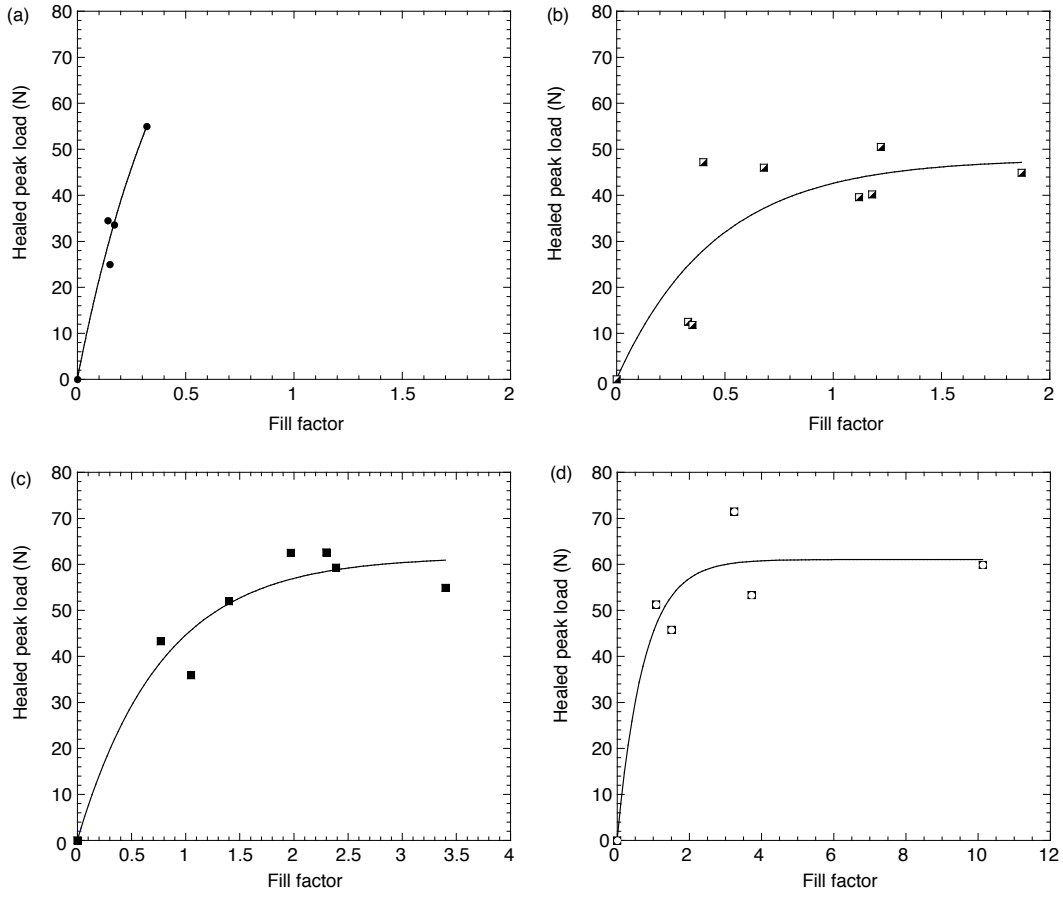

Figure 4.12: Healed peak load versus fill factor for TDCB samples injected with (a) $1\,\mu$l, (b) $2\,\mu$l, (c) $5\,\mu$l and (d) $10\,\mu$l of DCPD. Each point represents a single measurement.

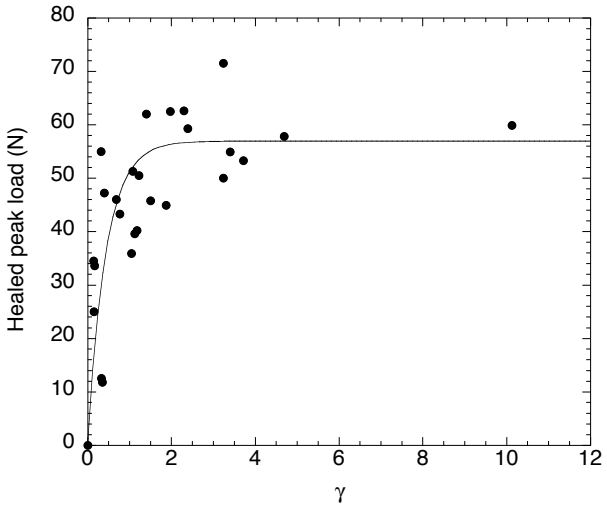

Figure 4.13: Healed peak load versus fill factor for all injected SMA samples.

These samples were fractured and subsequently 2 or 5μl of DCPD were injected into the crack. The sample halves were brought back together, registered as closely as possible and then compressed using elastic bands, exerting a compressive force of a few Newtons, to hold the crack closed. The samples were allowed to heal for 24 hr at room temperature. After healing, crack openings were all below 10 μm, and the corresponding fill factors were all well above unity. Healed peak loads for these samples are shown in Figure 4.14, averaging 36.8 ± 1.7 N for the 2 μl samples and 37.9 ± 2.1 N for the 5 μl samples. In comparison, Rule *et al.* obtained healed peak loads of $\sim 18.5 \pm 5$ N and $\sim 30 \pm 5$ N, respectively, for identical samples where no closure force was applied[2] (Fig. 2.8) [5].

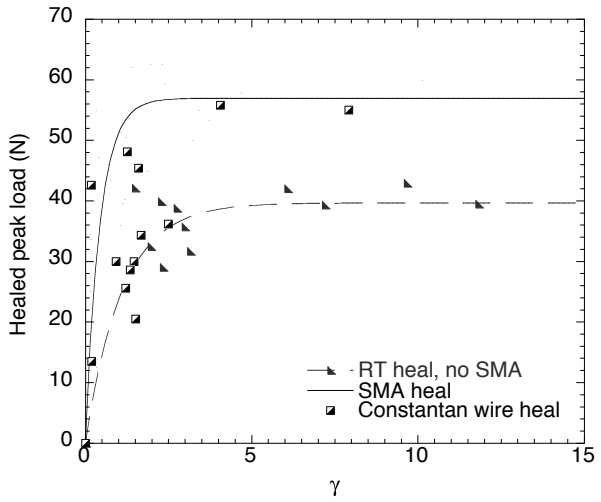

Figure 4.14: Healed peak load versus fill factor for samples (a) without SMA wires, healed at room temperature and held together with an elastic band (b) with 200 μm diameter constantan wires, healed with the same heating cycle for the SMA wires and (c) with SMA wires, healed in the standard fashion.

In another set of experiments, the effect of heating was isolated by preparing a set of TDCB samples in which the three SMA wires were replaced with three 200 μm-diameter constantan wires—a non shape-memory copper-nickel based alloy wire control. After virgin fracture, 2, 5, 15 or 20 μl of DCPD were injected into the crack and the sample halves were brought back together by hand. The constantan wires were free to slip through the matrix as the crack faces were brought back into contact, due to a thin layer of conducting paste on their surface. The constantan wires were then heated resistively for 30 min, to simulate the heat produced by the activated SMA wires. The SMA wires and the constantan wires have a resistance of $56.6\,\Omega\,\mathrm{m}^{-1}$ and $15.6\,\Omega\,\mathrm{m}^{-1}$, respectively. As a result, the constantan wires were heated with 0.95 A per wire for 30 min, so that the power dissipated in the two cases was the same. After this 30 min period the samples were allowed to sit at room temperature for a further 24 hr. The fracture results for these tests are also shown in Fig. 4.14, together with the curve for all SMA-healed samples from Fig. 4.13. The

[2]For this sample geometry, 1 μl of injected DCPD corresponds to $0.8\,\mathrm{mg\,cm}^{-2}$ delivered to the crack plane.

constantan-healed samples with a low fill factor had a maximum healed peak load of around 30 N. However, as the fill factor increased, the healed peak loads of the constantan-healed samples reached the 60 N plateau value exhibited by the SMA-healed samples. This is consistent with expectations, namely that provided the fill factor is above unity, heating the samples improves the healed peak loads, by increasing the degree of polymerisation of the DCPD healing agent.

These measurements are consistent with observations by Kessler *et al.*, who measured the effect of temperature on the healed interlaminar fracture toughness in a delaminated self-healing composite [50]. They prepared samples with the same EPON 828/DETA matrix used in this study, and plain-weave carbon fibre reinforcement. The samples were pin-loaded in tension and their interlaminar fracture toughness was determined. The samples were healed for 48 hr, either at room temperature or at 80°C, and re-tested. Room temperature samples yielded a healing efficiency of nearly 50%, and those healed at 80°C had an average healing efficiency of 66%, with a maximum over 80%, corresponding to an increase of a factor 1.6.

4.8 Microcapsule samples

4.8.1 Microcapsule thermal stability

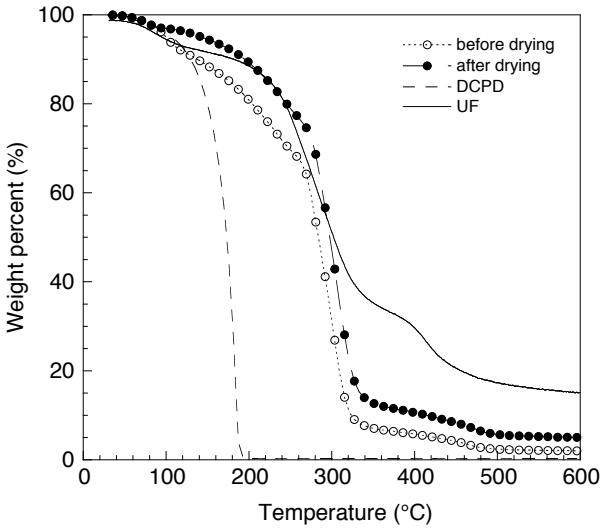

Figure 4.15: Measurement of the normalised weight versus temperature of samples of microcapsules and their components: (a) microcapsules without prior drying to remove water (hollow circles), (b) pre-dried microcapsules (solid circles), (c) dicyclopentadiene (dashed line), and (d) urea-formaldehyde shell wall (solid line). Each sample initially weighed around 10-20 mg and the heating rate was 10°C/min.

Representative weight loss curves for microcapsules and components are presented in Fig. 4.15. The DCPD monomer rapidly lost weight between 150-180°C, corresponding to the boiling point of DCPD (170–172°C). However, when DCPD was encapsulated in a UF shell wall, rapid weight loss did not occur until 300°C—

the temperature at which the UF shell wall began to degrade. These observations confirm that the microcapsules were predominantly well-formed and robust.

Although the rapid weight loss of the microcapsule samples occurred near 300°C, a gradual decrease in mass was observed between 100-280°C. Comparing capsules that were pre-dried with those that were not, there is clear evidence that part of the weight loss in this interval was due to evaporation of water. In addition, the UF shell material samples also showed loss in mass over the same temperature range, suggesting that some weight loss may have been due to evaporation of high volatility compounds from the UF walls. Since TGA measurements are performed on batch samples, some small fraction of microcapsules that were poorly formed could also have lead to premature weight loss. Nevertheless, over the temperature range of interest (< 80°C) these microcapsules retained the vast majority of their content.

4.8.2 Healing performance

TDCB samples containing microcapsules both without and with SMA wires were prepared and then fractured, healed and re-fractured as described in §4.2.1. Representative results of both are shown in Fig. 4.16. For samples without SMA wires the results are compared directly to those of Rule *et al.* [5] in Table 4.2; the curve for the sample healed without SMA wires in Fig. 4.16 is one such measurement. It should be noted that this particular healing event does not represent the maximum room temperature healing performance; the fill factor of this specific sample was 0.6, and was chosen so that the results here could be directly compared to those by Rule *et al.* in [5]. The maximum healed peak load for room temperature samples, achieved when the fill factor is at least unity, is about 40 N (Fig. 4.14), corresponding to a healing efficiency of ∼50%. The two sets of measurements of healed peak load in Table 4.2 are in reasonable agreement, although the Kirkby measurements are systematically about 25–30% lower. One possible explanation is that these particular samples had larger catalyst microspheres ($510 \pm 10\,\mu$m versus $220\,\mu$m for Rule *et al.*), which would alter the dissolution kinetics of the catalyst in the DCPD.

Table 4.2: Comparison of healed peak fracture loads with those of Rule *et al.* [5] for TDCB samples containing microcapsules but no SMA wires. The diameter of the microcapsules in the Kirkby samples was $114 \pm 6\,\mu$m.

Capsule concentration [wt %]	Healing agent delivered [mg cm^{-2}]	Healed peak load [N]	
		Kirkby data	Rule data
5	0.66	4.7 ± 1.1	8.0
10	1.32	8.8 ± 1.6	12.0
20	2.64	18.4 ± 2.6	24.5

For TDCB samples containing both SMA wires and microcapsules, the healed response displayed a linear elastic brittle-type fracture, similar to the virgin response (Fig. 4.16). The samples without SMA wires exhibited a more plastic-like fracture, indicative of incomplete polymerisation when healing at room-temperature alone. These observations are consistent with the fracture characteristics of the polyDCPD healing agent (§4.6). The fracture surface of a well-healed sample is shown in

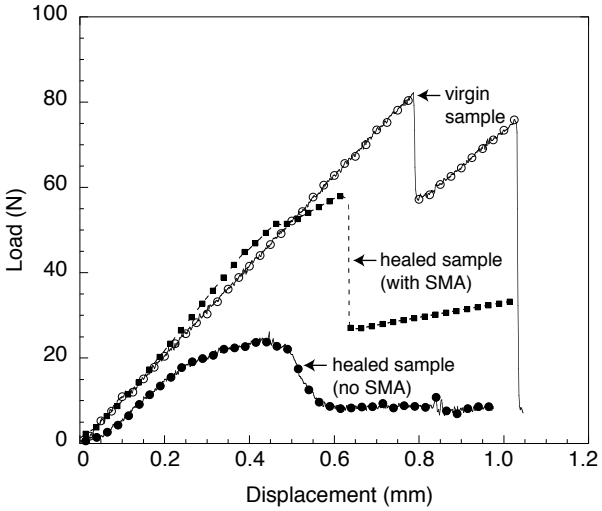

Figure 4.16: Representative curves of load versus displacement for TDCB samples containing 20 wt% microcapsules: (a) virgin sample, (b) healed sample without SMA wires (fill factor ∼0.6) and (c) healed sample with SMA wires (fill factor 1.7).

Fig. 4.17, and displays a polyDCPD film that is continuous and crisp-edged, characteristic of a strong heal.

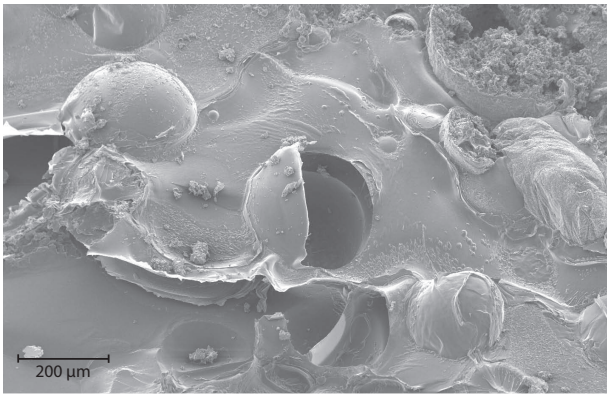

Figure 4.17: Crack plane image of a well-healed microcapsule/SMA sample. The polyDCPD film covers most of the imaged surface. A Grubbs' catalyst wax microsphere is present in the top right corner of the image.

For samples with SMA wires, 20 wt% microcapsules with diameters ranging between 140 and 205 μm were used. The fill factor of the healed samples (Eq. 4.6) varied from about 0.3 to almost 7 in one case, corresponding to crack separations ranging from 185 to 8 μm (58 μm mean and 39 μm standard deviation for all samples). Fill factors above unity indicate that more healing agent was delivered than necessary to fill the crack volume, assuming perfect filling efficiency. In the case of TDCB samples, excess healing agent flows out of the crack plane along the edges of the crack.

Around 40 TDCB samples with microcapsules and SMA wires were tested. The

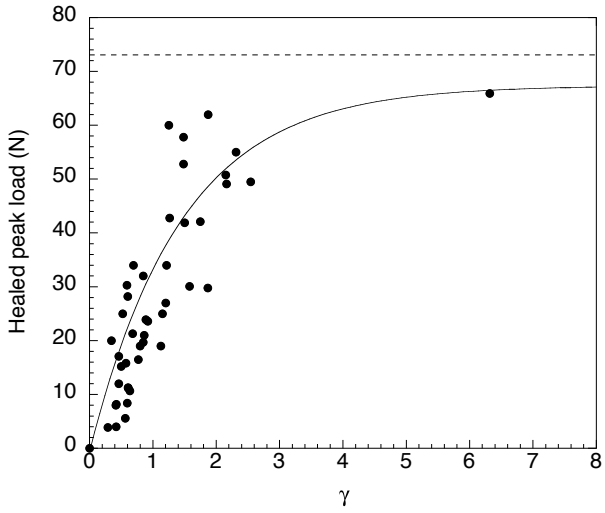

Figure 4.18: Healed peak load versus fill factor for healed TDCB samples with micro-encapsulated healing agent and SMA wires. The solid curve is a general fit to the data. The dashed line indicates the mean peak load of the virgin samples.

results are shown in Fig. 4.18. The healed peak load reached a maximum around 60 N, roughly 80% of the peak load of the virgin material. The data indicate that fill factors of at least two are required to reach maximum healing performance, an observation consistent with tests on samples where the healing agent was manually injected.

4.9 Discussion

Embedding SMA wires that bridge the fracture plane and activating them during the healing process has been shown to lead to significant improvements in the performance of self-healing polymers with both injected and microencapsulated healing agent. The healed peak fracture loads were increased from 38 N to 60 N on average when three SMA wires were embedded orthogonal to the crack plane of TDCB fracture samples and activated by resistive heating to 80°C for 30 min following the virgin fracture event. This corresponds an increase in healing efficiency from 49% to 77% with SMA wires.

The improved performance is due to two factors: a decreased crack volume and, consequently, an improved filling efficiency with a given quantity of healing agent; and improved mechanical properties of the polymerised healing agent, due to the heating effect of the SMA wires, which improves cross-linking during polymerisation. Furthermore, fill factors of at least two are required to reach the maximum healing efficiency. These results suggest that practical applications should aim for an overdelivery of healing agent of at least a factor of two to ensure complete filling of the crack and the highest healing efficiency.

Chapter 5

SMA composite processing

5.1 Introduction

In this chapter, a liquid composite moulding processing schedule suitable for a composite with embedded SMA wires is developed. In practical applications, the Active Sensing and Repair Composite will be post-cured at temperatures exceeding the activation temperature of the SMA wires. This means that an initially pre-strained wire, or a wire with a two-way shape memory effect, embedded in the composite structure will recover its original shape during the processing. Currently, for laboratory-scale production, this issue is overcome by using an external clamping frame that prevents the SMA wires from contracting [161]. However, this is cumbersome and time-consuming, and is, therefore, not suitable for an industrial-scale process. One group has developed a processing method that does not require a frame [162]. In their work, the wires are heavily cold-worked before being embedded, which has the effect of raising the reverse transformation temperature of the wires above the processing temperature. Once embedded, the wires are flash annealed at 350°C using a current, to restore their original transformation temperatures. This high temperature, however, though only applied for a short period of time, could be detrimental to the mechanical properties of the host material.

The goal in this chapter is to develop a post-cure schedule that does not require a frame or involve a high-temperature anneal, where the SMAs remain well-bonded to the matrix throughout processing. The post-cure schedule must meet several requirements: (a) the final glass transition temperature (T_g) of the epoxy matrix should be greater than the upper activation temperature (A_f) of 80°C of the SMA wires. This will ensure that there is no softening of the surrounding matrix when the SMA wires are fully activated, (b) the post-cure temperature should not exceed 110°C, to remain below the de-activation temperature of about 130°C of the Grubbs' catalyst, which will ultimately also be embedded in the epoxy, (c) the selected post-cure schedule should not be detrimental to the mechanical properties of the epoxy or to the SMA/epoxy interfacial quality, and (d) repeated and reproducible activation of the SMA wires embedded in the final material should be possible, without any significant debonding occurring.

These requirements are addressed through three stages of experiments. In the first stage, a post-cure schedule that produces an epoxy with the desired thermal and mechanical properties is selected. Pure epoxy samples are made using four dif-

ferent post-cure schedules. Their glass transition temperatures are determined with differential scanning calorimetry (DSC) and their tensile properties with mechanical tests on dog-bone samples. In the second stage, both single-wire and multi-wire SMA-epoxy composite samples are made. The influence of the SMA wires on the residual strain in the epoxy matrix after processing is first evaluated, using embedded optical fibre Bragg grating sensors. The quality of the interface between the SMA and the epoxy is then determined through both single-wire pull-out tests and visual observation. The intrinsic interfacial shear strengths are calculated from the pull-out measurements and are compared with the modelled shear stresses exerted at the interface by an activated SMA wire. Following this, tests to verify that the SMAs remain bonded to the matrix during cyclic activation are carried out on multi-wire samples in the U-holder (§3.2.3, Fig. 3.8). Finally, in the third stage the rheological properties of the epoxy system are determined to evaluate its suitability for a liquid composite moulding route. The viscosity of the resin should be sufficiently low so that it can penetrate fibre bundles, and should remain as such for a suitable length of time to fully impregnate them.

5.2 Experimental techniques

5.2.1 Epoxy properties

Differential scanning calorimetry

Both the total heat flow associated with the epoxy curing and the glass transition temperature of the post-cured epoxy samples were determined with DSC. A sample of a few milligrams was sealed inside an aluminium crucible, which was then placed in the measurement chamber of a TA Instruments DSC Q100, alongside a reference. The sample and reference were heated from 10°C to 200°C, cooled back to 10°C using liquid nitrogen coolant and heated a second time to 200°C, all at a rate of 10°C/min, under a continuous gaseous nitrogen purge with a flow rate of 25 ml/min. The data was recorded using the Q-Series Explorer software.

Tensile testing

Epoxy samples with a dog-bone geometry were prepared according to ASTM standard D638 (Fig. 5.1). They were cast eight at a time in a metallic mould, cured at room temperature for 24 hr and post-cured using one of the cycles in Table 5.1. A sample was then mounted in the tensile tester on a 100 kN load cell, and a 10 N tensile load was applied to it to avoid buckling. A type 411.S03 extensometer with a gauge length of 50 mm was positioned on the central section of the sample (Fig. 5.2). The sample was pulled in tension at 1 mm/min, and the load-displacement data was recorded, which was then converted into stress-strain data. The Young's modulus and the ultimate tensile strength were determined from these measurements. This test was repeated up to three times per sample type, and the data averaged.

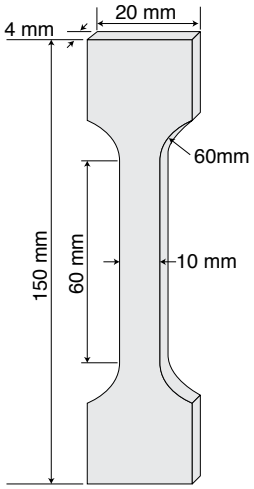

Figure 5.1: Epoxy dog-bone tensile test sample.

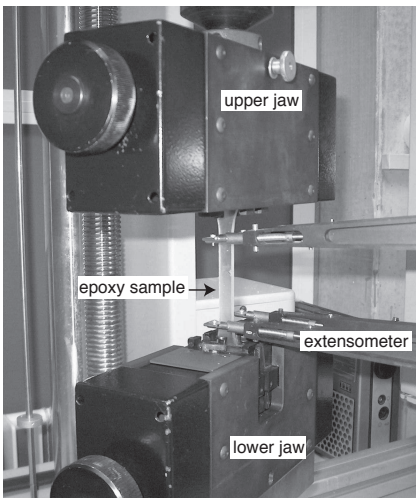

Figure 5.2: Epoxy dog-bone sample mounted in the tensile tester.

5.2.2 SMA composite properties

Effect of SMA wires on residual strain

The influence of the SMA wires on the residual strain in the epoxy matrix was evaluated by monitoring the evolution of the internal strain during curing and post-curing with an embedded fibre Bragg grating strain sensor [163]. Three types of sample were tested: (a) pure epoxy samples, (b) SMA wire/epoxy samples where the wires were fastened to an external frame for the duration of the cure and the post-cure and (c) SMA wire/epoxy samples where the wires were fastened to an external frame for the cure but unfastened for the post-cure. The epoxy bars had dimensions of $105 \times 10 \times 1\,\mathrm{mm}^3$; samples (b) and (c) had four embedded SMA wires—two on either side of the FBG—corresponding to a volume fraction of 0.7% (Fig. 5.3). To prepare the samples, the degreased SMA wires and the optical fibre were laid out parallel and evenly-spaced with the help of an alignment comb. A metallic mould of the sample dimensions was then placed around the wires, and the epoxy was then poured into it. The FBG was interrogated during the cure and post-cure periods, using a broadband optical source with a spectral range of 1,510-1,590 nm. The Bragg wavelength was monitored at 0.033 Hz by an optical detector. Both the interrogator and the detector were combined in a single Micron Optics sm125 Sensing Interrogator. The oven temperature was monitored with a K-type thermocouple. After testing, the reflected Bragg wavelengths were converted into a corresponding internal strain.

Single wire pull-out test

The SMA/epoxy interfacial strength was quantitatively characterised with a single wire pull-out test. Epoxy disc samples with a diameter of 10 mm, a height of 3-5 mm and an embedded SMA wire (Fig. 5.4) were made in silicone moulds. An SMA wire was passed through the centre of each mould using a needle. The SMA wires were

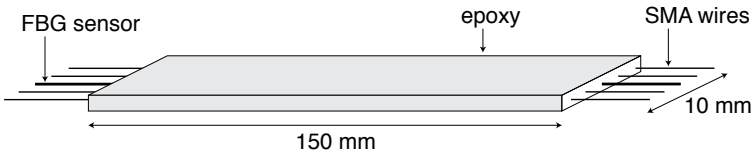

Figure 5.3: Schematic of the multi-SMA wire/epoxy composite sample with an embedded FBG sensor for monitoring internal strain evolution during processing.

then degreased using acetone and the moulds were filled with epoxy using a syringe. After curing and post-curing, the samples were de-moulded for testing. The SMA wire was slotted in a 160 μm-wide slit at the centre of a metal plate, which was clamped in the lower jaw of the tensile tester (Fig. 5.5). The free wire end was clamped in the upper jaw, which was then displaced at a rate of 1 mm/min. The force was recorded until the wire was completely pulled out of the matrix. The experimental interfacial shear strength (τ_{exp}) was determined from Eq. 2.4.

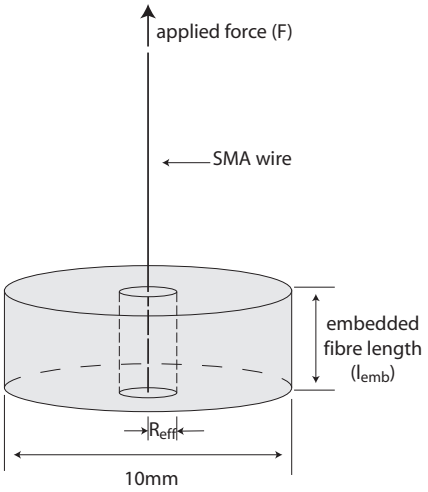

Figure 5.4: Schematic of the SMA wire pull-out sample.

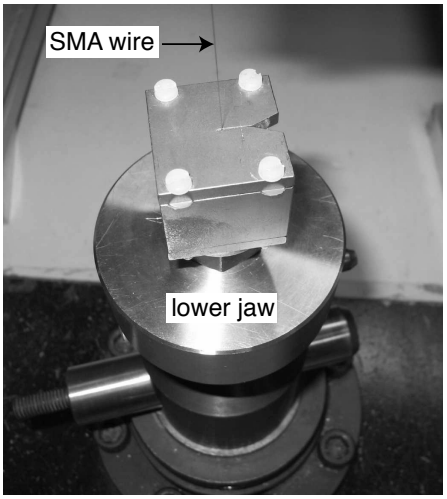

Figure 5.5: SMA wire pull-out sample in the lower jaw of the tensile tester.

Visual inspection of debonding

The interfacial strength was qualitatively characterised by progressively heating an epoxy sample containing six embedded, evenly-spaced SMA wires and observing for debonding. The samples were prepared in the same way as those in Fig. 5.3, but with six SMA wires (1.1% volume fraction) and without an optical fibre. These bars were then sectioned into 20 mm-long samples, with the SMA wires parallel to the length. A sample was placed on a Linkam TMS 600 programmable heater plate in a thermally-isolated sample holder, which was in turn placed under an Olympus macroscope, connected to a digital camera. The sample was heated at 10°C/min to 200°C, and photographs were taken at regular intervals.

Activation of multi-SMA wire samples

The interfacial bonding during cyclic activation of the embedded SMA wires was verified. The samples were prepared in the same way as the sample in Fig. 5.3, but with six SMA wires and without the optical fibre. The sample was clamped in the U-holder and then loaded in tension with 25 N to avoid buckling. The six wires were electrically-connected in series and then connected to a DC power supply. The heating cycle was repeated four times. The test procedure was identical to that of a single SMA wire, described in §3.2.3. However, a composite sample has a significantly higher rigidity than a single SMA wire, which implies that zero displacement of the U-holder when the sample is activated can no longer be assumed. The measured force is, therefore, corrected to account for this [95, 161]. The force the U-holder exerts in a non-equilibrium position is assumed to be fully recoverable, approximated by the force exerted by a spring with constant k, determined to be 540 N/mm [95]. Therefore, by definition, when an SMA wire/epoxy composite sample is placed in the U-holder and activated, the measured force is

$$\begin{aligned} F_{measured} &= F_u \\ &= kx \\ &= kl_0\epsilon_u \end{aligned} \tag{5.1}$$

where F_u is the force felt by the U-holder, x is the displacement from the equilibrium position, l_0 is the original distance between the two arms, ϵ_u is the strain of the U-holder, and compressive forces are taken as positive. The measured force is also the difference between the true activation force exerted by the sample (F_s; compressive) and the force that would be needed to restore its original length (F_r; tensile):

$$\begin{aligned} F_{measured} &= F_s - F_r \\ &= F_s - \sigma_c A_c \\ &= F_s - E_c\epsilon_c A_c \end{aligned} \tag{5.2}$$

where σ_c, ϵ_c, E_c and A_c are the stress, strain, Young's modulus and cross-sectional area of the sample, respectively. Equating Eqs. 5.1 and 5.2, and noting $\epsilon_u = \epsilon_c$,

$$\begin{aligned} F_s &= kl_0\epsilon_u + E_c\epsilon_c A_c \\ &= F_{measured}\left(1 + \frac{E_c A_c}{kl_0}\right) \end{aligned} \tag{5.3}$$

where the Young's modulus of the composite sample is given by the rule of mixtures:

$$E_s = V_f\, E_f + V_m\, E_m \tag{5.4}$$

where V_f and V_m are the volume fraction of fibres and matrix, respectively, and E_f and E_m are the Young's modulus of the fibres and matrix, respectively.

5.2.3 Liquid composite moulding

The suitability of the epoxy resin for liquid composite moulding was evaluated through torsional rheometry. The visco-elastic properties of the resin were determined as a function of cure time and temperature, using an Advanced Rheometric

Expansion System (ARES) from Rheometric Scientific Inc. The uncured epoxy mixture was placed between two parallel plates 25 mm in diameter and 0.3 mm apart, and subjected to a sinusoidal torsional deformation of 6.28 rads/s frequency and 20% strain. The evolution with time of the elastic shear modulus (G'), the viscous shear modulus (G''), their ratio ($\tan\delta = G''/G'$) and the viscosity (η) were measured. The test was repeated at different temperatures in the range 25-40°C, and then repeated on epoxy containing 5, 10 and 16 wt% Heloxy 61 modifier, a viscosity reducer.

The influence of adding the Heloxy 61 modifier on the deflection temperature of the epoxy was measured using a Rheometrics Solids Analyser, RSA II. Bars of cured epoxy of dimensions $5 \times 10 \times 50\,\text{mm}^3$, both without and with Heloxy 61 modifier, were prepared. The samples were then subject to dynamic three-point loading at a frequency of 1 Hz, and simultaneously heated from 25°C to 300°C at a rate of 10°C/min. The flexural elastic modulus (E') and the flexural visco-elastic modulus (E'') were measured over this range. The sample's deflection temperature was that at which its mechanical rigidity dropped.

5.3 Determination of epoxy post-cure schedule

5.3.1 Post-cure schedules

Table 5.1 summarises the four post-cure schedules evaluated in this chapter. These schedules are given the names PC_1–PC_4, where PC stands for *post-cure*. PC_1 is the standard schedule used in Chapter 4, while PC_2–PC_4 are introduced in this chapter.

Table 5.1: Description of the post-cure schedules.

Profile	1st stage		2nd stage		3rd stage	
	Temp [°C]	Time [hr]	Temp [°C]	Time [hr]	Temp [°C]	Time [hr]
PC_1	35	24	-	-	-	-
PC_2	45	24	-	-	-	-
PC_3	45	6	75	0.75	-	-
PC_4	45	6	75	0.75	95	0.2

5.3.2 Total heat of reaction

The total heat flow associated with the epoxy polymerisation reaction was determined from differential scanning calorimetry measurements on the uncured epoxy mixture, and found to be 358 J/g (Fig. 5.6).

5.3.3 Glass transition temperatures

The glass transition temperatures of the epoxy cured with each of the post-cure schedules were measured using 5–7 mg samples. The test was repeated three times for each sample type, and the data averaged. These are summarised in Table 5.2, and an example DSC curve is shown in Fig. 5.7. The goal was to achieve a glass

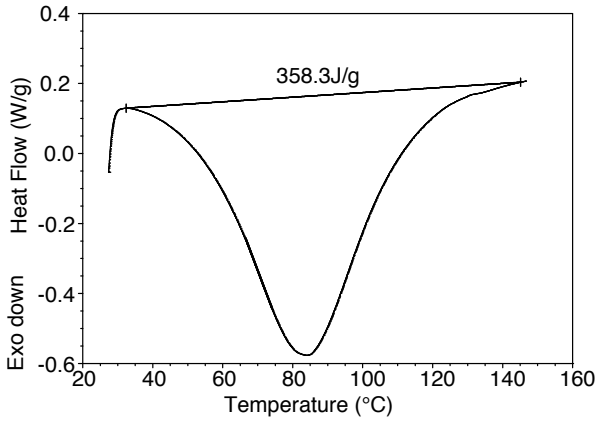

Figure 5.6: Differential scanning calorimetry curve for uncured epoxy mixture.

transition temperature 10°C higher than the 80°C activation temperature of the SMA wires. From Table. 5.2, PC_1 and PC_2 resulted in glass transition temperatures that did not meet this requirement. They were, however, substantially higher than their respective post-cure temperatures. This was most likely due to the highly exothermic nature of the reaction. PC_3 and PC_4, in contrast, both produced epoxies with sufficiently high glass transition temperatures.

Table 5.2: Glass transition temperatures of the epoxy cured at room temperature (PC_0) and post-cured using each of the four post-cure schedules (PC_1-PC_4).

Profile	Glass transition temperature [°C]
PC_0	48.2 ± 0.1
PC_1	63.0 ± 3.9
PC_2	68.6 ± 2.1
PC_3	94.9 ± 2.2
PC_4	109.1 ± 3.3

5.3.4 Tensile properties

Based on the results in §5.3.3, only the mechanical properties of epoxy samples prepared with PC_3 and PC_4 were evaluated. Four samples were prepared in each case. Before testing, each sample was verified for defects such as trapped air bubbles or chips, and faulty samples were discarded. For this reason, only two of the four PC_3 samples and three of the four PC_4 samples were tested. Their stress-strain curves are shown in Fig 5.8 a and Fig 5.8 b, respectively, and the averaged mechanical properties are summarised in Table 5.3. All samples exhibited brittle characteristics. Those fabricated using PC_3 had good mechanical properties. Post-curing the epoxy with PC_4 decreased both its tensile strength and its strain to failure by about 40%, and its Young's modulus by about 20%. These results suggest that the final stage at 95°C for 12 min of PC_4 induced some chemical degradation in the material.

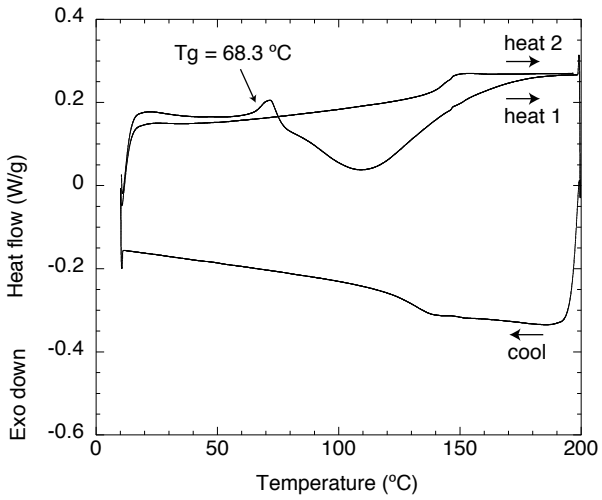

Figure 5.7: Differential scanning calorimetry curve for epoxy mixture cured at room temperature and post-cured with the PC_1 schedule. The glass transition temperature of this sample is 68.3°C.

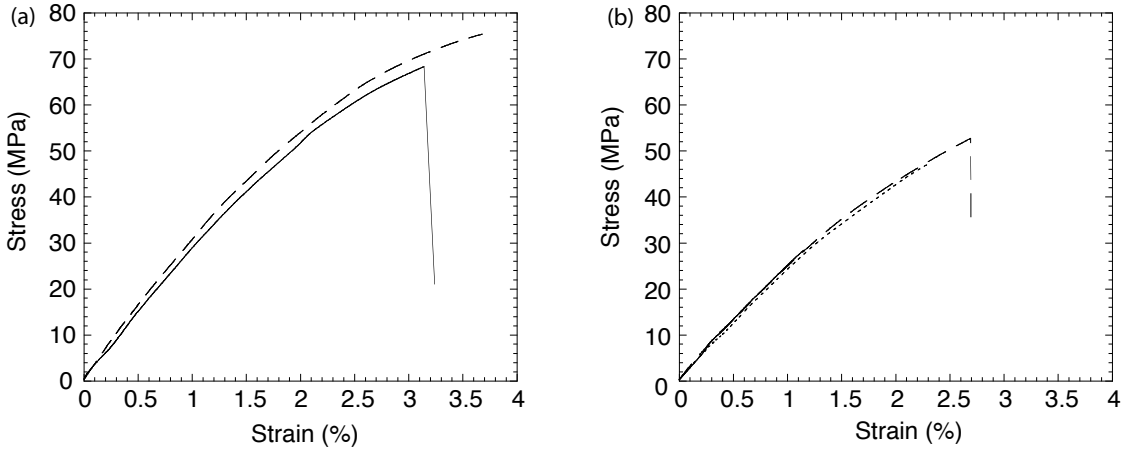

Figure 5.8: Stress-strain curves for the epoxy cured with (a) PC_3 and (b) PC_4.

Table 5.3: Tensile properties of the epoxy post-cured with PC_3 and PC_4.

Profile	Failure load [N]	Tensile strength [MPa]	Strain at failure [%]	Young's modulus [GPa]
PC_3	2.85 ± 0.21	71.9 ± 5.0	3.5 ± 0.3	2.81 ±0.09
PC_4	1.68 ± 0.49	42.8 ± 12.7	2.1 ± 0.8	2.29 ± 0.04

5.4 SMA composite behaviour

5.4.1 Effect of SMA wires on residual strain

The evolution of internal strain of the epoxy both without and with four embedded SMA wires during room-temperature curing and post-curing with PC_3 is shown in Fig. 5.9. At the end of the curing stage (Fig. 5.9a), the pure epoxy sample had a slight compressive strain of $50\,\mu\epsilon$. This was most probably due to the shrinkage of the sample upon gelation. The two samples with embedded SMA wires had a higher internal compressive strain of $150\mu\epsilon$ at the end of the cure stage. This was probably a result of the exothermic nature of the room-temperature curing—the reaction could have liberated sufficient heat to partially activate the wires during curing, causing them to contract and exert a compressive stress in the matrix.

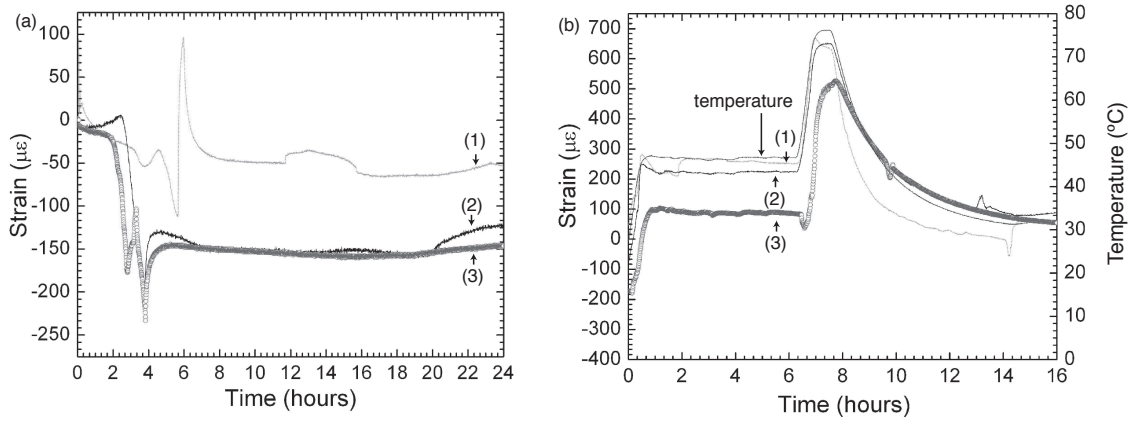

Figure 5.9: Evolution of internal strain of three samples that were (a) cured at room temperature and then (b) post-cured with schedule PC_3. The samples were a pure epoxy bar (1), an epoxy bar with four embedded SMA wires that were clamped in an external frame both during curing and post-curing (2) and an epoxy bar with four embedded SMA wires that were clamped in an external frame during curing and un-clamped during post-curing (3).

After curing, the SMA wires in one sample were released from the frame, which induced compressive stresses within it (Fig. 5.9 b, curve (3)). A strain of $300\,\mu\epsilon$ was then observed in the first hour for all samples, when the temperature was raised from 20°C to 45°C, and an additional strain of about $400\,\mu\epsilon$ was seen after about 7 hr, when the temperature was raised to 75°C. These two increases correspond to the expected expansion of the steel mould, assuming a thermal expansion coefficient of $12 \times 10^{-6}\,°C^{-1}$. When the samples were cooled to room temperature, the residual strain after post-curing tended to zero in all three samples. This volume fraction of SMA wires, therefore, did not noticeably influence the residual strain in the epoxy matrix.

5.4.2 SMA-epoxy interfacial strength

A first series of pull-out samples were prepared, with three samples per post-cure schedule, and tested. A representative result is shown in Fig. 5.10. The force increased until a displacement of about 6 mm and a load of 4 N, where the interface failed abruptly. After this point, the force was frictional, which gradually decreased and finally dropped to 0 N as the wire was pulled out of the matrix.

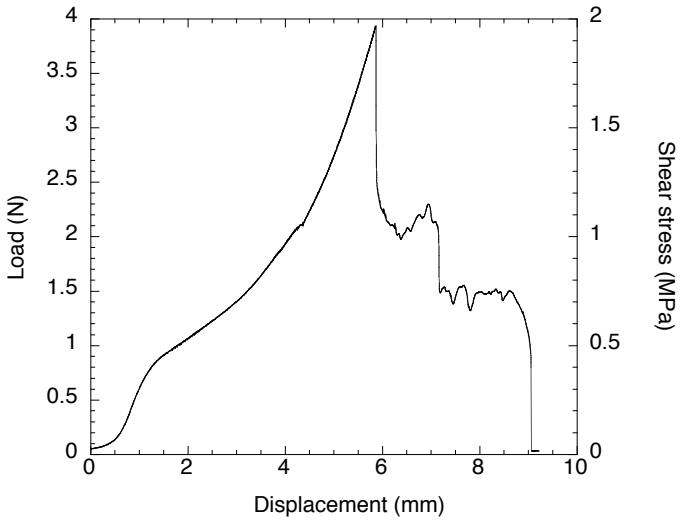

Figure 5.10: Representative result for a single SMA wire pull-out test. The strain rate was 1 mm/min and the embedded length of SMA wire was 4.3 mm.

The experimental interfacial shear strengths of the first series of samples were calculated using Eq. 2.4; the averaged values are summarised in Fig. 5.11. From Fig. 5.11, PC_3 and PC_4 produced the samples with the highest interfacial shear strength. A second series of pull-out samples were, therefore, prepared with these two schedules, and pull-out tests were once again carried out. Four samples were prepared in each case. The average embedded lengths for the second series of samples were 3.8 mm and 3.5 mm for the PC_3 and PC_4 samples, respectively, and the resulting τ_{exp} values were 3.6 $\pm$ 0.3 MPa and 2.8 $\pm$ 1 MPa, respectively. These values are higher than those in Fig. 5.11 due to the inverse dependence of τ_{exp} on the embedded length (Eq. 2.4); the average embedded lengths were longer in the first set of tests.

Equation 2.4 assumes an even distribution of shear stress over the full embedded length. However, the *actual* shear stress distribution is non-uniform, reaching a maximum at shallow depths in the samples, and then gradually decreasing with depth. The true maximum interfacial shear stress is, therefore, higher than the average value that is given by Eq. 2.4. Many groups have developed models for the pull-out of a single wire from a matrix to account for this. Both strength-based and energy-based approaches have been developed; each have their own set of assumptions. All start with the basic shear lag assumption by Cox [164]. One such model was developed by Mendels *et al.*, and is an analytical model that accounts for the geometry of the wire, the thermal stresses induced during curing and post-curing and the single-end loading configuration of the pull-out test. A full derivation is given in [165]–[167]. Their model assumes

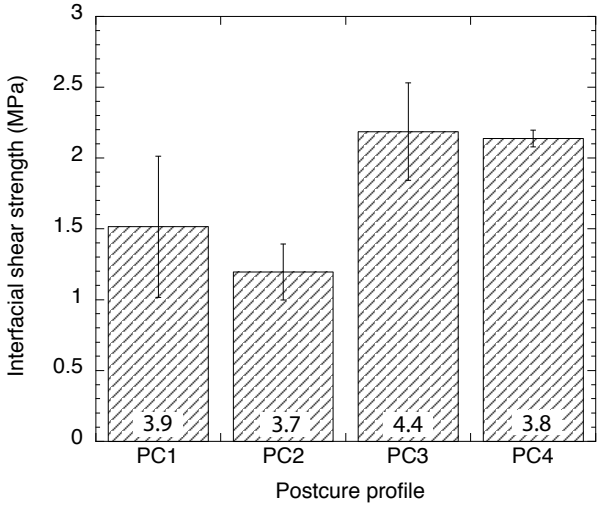

Figure 5.11: Summary of the SMA/epoxy interfacial shear strengths measured with the single wire pull-out test for the first series of samples, produced with each of the four post-cure cycles. The number at the base of each column is the average embedded length, in mm.

- the matrix and wires are linear elastic and isotropic,
- perfect bonding between the matrix and wires,
- the wires are perfect cylinders,
- the radial shrinkage is negligible relative to the axial shrinkage,
- failure occurs at the matrix/wire interface,
- constant stress through the radial section of the fibre, and integral stress transfer from matrix to fibre by shear at the interface,
- axial derivative of the axial stress in the matrix is graded in the radial direction by a function $1/r$, and
- martensitic orientation occurs only in the unembedded segment of the wire.

The resulting expression for the intrinsic interfacial shear stress is

$$\tau_i \;=\; \tau_{exp}\,\frac{\alpha l_{emb}}{\tanh\left(\alpha l_{emb}\right)} + K\tanh\left(\frac{\alpha l_{emb}}{2}\right) \tag{5.5}$$

where τ_{exp} is the experimental interfacial shear strength, given by Eq. 2.4, l_{emb} is the embedded SMA wire length, α accounts for the cylindrical geometry of the wire, given by

$$\alpha \;=\; \left[\kappa\frac{a^2E_f + \left(b^2-a^2\right)E_m}{aE_f\left(1+\nu_m\right)}\right]^{1/2} \tag{5.6}$$

where

$$\kappa = \frac{12\left[2(b-a)+\xi\left(b^2-a^2\right)\right]}{a\left[24a\left(b^2-a^2\right)-16\left(b^3-a^3\right)-3\xi\left(a^2-b^2\right)^2+6b(2+\xi b)\left[2b^2\ln(b/a)-\left(b^2-a^2\right)\right]\right]} \tag{5.7}$$

where

$$\xi = \frac{-E_m}{aE_f} \tag{5.8}$$

and K is the contribution due to internal thermo-elastic stresses, given by

$$K = \frac{a\alpha E_f(\alpha_m-\alpha_f)\Delta T}{2} \tag{5.9}$$

where α_m and α_f are the thermal expansion coefficients of the matrix and wire, respectively, and ΔT is the difference between room temperature and the peak post-curing temperature. The resulting interfacial shear stress distribution is illustrated schematically in Fig. 5.12 [166]. It can be seen that the contribution due to thermal stresses increases the maximum interfacial shear stress.

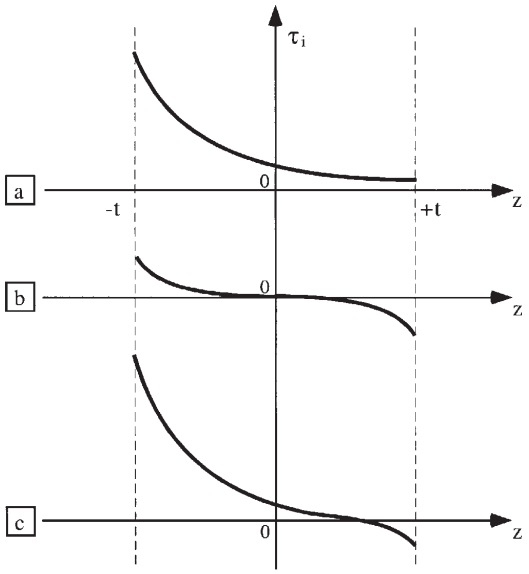

Figure 5.12: Interfacial shear stress distribution in the single wire pull-out test, given by the Mendels shear lag model. The z-direction is parallel to the wire's axis, where $2t$ is the embedded length, $-t$ and $+t$ are the two locations where the wire exits the matrix, and the load is applied on the side of $-t$. Shear stress due to: (a) single-end wire loading, (b) thermal stresses and (c) sum of (a) and (b) [166].

The intrinsic interfacial shear stresses for the SMA/epoxy samples fabricated with both PC_3 and PC_4 were calculated from Eq. 5.5, and are given in Table 5.4; each is the average of four tests. The material parameters used for these calculations are given in Table 5.5, and the constants are given in Table 5.6. The calculated interfacial shear strengths in Table 5.4 are high relative to the shear strength of the epoxy.

This is because the Mendels model assumes that failure occurs at the wire/matrix interface, and does not include a cohesive failure criterion, whereby failure occurs by shearing of the epoxy matrix. Nonetheless, the values in Table 5.4 indicate strong interfacial adhesion, and that the failure is likely to be cohesive. Similar observations were made in a previous study, where SMA wires were pulled out of an epoxy matrix, and observed under a scanning electron microscope [95]. Fragments of epoxy remained attached to the wire surface, indicating cohesive failure.

Table 5.4: Calculated intrinsic interfacial shear strengths for PC_3 and PC_4.

Profile	Intrinsic interfacial shear strength [MPa]
PC_3	77.2 ± 9.9
PC_4	51.8 ± 3.1

Table 5.5: Material parameters used in the pull-out model.

Matrix Young's modulus (PC_3)	$E_{m_{PC3}}$	[GPa]	2.81
Matrix Young's modulus (PC_4)	$E_{m_{PC4}}$	[GPa]	2.29
SMA wire Young's modulus	E_f	[GPa]	19
SMA wire radius	a	[mm]	0.075
Matrix Poisson ratio	ν_m		0.35
Matrix CTE	α_m	$[10^{-6}{}^{\circ}\mathrm{C}^{-1}]$	10
SMA wire CTE	α_f	$[10^{-6}{}^{\circ}\mathrm{C}^{-1}]$	60

Table 5.6: Calculated constants used in the pull-out model.

Profile	α [mm^{-1}]	κ [mm^{-3}]	b [mm]	ξ [mm^{-1}]	K [MPa]
PC3	5.06	60.6	0.507	-1.97	9.01
PC4	4.19	34.5	0.622	-1.61	10.5

5.4.3 Interfacial stress exerted by an activated SMA wire

The next stage was to determine if the interface was strong enough to remain intact once the SMA wires were fully activated. The requirement is that the interfacial shear strength (Table 5.4) should exceed the shear stress a wire generates at the interface by an activated wire. Baltá proposed a model to describe the stress generated in a prestrained, activated SMA wire embedded in an epoxy matrix [95]:

$$\begin{aligned}\sigma &= \sigma_p + \sigma_i \left(1 - \frac{\cosh(\alpha z)}{\cosh(\alpha t)}\right) \\ &\quad + \frac{2}{l_0}\left[\sigma_p t - \sigma_i \left(t - \frac{1}{\alpha}\tanh(\alpha t)\right)\frac{\cosh(\alpha z)}{\cosh(\alpha t)}\right] \\ &\quad + \sigma_{act}\left(1 - \frac{\cosh(\alpha z)}{\cosh(\alpha t)}\right)\end{aligned} \tag{5.10}$$

where σ_p, σ_i and σ_{act} are the stresses due to prestrain, thermal contraction and wire activation, respectively, z is the distance along the wire, t is the total length and α is 5.06 (Table 5.4). The initial prestrain of the wires was 0%, so $\sigma_p = 0$. Also, σ_i is related to the energy released into the composite when the wires are unfastened from the prestraining clamp. As the wires were not fastened during post-curing, this term is also zero. Thus, Eqn. 5.10 simplifies to

$$\sigma = \sigma_i \left(1 - \frac{\cosh(\alpha z)}{\cosh(\alpha t)}\right) + \sigma_{act} \left(1 - \frac{\cosh(\alpha z)}{\cosh(\alpha t)}\right) \tag{5.11}$$

Taking the first derivative with respect to z of Eq. 5.11 and equating it to the expression for the force equilibrium on a fibre element:

$$\frac{\partial \sigma}{\partial z} = \frac{-2\tau}{r_f} \tag{5.12}$$

gives

$$\tau = -r_f \frac{\alpha}{2} \frac{\sinh(\alpha z)}{\cosh(\alpha t)} (\sigma_i + \sigma_{act}) \tag{5.13}$$

For a sample post-cured with PC_3, $\sigma_i = E\alpha\Delta T = 2.81 \times (60 \times 10^{-6}) \times 50 = 8.4\,\text{MPa}$[1] and $\sigma_{act} = 300\,\text{MPa}$ (Fig. 3.10; $\sigma = F/A$). Figure 5.13 is the graphical representation of Eq. 5.13, using these values, for an embedded wire length of 2 mm[2]. The model predicts that the maximum interfacial shear stress is 58.3 MPa, exerted at the wire's extremities. Once again, however, Baltá's model does not include an interfacial failure criterion and, furthermore, assumes a perfectly linear elastic matrix. Equation 5.13 is, therefore, an overestimate of the interfacial shear stress. However, the Mendels and Baltá models can be comparatively interpreted, confirming that the maximum shear stress exerted by an activated SMA wire (58 MPa) remains below the intrinsic interfacial shear strength determined using the Mendels *et al.* model (77 MPa).

5.4.4 Visual examination of SMA/epoxy interface

Figure 5.14 shows two representative images of a sample with six embedded wires at (a) 25°C (not activated) and (b) 90°C (activated). At the start of the test (25°C) some debonding could be seen at the extremities of left-most SMA wire, which was induced when the samples were cut with the diamond saw. At 90°C, above the activation temperature of the SMA wires, the debonding of this wire extended further along the length of the interface, while the five other wires remained well-bonded. This test was repeated several times, yielding similar results. Only those wires that were already partially debonded showed further debonding as the temperature was increased. All wires were, however, fully debonded by 120°C.

[1] Where α was obtained from [168]

[2] The transfer length was calculated to be 1 mm

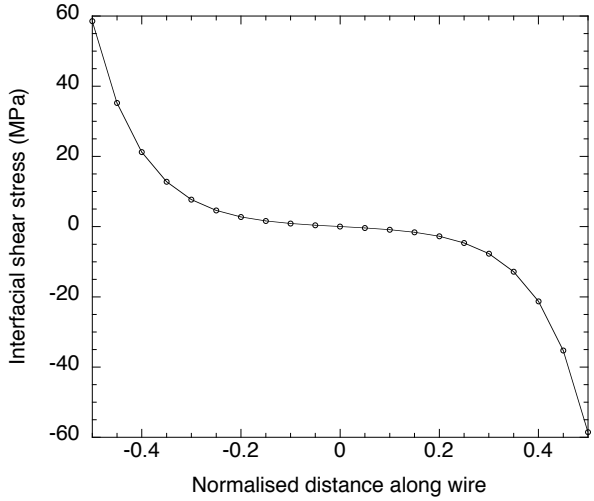

Figure 5.13: Modelled interfacial shear stress distribution for an SMA wire/epoxy sample processed with post-cure schedule PC_3, where the SMA wire is activated at 80°C.

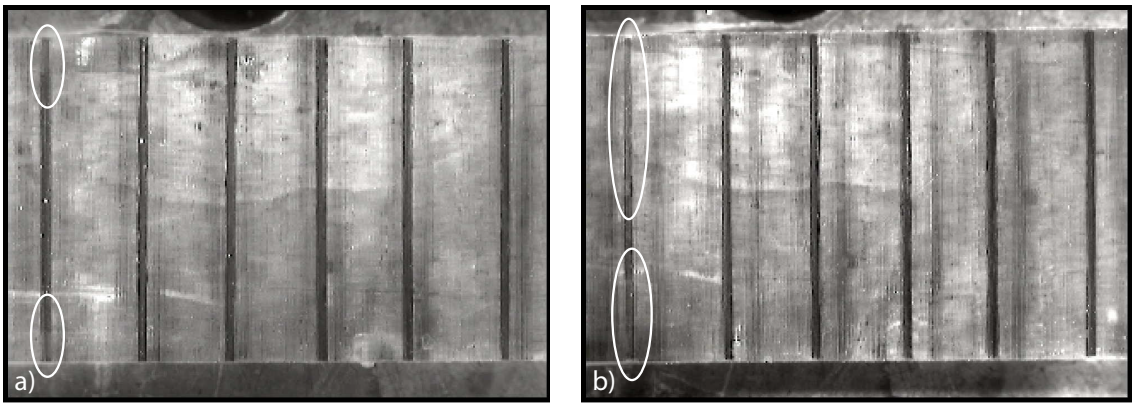

Figure 5.14: Images of a $1 \times 10 \times 20$ mm^3 epoxy sample with six embedded SMA wires at (a) 25°C and (b) 90°C. Although the resolution of the images is low, the left-most SMA wire is partially debonded at 25°C. This was induced by the cutting procedure with the diamond saw. At 90°C, the extent of debonding on this wire had increased, but the five other wires remain fully bonded to the matrix, indicating a good interfacial shear strength.

5.4.5 Cyclic activation of embedded SMA wires

To determine how the SMA composite behaves under cyclic SMA activation, a multi-SMA wire/epoxy sample was prepared and tested as described in §5.2.2. Figure 5.15 shows the recovery force generated over the four activation cycles. The compressive stress decreased between room temperature and 45°C due to the thermal expansion of the epoxy matrix coupled with the fact that that SMA wires were not activated in this temperature range. From Fig. 5.15, the thermal expansion coefficient of the matrix is $\alpha = \sigma/\mathrm{E}\Delta\mathrm{T} \sim 50 \times 10^{-6}\,^{\circ}\mathrm{C}^{-1}$, agreeing with values in the literature. Just above 40°C, which is the temperature above which the SMA wires start to exert a recovery force (Fig. 3.10), the gradient of the plot changed, due to activation of the SMA wires. The stress would have been expected to increase once again above this temperature, as the wires contracted. Instead, the curve flattened out. Most likely, the SMA wire volume fraction of this sample (1.1%) was too low to overcome the thermal expansion of the matrix; Baltá has previously found that a volume fraction of at least 2% is needed for the total recovery stress of the SMA wires to exceed the thermal expansion of the matrix [95]. However, the wires in the sample were visually inspected during and after activation, and remained well-bonded to the matrix throughout.

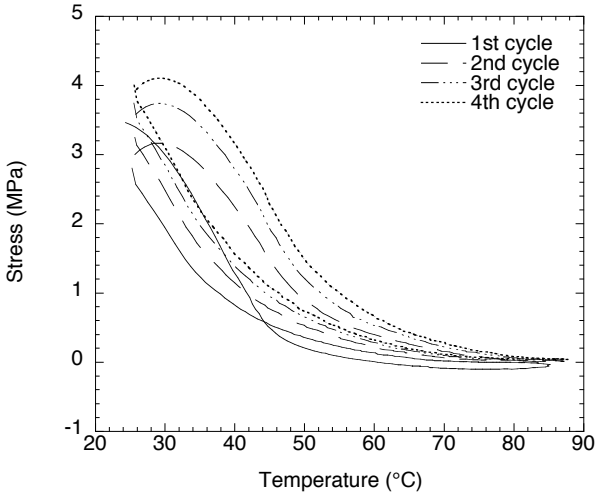

Figure 5.15: Stress induced in an epoxy bar of dimensions $1 \times 10 \times 150$ mm^3 with six embedded SMA wires over four SMA activation cycles.

5.5 Liquid composite moulding

5.5.1 Epoxy rheology

As a final stage of the study, the suitability of the epoxy system for resin transfer moulding was evaluated through viscosity measurements on the epoxy mixture. The evolution of the viscosity with time was measured at several different temperatures in the ARES torsional rheometer (Fig. 5.16), described in §5.2.3. To ensure good

impregnation of the reinforcing carbon fibres with the resin, a maximum viscosity of 0.5–1 Pa s is desirable. From Fig. 5.16b it is clear that the EPON 828/DETA system is not ideally-suited to resin transfer moulding, with the only acceptable processing temperatures in the range 35-37.5°C, and offering only a 10 min window before the viscosity becomes too high. The solution was to add Heloxy 61 modifier to the system (§5.5.2).

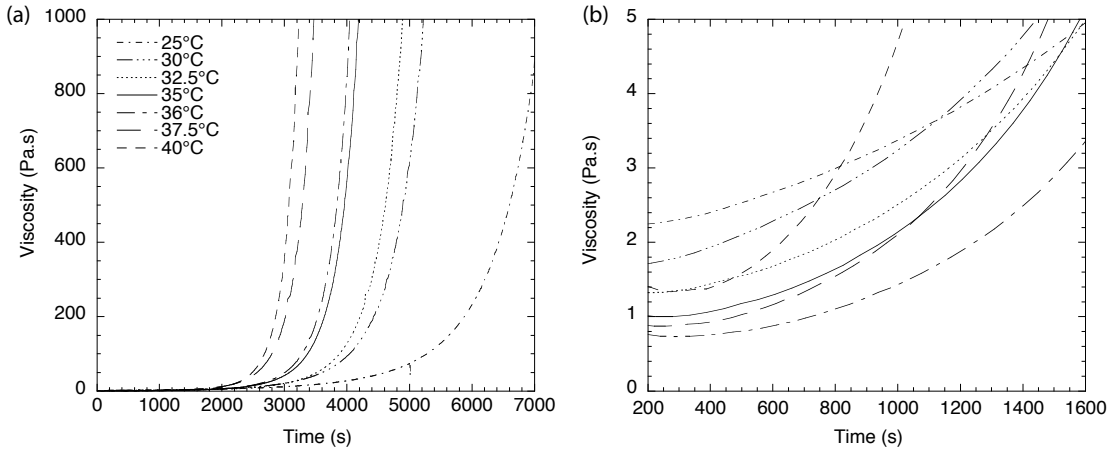

Figure 5.16: (a) Evolution of epoxy viscosity with time, at different temperatures. (b) Expanded region of the first minutes. The first 200 s are discarded as this was how long it took before the oven and sample were in thermal equilibrium.

5.5.2 Effect of Heloxy 61 modifier

Heloxy 61 is widely used to reduce the viscosity of epoxy resin formulations. Shell Chemicals, the manufacturer of EPON 828 epoxide, recommends a 16 wt% addition of Heloxy 61. However, torsional rheometer tests in the ARES on samples containing 5, 10 and 16 wt% Heloxy 61 revealed that 10 wt% was sufficient to reduce the viscosity to about 0.5 Ps s (Fig. 5.17).

The effect of adding Heloxy 61 on the glass transition temperature was determined using differential scanning calorimetry, as before. Figure. 5.18 shows that for an addition of 10 wt%, the glass transition temperature was reduced by 7°C to about 88°C. This, however, remained above the peak activation temperature of 80°C of the SMA wires.

The influence of Heloxy 61 on the epoxy's deflection temperature was determined by testing solid samples in three-point bend in the rheological solids analyser (RSA). A representative measurement is shown in Fig. 5.19, for a sample prepared with 10 wt% Heloxy. The elastic and visco-elastic moduli started to drop at about 100°C, and the deflection temperature was measured as 107.0°C, where the loss factor was the greatest. The deflection temperature for a sample with 0 wt% Heloxy 61 was 113°C. Adding 10 wt% Heloxy 61, therefore, decreased the deflection temperature by 6°C, consistent with the decrease in glass transition temperature measured by DSC.

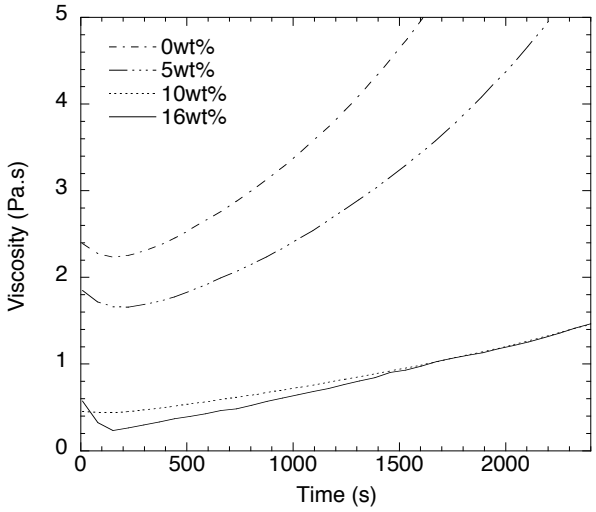

Figure 5.17: Evolution of epoxy viscosity with addition of 0, 5, 10 and 16 wt% Heloxy 61 modifier content in the epoxide, measured at 36°C.

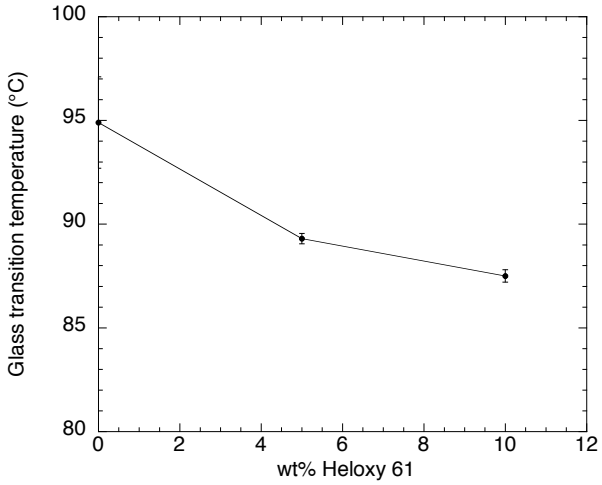

Figure 5.18: Variation of the glass transition temperature on addition of Heloxy 61 modifier.

Finally, the effect of Heloxy 61 on the mechanical properties of the epoxy was evaluated. Four dog-bone samples were prepared with 5 wt% Heloxy 61, and four with 10 wt%, all post-cured with the PC_3 schedule. These were tested in tension as before. Figure 5.20 shows the results. Within experimental variation, the Heloxy 61 did not have any significant effect on the tensile properties of the material.

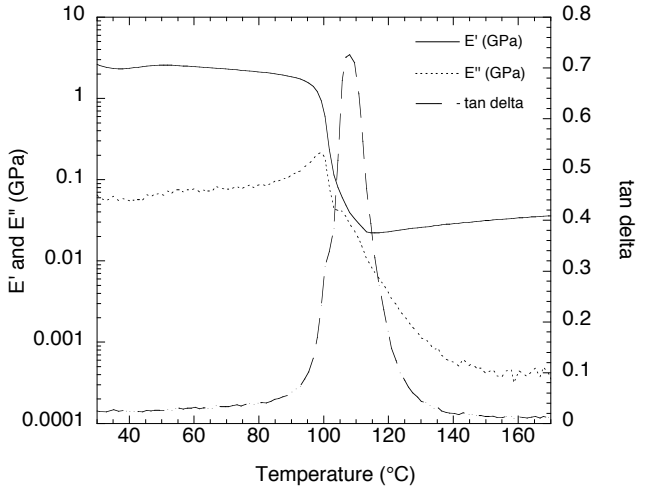

Figure 5.19: Rheological solids analysis plot for an epoxy sample containing 10 wt% Heloxy 61 in the epoxide. The sample was subject to dynamic three-point loading while heating. The elastic and visco-elastic moduli start to drop at about 100°C, and the deflection temperature is 107.0°C.

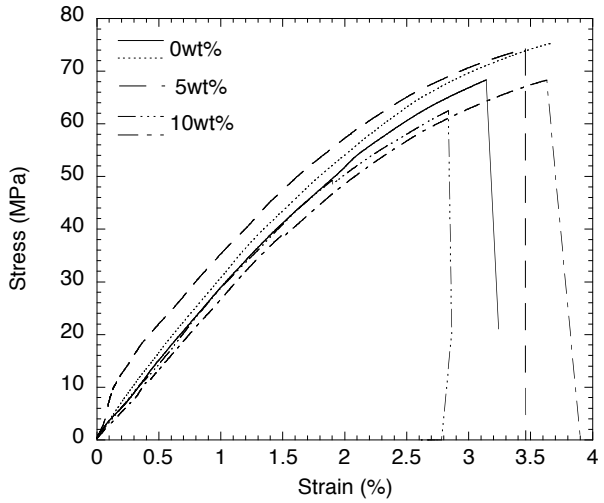

Figure 5.20: Stress-strain plots for epoxy dog-bone samples prepared with 0, 5 and 10 wt% Heloxy 61 viscosity modifier in the epoxide.

5.6 Discussion

A low-temperature liquid composite moulding cure schedule for composite samples with embedded shape memory alloy wires has successfully been developed. The selected process is a cure at room temperature for 24 hr followed by a two-stage post-cure with the first step at 45°C for 6 hr and the second at 75°C for 45 min. With this process, the SMA wires do not have to be maintained in place with an external frame—even though the maximum processing temperature exceeds their activation temperature—and remain well-bonded to the matrix during and after the process. The final composite has excellent thermal, mechanical and interfacial properties. The glass transition temperature of the pure epoxy matrix is 95°C, and 88°C upon addition of 10 wt% Heloxy 61 viscosity modifier. This, however, remains above the peak activation temperature of 80°C of the SMA wires. The tensile strength of the epoxy is 75 MPa.

The intrinsic SMA/epoxy interfacial shear strength was 77 MPa, determined using single-wire pull-out tests and an analytical model developed by Mendels *et al.* Bearing in mind the 75 MPa tensile strength of the epoxy, this calculated value of 77 MPa for the interfacial shear strength is high. This is because the Mendels model assumes that failure occurs at the interface between the wire and the matrix, and does not include a cohesive failure criterion, whereby failure occurs by shearing of the matrix. Nonetheless, the value does indicate a strong interface. The shear stress generated at the interface by an SMA wire activated at 80°C was then modelled, and determined to be a maximum of about 58 MPa, at the wire's extremities. Although this model overestimates the maximum interfacial shear stress, this value is comparatively lower than the intrinsic interfacial shear strength of 77 MPa. The SMA wire will, therefore, remain bonded to the matrix during activation. This was confirmed both through direct visual observation and through cyclic activation of a multi-SMA wire/epoxy sample made using the selected post-cure schedule. The wires in the sample were heated and cooled between room temperature and about 85°C four times, and remained bonded to the matrix throughout. Although the recovery stress they exerted was not sufficient to produce a net contractive stress on the sample, it was sufficient to counterbalance the thermal expansion of the epoxy matrix. Repeating this test with a higher volume fraction of SMA wires is expected to produce a net contractive stress [95]. The measurements in this chapter have successfully demonstrated that, through careful tailoring of the processing schedule, an SMA-epoxy composite can be manufactured without the need for any special infrastructure for, or treatment of, the SMA wires.

Chapter 6

Impact detection and localisation

6.1 Introduction

So far, the focus of this work has been on the repair components of the Active Sensing and Repair Composite, namely the microcapsule system for delivering the healing agent, and the shape memory alloy wires for compressing and heating the damage site during repair. In this chapter, the sensing component is considered.

There are two reasons why it is necessary to determine both the time of the damage event and its location in the material: 1) to activate the SMA wires as soon as the healing agent is released from the microcapsules, and to maintain the activation during the polymerisation period, and 2) to activate only those SMA wires that bridge the damaged region. The first item is to ensure crack closure occurs before the healing agent polymerises, and to ensure an optimised healing efficiency. The second item follows since each SMA wire draws considerable electrical power when activated (about 14 W per metre of wire at 0.5 A), and so it would be impractical to activate all SMA wires in the material simultaneously. Moreover, there may be other reasons, depending on the specific application, that preclude excessive heat dissipation throughout the material.

Impact detection and localisation are achieved in this work by incorporating a sparse array of strain sensors in the material. These sensors remotely detect the shock pulse propagating out from the impact site through the material. The time and location of the impact event are then determined from the relative time-of-flight measurements of three sensors.

Shock waves that propagate along a thin plate are guided elastic surface waves known as Lamb waves [169]. They are ultrasonic, with typical velocities in composite materials of 1,000–7,000 $\mathrm{m\,s^{-1}}$. Two main types of Lamb waves exist (Fig. 6.1): (a) extensional (symmetric, S) modes, with displacements that are symmetric about the mid-plane of the plate and (b) flexural (anti-symmetric, A) modes, with displacements that are anti-symmetric about the mid-plane of the plate. The waves are dispersive, i.e. their velocity is frequency-dependent. In principle the number of modes is infinite, although when the product of wave frequency times plate thickness is below 1 MHz mm, only the fundamental modes (S_0 and A_0) propagate [170].

To date, either surface-mounted or embedded piezo-ceramic transducers (PZTs) have been used to detect Lamb waves, since they are sensitive in the ultrasonic range and, moreover, to low-amplitude waves. However, optical fibre Bragg grating (FBG)

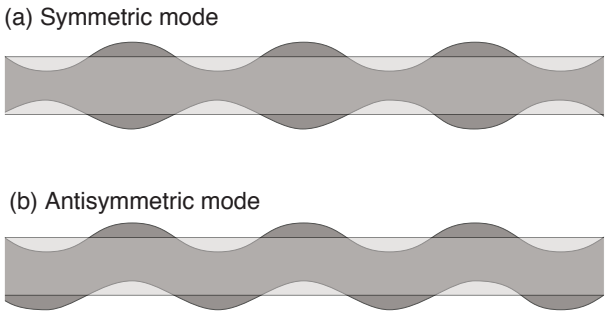

Figure 6.1: Oscillations of (a) symmetric and (b) anti-symmetric Lamb waves in thin plates. The undisplaced plates are represented by lighter shading.

sensors are an attractive solution for the present application, since they are easily embedded within the material, can be multiplexed and are immune to electromagnetic interference. Ultrasonic readout systems for FBG sensors are being developed by several groups, e. g. [145]–[149], towards applications in structural health monitoring. In this work, an FBG high-speed interrogation method based on work by Tsuda *et al.* [17, 18] is developed, permitting sensor interrogation at high sampling rates of 1–10 MHz. The technique is implemented here in a novel way, by creating a sparse array of surface-mounted, high-speed FBG sensors for impact localisation.

Localisation of the impact point is based on the arrival times of the Lamb waves at several sensors, which depend on the wave velocities. In an isotropic material the propagation velocity is independent of direction, and so the impact point can be located by classical triangulation [171]. However, for an orthotropic material such as a composite, the velocity varies with direction. As a consequence, several groups have developed localisation algorithms for orthotropic materials, e. g. [172]–[178].

In the work described in this chapter, impact events in isotropic aluminium plates are first localised using PZTs and classical triangulation [171]. This serves as a reference starting point because both the behaviour of Lamb waves in aluminium plates and the response of PZTs are well understood. The experimental and theoretical Lamb wave velocities for the aluminium plate are compared in order to confirm the experimental procedure. The complexity of the system is then increased by replacing the test plate with an orthotropic composite plate. An elegant, sequentially-iterative algorithm for locating impacts in orthotropic plates, based on minimising an error function [174], is written in Matlab and implemented. The velocity profiles for the S_0 and A_0 modes in the composite are experimentally-determined, and incorporated into the algorithm. Once again, to confirm the experimental understanding, the measured velocities in the composite material are compared to the theoretical values, which are calculated from classical plate theory, using a series of first-order approximations, and the known mechanical properties of the composite. Finally, once the algorithm has been verified and optimised, the PZTs are replaced with FBG sensors and further localisation tests performed.

The implemented algorithm has previously been evaluated with PZTs [174, 175] but, to the author's knowledge, not yet with FBGs. Moreover, although localisation of an impact using an FBG sensor array has recently been shown in an aluminium plate [179], the work reported here represents the first time it has been demon-

strated in a composite plate. Furthermore, in ref. [179] and other previous studies, ultrasonic pulses were used as a diagnostic tool to locate a damaged region and to determine its size; Lamb waves were launched from PZT generators, and the signal passing through a damaged region were compared with that passing through a healthy region, e. g. [17]–[152]. In contrast, the work presented here is—again to the author's knowledge—the first time the source of the wave is the impact event itself.

6.2 Theory

A brief description of the equations governing the propagation of symmetric and antisymmetric Lamb waves in thin plates is provided below.

6.2.1 Lamb wave propagation in isotropic plates

The theoretical dispersion curves of the lowest order extensional (S_0) and flexural (A_0) Lamb waves are obtained from classical plate theory, which uses first-order approximations to derive a set of equations describing the plate motion. Classical plate theory assumes that normals remain normal, straight and unstretched upon plate deformation. The approximations are valid in the range where the wavelength is large compared with the plate thickness; the typical cut-off is defined as a frequency-thickness product of 1 MHz mm. Details of the derivations can be found in [180] and [181].

S_0 mode

The expression for the velocity of the S_0 mode is determined from one of the equations of motion for the in-plane stresses, namely

$$\frac{E}{(1-\nu^2)}\left(\frac{\partial^2 u}{\partial x^2}+(1+\nu)\frac{\partial^2 v}{\partial x \partial y}+\left(\frac{1-\nu}{2}\right)\frac{\partial^2 u}{\partial y^2}\right)+\rho f_x \;=\; \rho\frac{\partial^2 u}{\partial t^2} \tag{6.1}$$

where E is the Young's modulus, ν is the Poisson ratio, u and v are the displacements in the x- and y-directions, respectively, f_x is a body force and ρ is the density. Now assume that f_x is zero, and that a sinusoidal plane wave is propagating along the x-axis with particle displacement in the x-direction. The displacements are

$$u \;=\; A_0 e^{i(\omega t - kx)} \tag{6.2}$$

$$v \;=\; 0 \tag{6.3}$$

where A_0 is its amplitude, ω is the angular frequency in radians/sec ($= 2\pi f$, where f is the liner frequency), k is the wavenumber ($= 2\pi/\lambda$) and $i = \sqrt{-1}$. Substituting Eqs. 6.2 and 6.3 into Eq. 6.1 gives the expression for the group velocity, c_e ($= \omega/k$), of the S_0 mode in an isotropic material:

$$c_e \;=\; \sqrt{\frac{E}{\rho(1-\nu^2)}} \tag{6.4}$$

Equation 6.4 predicts that, when the assumptions of classical plate theory apply, the S_0 mode travels at a constant velocity, independent of frequency.

A_0 mode

The expression describing the velocity of the A_0 mode is obtained from the equation of motion for a state of pure bending, where plane sections remain plane and perpendicular to the mid-plane of the plate. The relevant equation of motion is

$$D\nabla^4 w + \rho h \frac{\partial^2 w}{\partial t^2} = q \tag{6.5}$$

where h is the sample thickness, w is the displacement in the z-direction, q is the normal component of the body forces, ∇^4 is the biharmonic operator, given by

$$\nabla^4 = \frac{\partial^4}{\partial x^4} + 2\frac{\partial^4}{\partial x^2 \partial y^2} + \frac{\partial^4}{\partial y^4} \tag{6.6}$$

and D is the bending stiffness, given by

$$D = \frac{Eh^3}{12\left(1-\nu^2\right)} \tag{6.7}$$

Again assuming a sinusoidal displacement and zero body force, substituting into Eq. 6.5 gives the expression for the velocity of the A_0 mode in an isotropic material:

$$c_f = \sqrt[4]{\frac{D}{\rho h}}\sqrt{\omega} \tag{6.8}$$

The flexural mode is, therefore, dispersive, with a square root dependence on the frequency. As before, this equation is applicable only when the assumptions of classical plate theory apply.

6.2.2 Lamb wave propagation in orthotropic plates

In the case of an orthotropic material, classical plate theory is extended to include the orthotropic elastic properties predicted by laminate plate theory, giving rise to a new set of equations of motion. The dispersion relations for the extensional and the flexural modes are once again determined from these equations of motion. Full details of the derivation can be found in [181], [182] and [183].

S_0 mode

The equations of motion for a symmetric, orthotropic plate under pure tension are

$$A_{11}\frac{\partial^2 u_0}{\partial x^2} + A_{66}\frac{\partial^2 u_0}{\partial y^2} + (A_{12}+A_{66})\frac{\partial^2 v_0}{\partial x \partial y} = \rho h \frac{\partial^2 u_0}{\partial t^2} \tag{6.9}$$

$$A_{22}\frac{\partial^2 v_0}{\partial y^2} + A_{66}\frac{\partial^2 v_0}{\partial x^2} + (A_{12}+A_{66})\frac{\partial^2 u_0}{\partial x \partial y} = \rho h \frac{\partial^2 v_0}{\partial t^2} \tag{6.10}$$

where A_{ij} are the in-plane stiffnesses of the laminate, u_0 is the displacement in the x-direction, v_0 is the displacement in the y-direction and t is the time. Sinusoidal particle displacement is once again assumed:

$$u_0 = A_0 \alpha_x e^{i(\omega t - kx1_x - ky1_y)} \tag{6.11}$$

$$v_0 = A_0 \alpha_y e^{i(\omega t - kx1_x - ky1_y)} \tag{6.12}$$

where A_0 is the amplitude, α_i are particle direction cosines to account for the directional dependence of the propagation velocity, 1_i are the direction cosines between the propagation direction and the i-axis and ω is the angular frequency. Substituting Eqs. 6.11 and 6.12 into Eqs. 6.9 and 6.10, writing the resulting equations in matrix form, and finally setting the determinant equal to zero, gives two non-trivial solutions. The solution describing the S_0 mode velocity in the 0° direction, defined parallel to the axis of the reinforcing fibres, is

$$c_{e0} = \sqrt{\frac{A_{11}}{\rho h}} \tag{6.13}$$

where h is the sample thickness and ρ is its density. Similarly, for the 90° direction

$$c_{e90} = \sqrt{\frac{A_{22}}{\rho h}} \tag{6.14}$$

and finally for the 45° direction

$$c_{e45} = \sqrt{\frac{(A_{11} + 2A_{66} + A_{22}) + \sqrt{R}}{4\rho h}} \tag{6.15}$$

where

$$R = (A_{11} + 2A_{66} + A_{22})^2 - 4(A_{11} + A_{66})(A_{22} + A_{66}) + 4(A_{12} + A_{66})^2 \tag{6.16}$$

A_0 mode

The theory can be extended to include the A_0 mode. In this case an equation of motion for the bending of the plate is derived. When the laminate contains only 0° and 90° plies and when body forces are zero, this expression is

$$D_{11}\frac{\partial^4 w}{\partial x^4} + 2(D_{12} + 2D_{66})\frac{\partial^4 w}{\partial x^2 \partial y^2} + D_{22}\frac{\partial^4 w}{\partial y^4} + \rho h \frac{\partial^2 w}{\partial t^2} = 0 \tag{6.17}$$

where D_{ij} are the bending stiffnesses and w is the displacement in the z-direction. After substitution,

$$c_f = \sqrt[4]{\frac{(D_{11}{1_x}^4 + 2(D_{12} + D_{66}){1_x}^2{1_y}^2 + D_{22}{1_y}^4}{\rho h}}\sqrt{\omega} \tag{6.18}$$

For the 0° direction, $l_x = 1$ and $l_y = 0$, giving the expression for the flexural velocity in this direction as

$$c_{f0} = \sqrt[4]{\frac{D_{11}}{\rho h}}\sqrt{\omega} \tag{6.19}$$

Similarly, for the 90° direction ($l_x = 0$ and $l_y = 1$)

$$c_{f90} = \sqrt[4]{\frac{D_{22}}{\rho h}}\sqrt{\omega} \tag{6.20}$$

and the 45° direction ($l_x = l_y = 1/\sqrt{2}$)

$$c_{f45} = \frac{\sqrt[4]{D_{11} + 2(D_{12} + 2D_{66}) + D_{22}}}{4\rho h}\sqrt{\omega} \tag{6.21}$$

6.3 Experimental techniques

6.3.1 Localisation in aluminium plates with PZT sensors

Lamb wave velocity

Two Physical Acoustics Corporation (PAC) Nano-30 PZTs, each connected to a 40 dB 1220A PAC preamplifier, were mounted 100 mm apart on the surface of an aluminium plate of thickness 1.5 mm, using vacuum grease as a coupling agent (Fig. 6.2 a). Lamb waves were excited in the plate by snapping a 0.5 mm pencil lead[1] on its surface at the location shown in the figure. The propagating waves were detected by the PZTs and the electrical pulses were digitised at 10 MHz sampling rate using a Vallen AMSY5 high-speed AE (acoustic emission) system. The arrival times at the sensors of S_0 and A_0 mode waves of specific frequencies were determined using wavelet transform analysis, which decomposes the signals in the time-frequency domain.[2] The arrival time of a wave of a specific frequency was defined as the time at which the amplitude was maximum for that frequency. The velocities were then calculated from the times-of-flight.

Impact localisation

Three PZTs were mounted on the surface of the aluminium plate at the positions (100,100), (200,300) and (400,150), with the origin defined at the lower left corner of the plate (Fig. 6.2 b). Half-millimetre diameter pencil leads were then broken on the surface of the plate at known locations, namely (200,200), (300,100), (300,200) and (400,300). The Lamb waves detected by the three sensors were amplified, recorded using the Vallen system, and were then exported to Matlab for analysis using the algorithm for impact localisation in isotropic plates, detailed in Appendix A. The location of the impact points were first determined using the arrival times of the S_0 mode. In this work, the velocity of the S_0 mode is assumed to be constant, regardless of frequency, and the arrival time is defined as that of the leading edge of the signal, i. e. when the amplitude of the signal first exceeds the inherent noise level of the system. The location of the impacts were then determined using the arrival times of the A_0 mode at 250 kHz, given by the maximum amplitude on the wavelet transform plot.

6.3.2 Composite plate fabrication

Composite plates were fabricated by resin infusion. Carbon plies were laid up with a $[0°,90°]_s$ stacking sequence on a flat aluminium mould. A peel-ply layer and a mesh for resin distribution were laid on top of the carbon fibre bed. Two spiral feeds were placed on opposite sides of the fibre bed, parallel to its edges. One feed was the inlet for the resin, and the other was the outlet, connected to a vacuum pump. The layup was sealed in a vacuum bag, the resin inlet tube was closed, and a vacuum was drawn inside the bag. The resin was mixed with Heloxy 61 modifier

[1] ASTM standard E976-94

[2] The reader is referred to [174, 178] [184]-[188], for example, for a description of wavelet transform analysis.

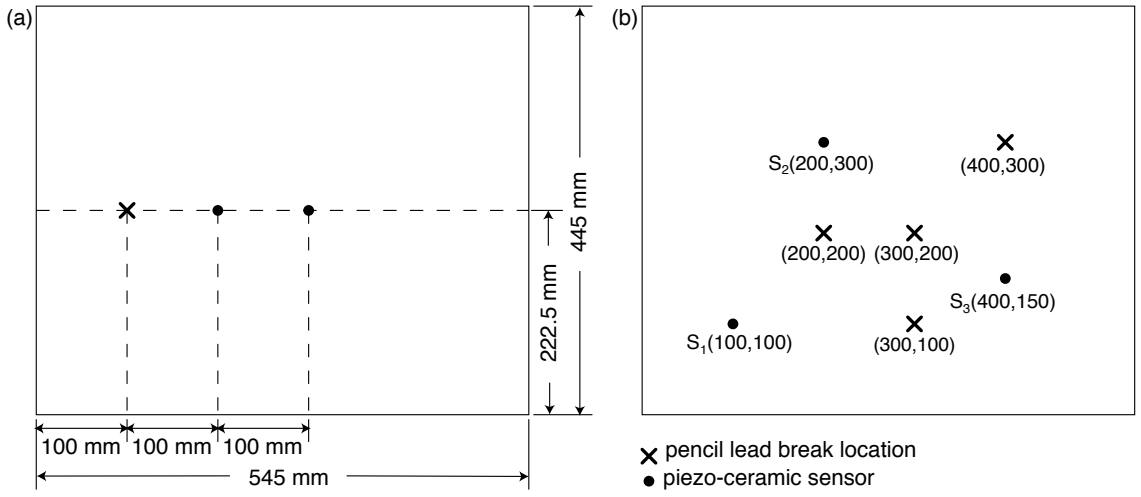

Figure 6.2: Positions of the lead breaks (crosses) and sensors (filled circles) on the aluminium plate to measure (a) the Lamb wave velocity, and (b) the location of impact events.

in a 9:1 weight ratio, which was then mixed with DETA hardener in a 100:12 weight ratio. The inlet tube was placed in the mixture, and the inlet valve was opened. The vacuum drew the resin from the pot into the vacuum bag, where it infused the carbon fibres. Once the resin front reached the far side, the inlet valve was closed, preventing any more epoxy resin from entering the vacuum bag. The vacuum was maintained for the duration of cure. Once cured, the sample was removed from the vacuum bag and post-cured at 45°C for 6 hr, followed by 75°C for 45 min.

6.3.3 Composite mechanical properties

Composite samples of dimensions $250 \times 25 \times 0.85$ mm^3, with a $[0°,90°]_s$ stacking sequence, were cut with the carbon fibres in the two outer plies parallel to the long dimension. Samples were prepared and tested in tension in accordance with the ASTM standards D 3039 and D 3518. Two HBM strain gauges, type 10/120LY41—one to measure longitudinal strain and the other transverse strain—were glued to the surface of each sample and connected in a half-bridge configuration. The gauges were calibrated before testing. The sample was then clamped in a tensile tester, and loaded in tension at a rate of 2 mm/min. Load-extension data were recorded. The longitudinal Young's modulus (E_{11}) was determined from the slope of the stress-strain plot. Due to the symmetry of the composite layup, the transverse modulus (E_{22}) was assumed to be the same as E_{11}. The major Poisson ratio (ν_{12}) is the ratio of the transverse strain to the longitudinal strain. The minor Poisson ratio (ν_{21}) was then $\nu_{12}E_{22}/E_{11}$. Five samples were tested and the data averaged. This test was repeated for composite samples cut with their plies at $[+45°,\text{-}45°]_s$. The slope of these stress-strain curves gave the shear modulus (E_{66}).

The experimentally-determined mechanical properties were then used in Eqs. 6.13–6.15 and Eqs. 6.19–6.21 to obtain the approximated theoretical velocities of the S_0 and A_0 modes, respectively. For Eqs. 6.13–6.15 the in-plane stiffnesses of the lami-

nate (A_{ij}) are

$$A_{ij} = \int_{-h/2}^{h/2} Q_{ij}^{(k)}\, dz = Q_{ij} h \tag{6.22}$$

where i = 1,2,6, k denotes the laminate layer and h is the sample thickness. For Eqs. 6.19–6.21 the bend stiffnesses (D_{ij}) are

$$D_{ij} = \int_{-h/2}^{h/2} Q_{ij}^{(k)} z^2\, dz = \frac{Q_{ij} h^3}{12} \tag{6.23}$$

In both cases, the elastic stiffness coefficients (Q_{ij}) are for a single unidirectional lamina in the laminate. In this work, however, the *average* stiffness coefficients ($\overline{Q}_{ij}$) are used, where

$$\overline{Q}_{11} = \frac{E_{11}}{(1 - \nu_{12}\nu_{21})} \tag{6.24}$$

$$\overline{Q}_{22} = \frac{E_{22}}{(1 - \nu_{12}\nu_{21})} \tag{6.25}$$

$$\overline{Q}_{12} = \frac{\nu_{12} E_{22}}{(1 - \nu_{12}\nu_{21})} = \frac{\nu_{21} E_{11}}{(1 - \nu_{12}\nu_{21})} \tag{6.26}$$

$$\overline{Q}_{66} = E_{66} \tag{6.27}$$

The reader is referred to [189] for further details.

6.3.4 Localisation in composite plates with PZT sensors

Lamb wave velocity

Two PZTs were mounted 100 mm apart on the surface of a $500 \times 500\,\mathrm{mm}^2$ composite plate, using vacuum grease as a coupling agent (Fig. 6.3 a). Lamb waves were excited and detected, and the S_0 and 250 kHz A_0 velocities were determined, all in the same way as for the aluminium plate (§6.3.1). Since the composite plate is orthotropic, the measurement was repeated for orientations from 0° to 90°, in 15° increments, where the 0° direction was parallel to the carbon fibres in the top lamina (Fig. 6.3 a).

Impact localisation

The same $500 \times 500\,\mathrm{mm}^2$ composite plate was used for the localisation tests with PZTs. Two sets of tests were performed. In the first set of tests, the sensors were placed at (100,100), (400,100) and (100,400), with the origin in the bottom left corner of the plate, and pencil lead breaks were performed at (150,300), (200,200), (300,140) and (400,350). In the second set of tests, the sensors were placed at (150,150), (350,150) and (150,350), and pencil lead breaks were performed at (200,200), (300,180), (240,230), (170,280) and (330, 250) (Fig. 6.3 b). The transient signals detected by the sensors were amplified, and recorded using the Vallen system. The signals were then exported to Matlab for analysis with the algorithm for impact localisation in orthotropic plates, detailed in Appendix B. The impact points were first located using the arrival times and velocity profile of the S_0 mode, and then using the 250 kHz component of the A_0 mode, in the same was as for the aluminium plate.

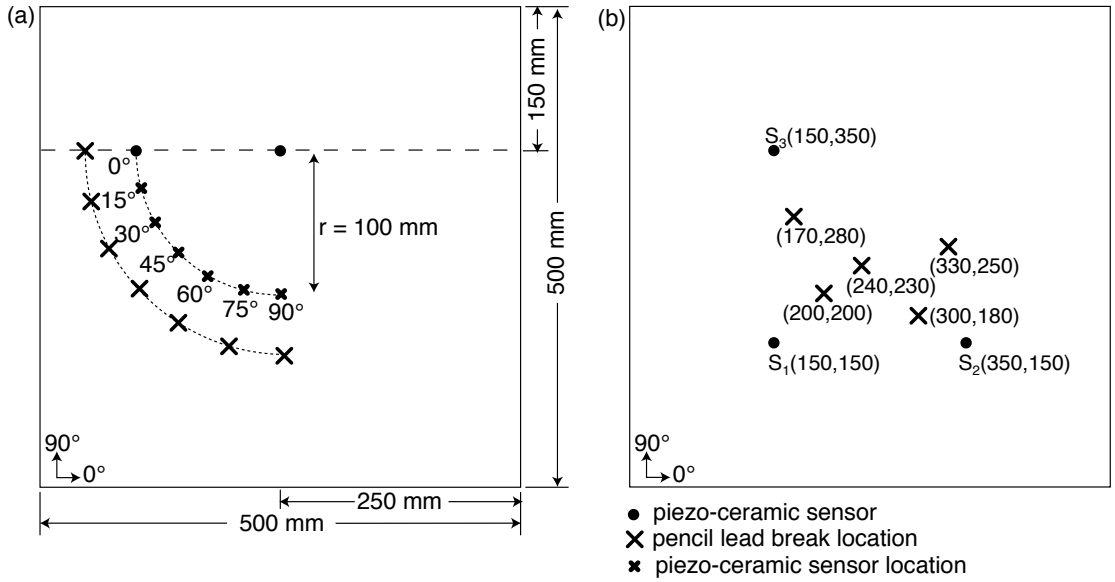

Figure 6.3: Positions of the lead breaks (large crosses) and sensors (filled circles and small crosses) on the composite plate to measure (a) the Lamb wave velocity at various angles relative to the carbon fibre orientation (diagram not to scale), and (b) the location of impact events.

6.3.5 Localisation in composite plates with FBG sensors

Setup

Impact localisation using FBGs was based on the FBG high-speed interrogation technique described in §2.3.3. Figure 6.4 shows a schematic diagram of the full setup, which involved three FBG sensor/filter pairs, each written at a different wavelength. The sensors were mounted on the surface of the composite plate and were illuminated by a 25 dBm Amonics broadband light source with 1528–1608 nm spectral range (Fig. 6.5). The three reflected narrowband signals were passed through the three FBG filters, whose Bragg wavelengths were set to the wavelengths at full-width half-maximum of each sensor. This tuning was achieved by mounting each filter on an individual micrometer stage. The transmitted light intensity was detected by three New Focus 125 MHz low-noise silicon photodetectors, sensitive in the 900–1700 nm range. The outputs of the photodetectors were sampled at 10 MHz by a National Instruments data acquisition card, controlled by a LabView program. The data were recorded to disk for offline analysis. Due to the short time span of impact events, a thermal-compensation FBG was not required.

The variation of reflected light intensity with strain of an FBG is given by

$$\frac{dR}{d\epsilon} = \frac{dR}{d\lambda} \cdot \frac{d\lambda}{d\epsilon} \tag{6.28}$$

where R is the reflected intensity, ϵ is the strain and λ is the wavelength [145]. The first term on the right side of the equation depends on grating length and strength. The second term depends on the optical fibre parameters; for the SMF 28 used in

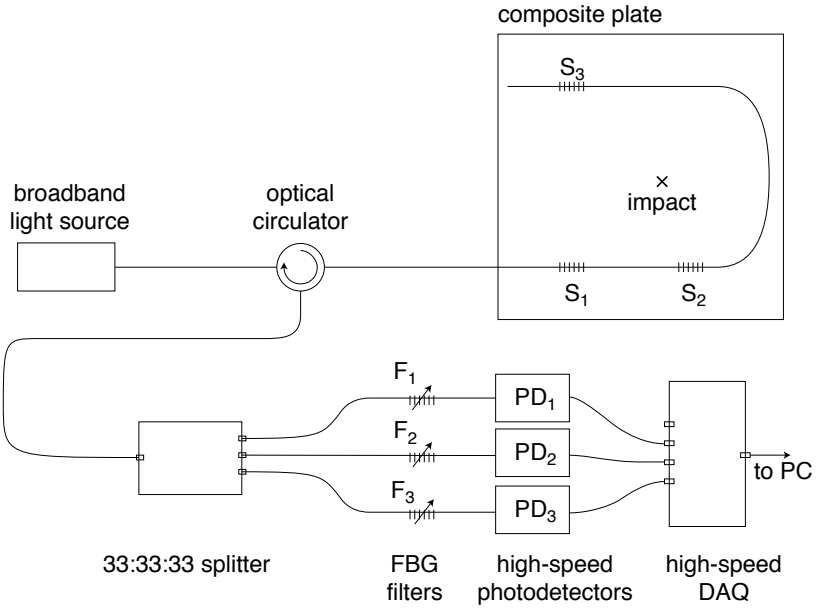

Figure 6.4: Schematic of the FBG high-speed interrogation system for locating impact events. The principle of operation is detailed in Fig. 2.35.

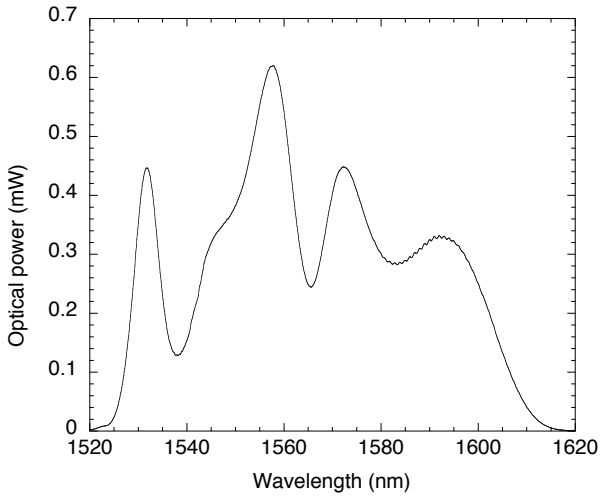

Figure 6.5: Emission spectrum of the 25 dBm Amonics broadband light source. The spectral range is 1528–1608 nm.

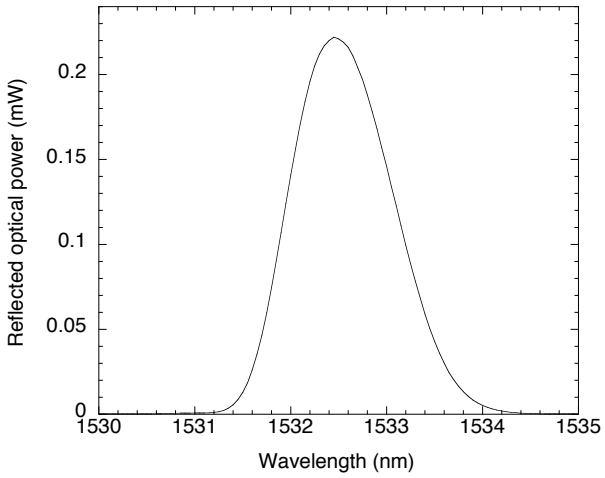

Figure 6.6: Reflection spectrum of the 50% reflectivity 1532 nm FBG sensor with 1 mm gauge length.

these tests, it is 1.2 pm/$\mu\epsilon$. Maximum strain range is achieved by minimising the first term, while maximum strain resolution is achieved by maximising it. FBGs with a reflectivity of 50% and a gauge length of 1 mm were, therefore, selected. The reasonably high reflectivity ensured sufficient light was reflected, increasing the sensitivity of the system, while the short gauge length increased the sensitivity to ultrasonic waves. When the wavelength of the propagating wave (λ) is much longer than the gauge length (L), the FBG is subject to a uniform strain field and a shift in the Bragg wavelength can be seen. However, when $\lambda \ll L$, the FBG is subject to a non-uniform strain field, with some areas of the sensor in tension while others are in compression. As a result the average strain almost cancels, and the Bragg wavelength barely shifts. Generally, $\lambda/L > 7$ ensures good sensitivity [146, 151]. So, for a propagation velocity of 5,000 m s^{-1}, a 1 mm FBG sensor should be sensitive to frequencies of up to about 700 kHz. The Bragg wavelengths of the three sensor/filter pairs were 1532 nm, 1547 nm and 1562 nm. Figure 6.6 shows a representative reflection spectrum of the FBGs used in this study.

An alternative setup for ultrasonic interrogation of FBG sensors uses a narrow-band tuneable laser instead of a broadband light source (Fig. 2.34) [18],[146]–[149], eliminating the need for FBG filters. This technique is also evaluated, and the results are compared to those obtained with the broadband source. The laser wavelength is set to the wavelength at full-width half-maximum of the sensor mounted on the composite plate, and any shift in the sensor's Bragg wavelength, therefore, modulates the detected optical intensity of the laser.

Velocity profile

The velocity profile in the composite plate was determined by mounting the 1532 nm (S_1), 1547 nm (S_2) and 1562 nm (S_3) FBG sensors at (150,150), (350,150) and (150,350), respectively, with their long axis parallel to the carbon fibres in the top ply, defined as 0° (Fig. 6.3 b). The plate was impacted using a small metallic hammer and the velocity was measured in the 0°, 45° and 90° directions. A metallic hammer

was used since it generated larger-amplitude signals than the pencil lead breaks; unless stated otherwise, this is the impactor used for all tests with FBGs. Sensors S_1 and S_2 were interrogated for the 0° direction, S_2 and S_3 for the 45° direction, and S_1 and S_3 for the 90° direction. The signals were recorded at a sampling rate of 10 MHz. The velocities were then determined from the arrival times of the leading edge of the signals.

Impact localisation

The setup to localise impact events with FBGs was identical to that described above to determine the velocity profile with FBGs. The same series of tests described in the *Localisation* section of §6.3.4 were carried out, but using a small metallic hammer as the impactor. The localisation results were compared to those obtained with PZTs.

6.4 Aluminium (isotropic) plate

6.4.1 Lamb wave velocities

The velocities of the S_0 and A_0 modes were experimentally-determined as described in §6.3.1. Representative signals for a single pencil lead break recorded by the two PZTs placed 100 mm apart are shown in Fig. 6.7, and the wavelet transform plots for these two signals are shown in Fig. 6.8.

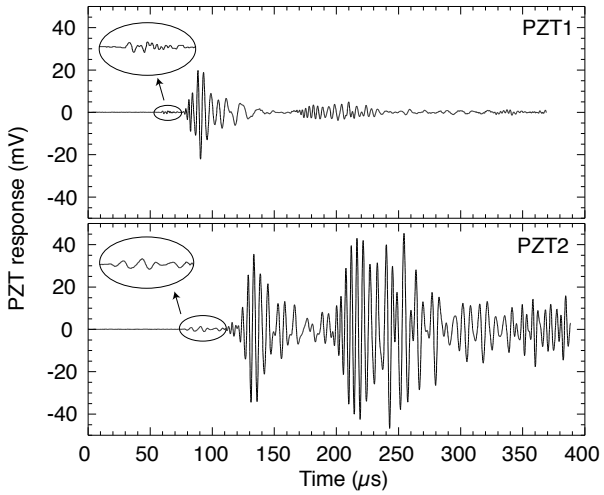

Figure 6.7: Representative single event measured in an aluminium plate. The two sensors, PZT_1 and PZT_2, are mounted 100 mm apart and respond to a 0.5 mm pencil lead break at the surface of the plate. The S_0 mode is the small-amplitude signal arriving at about 60 μs at PZT_1, and the A_0 mode is the larger-amplitude signal arriving at about 80 μs. Reflections from the plate boundaries are seen to arrive at PZT_1 after 170 μs. The corresponding pulses, at delayed times, can be seen at PZT_2.

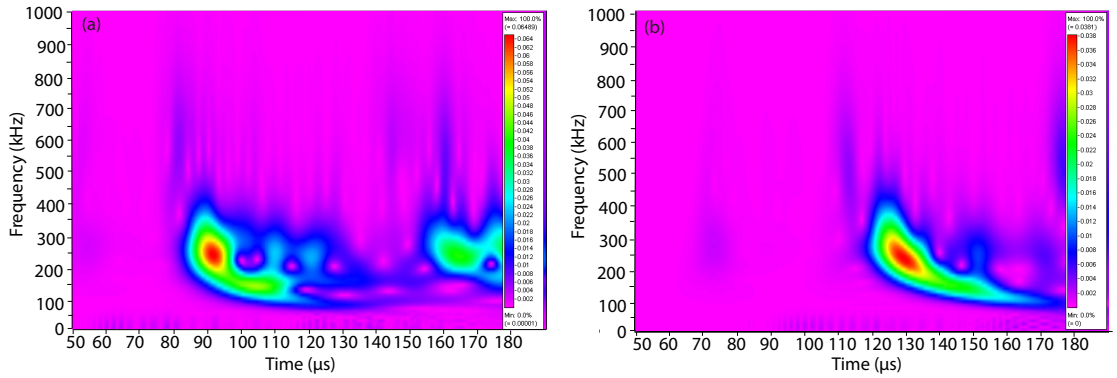

Figure 6.8: Time-frequency domain analysis of the pulses in Fig. 6.7. The colour scale represents the wavelet coefficient, where red is the highest and blue is the lowest. The S_0 mode (faint blue patch) arrives around 55 μs in (a) and 72 μs in (b); the A_0 mode begins at 80 μs in (a) and at 120 μs in (b).

The arrival times of restricted S_0 and A_0 frequency bands in the range 100–600 kHz were determined from the time-frequency data using bandpass filters, from which experimental velocities were determined. The results are shown in Fig. 6.9, together with the theoretical dispersion curves calculated from the physical properties of a 1.5 mm-thick aluminium plate (Table 6.1). The theoretical curves are first calculated according to the approximations of classical plate (CP) theory (Eqs. 6.4 and 6.8), and are then calculated with a computer program employing the Lamb wave equations (L) [169]. From Fig. 6.9, the Lamb waves equations, which give the exact solutions, accurately predict the velocities. However, the approximations of classical plate theory provide a reasonable estimation of the velocities.

Table 6.1: Physical properties of an aluminium plate of thickness 1.5 mm: tensile stiffness (E) Poisson ratio (ν) and density (ρ).

E [GPa]	ν	ρ [kg m^{-3}]
72	0.35	2700

6.4.2 Impact localisation

Lead breaks were carried out on the aluminium plate as described in §6.3.1 and the events were located using the algorithm for an isotropic plate (Appendix A). Figure 6.10 shows representative PZT signals, in this case for a lead break at (200,200).

The impact events were first located using the S_0 mode and then using the A_0 mode at 250 kHz. Experimentally-measured velocities of 5440 m s^{-1} and 2763 m s^{-1} were used in the algorithm, respectively (Fig. 6.9). Figure 6.11 summarises these localisation tests. All points were accurately located, with a standard deviation of 2.5 mm for the S_0 mode and 1.1 mm for the A_0 mode.

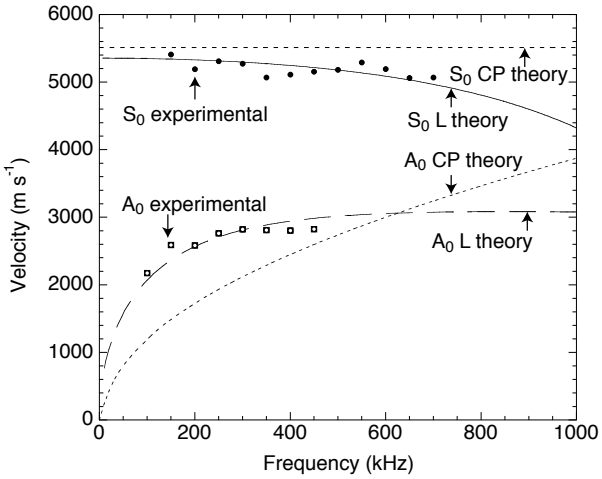

Figure 6.9: Comparison of the experimental and theoretical velocities of the S_0 and A_0 Lamb wave modes in an aluminium plate of 1.5 mm thickness, as a function of wave frequency. The theoretical curves are calculated according to classical plate (CP) theory and higher-order plate (L) theory. The experimental measurements (data points) are made with PZT sensors.

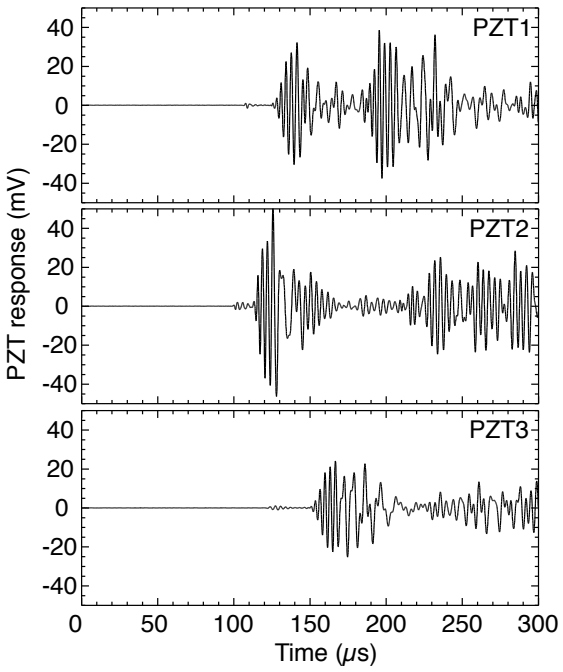

Figure 6.10: Representative single event measured in an aluminium plate using three PZT sensors, in response to a lead break at (200,200).

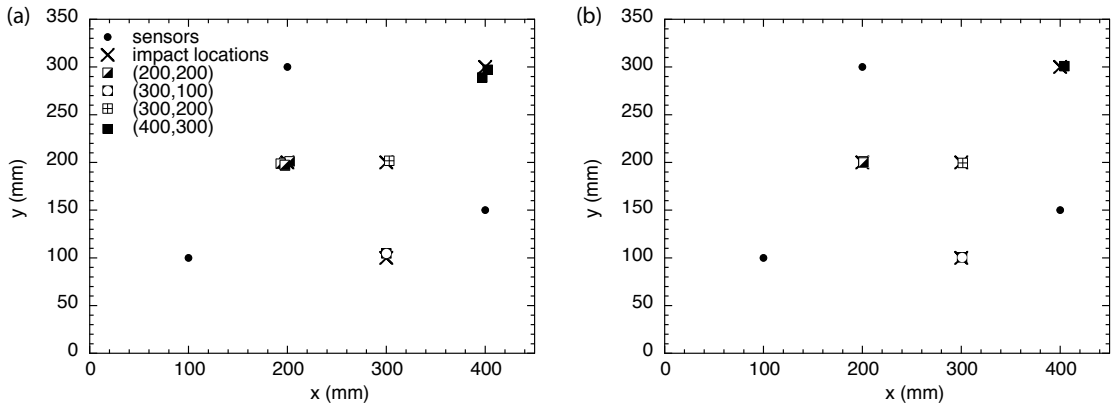

Figure 6.11: Summary of impact localisation tests on a 1.5 mm aluminium plate, based on the arrival times of (a) the S_0 mode and (b) the A_0 mode at 250 kHz at three PZTs (indicated by the filled circles). The impact points were all precisely located, with precisions for the S_0 and A_0 modes of 2.5 mm and 1.1 mm, respectively.

6.5 Composite (orthotropic) plate

6.5.1 Composite mechanical properties

The mechanical properties of the composite plate were determined as described in §6.3.3. Figures 6.12 and 6.13 show example measurements of stress versus strain for composite samples of $[0°,90°]_s$ and $[+45°,-45°]_s$ fibre orientations, respectively. Table 6.2 summarises the resulting experimentally-determined mechanical properties.

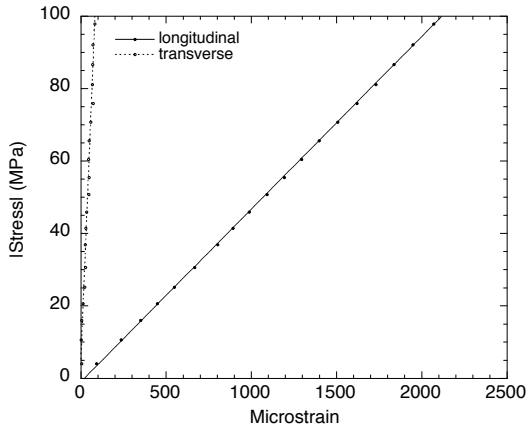

Figure 6.12: Longitudinal and transverse stress-strain curves, in the 0° direction of the composite, $[0°,90°]_s$ fibre orientation.

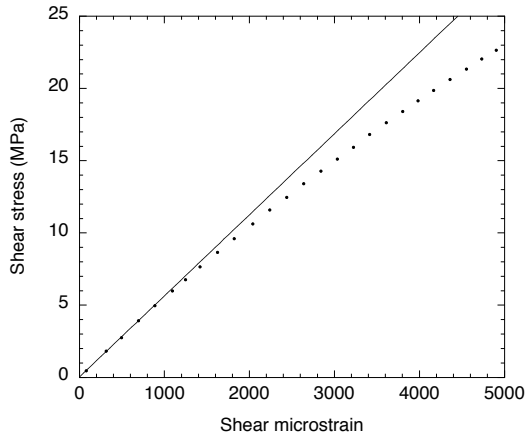

Figure 6.13: Shear stress-strain curve, in the 45° direction of the composite, $[+45°,-45°]_s$ fibre orientation.

Table 6.2: Experimentally-determined physical properties of the composite laminate with $[0°,90°]_s$ layup: tensile moduli (E_{ij}) Poisson ratios (ν_{ij}) and density (ρ).

E_{11}, E_{22} [GPa]	E_{66} [GPa]	ν_{12}, ν_{21}	ρ [kg m^{-3}]
47.7±0.3	5.55±0.4	0.028	1214

6.5.2 Lamb wave velocities

The velocities of the S_0 mode and the A_0 mode at 250 kHz were determined using two PZT sensors, as described in §6.3.4. Figure 6.14 is an example of the signals recorded by the two sensors aligned at an angle of 75° to the carbon fibre axis of the top lamina. Figures 6.15 and 6.16 show the measured angular dependence of the velocity for the S_0 mode and A_0 at 250 kHz mode, respectively.

The experimental and theoretical velocities of the S_0 and A_0 modes in the 0°, 45° and 90° directions are summarised in Table 6.3. The theoretical velocities were calculated using Eqs. 6.13–6.15 and Eqs. 6.19–6.21 for the S_0 and A_0 modes, respectively, and the mechanical properties in Table 6.2. In general the agreement is good, to within about one per cent. The larger discrepancies at 90° (transverse to the fibre axis) may have resulted from the effects of transverse shear deformation and rotary inertia, which are ignored in the classical plate theory. There could also have been contributions from the non-uniformity of the fibre tow spacing, which would alter the mechanical properties, and hence propagation velocity, transverse to the fibre axis.

Table 6.3: Comparison of experimental and theoretical velocities of the S_0 mode and the A_0 mode at 250 kHz at several angles in a 0.85 mm-thick composite plate.

Angle	S_0 velocity [m s^{-1}]		250 kHz A_0 velocity [m s^{-1}]	
	Experimental	Theoretical	Experimental	Theoretical
0°	6,630	6,270	1,646	1,555
45°	4,920	4,970	1,381	1,380
90°	5,992	6,270	1,360	1,555

6.5.3 Impact localisation with PZT sensors

A first series of lead breaks were performed on the surface of the composite plate at known locations, with the three PZTs at (100,100), (400,100) and (100,400). Figure 6.17 shows an example of the pulses detected by the sensors for an impact event at (300,140).

The events were first localised using the arrival times and the velocity profile of the S_0 mode (Fig. 6.15). The measured arrival times deviated on average by 1.9 μs from the expected arrival times, resulting in precise localisation of the impact point, to within about 7 mm. For example, the measured impact point for the event shown

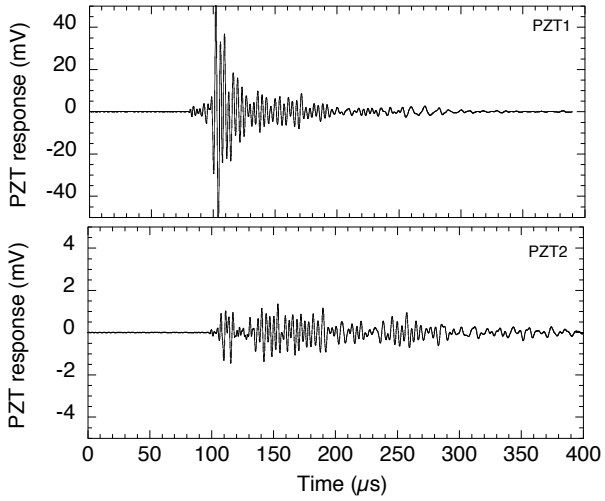

Figure 6.14: Representative single event measured in a 0.85 mm-thick composite plate using PZTs, in response to a pencil lead break located on the PZT_1-PZT_2 axis, and preceding PZT_1. The two PZTs are mounted 100 mm apart on the surface of the plate and are aligned at 75° to the fibre direction.

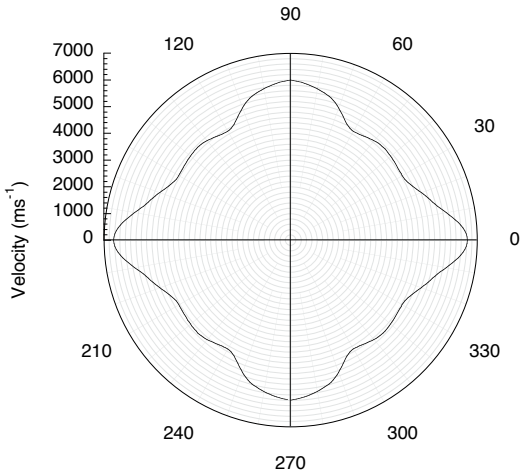

Figure 6.15: Angular dependence of the S_0 Lamb wave velocity in a 0.85 mm-thick composite panel, measured with PZT sensors. Zero degrees is the direction parallel to the carbon fibre axis in the top ply.

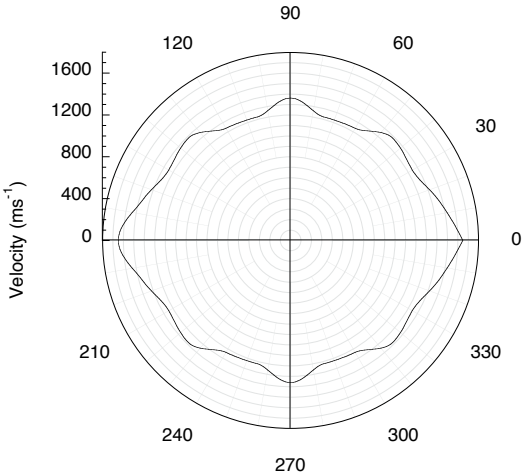

Figure 6.16: Angular dependence of the 250 kHz component of the A_0 Lamb wave velocity in the composite panel, measured with PZT sensors.

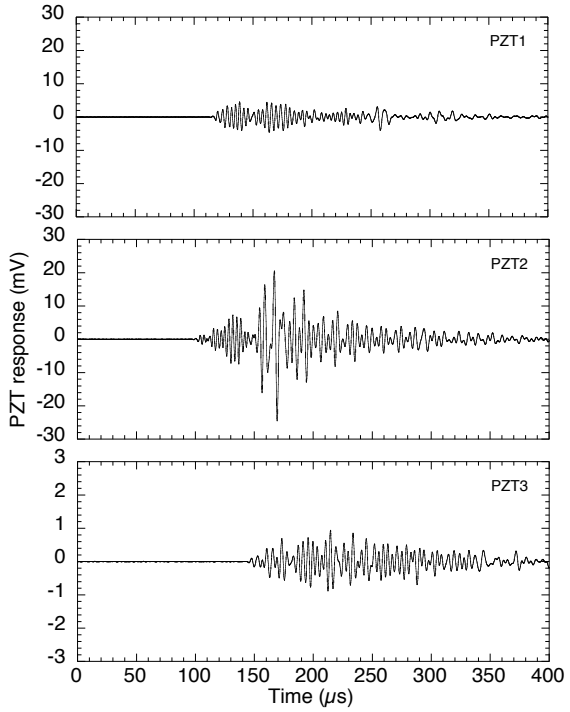

Figure 6.17: Representative single event measured in a 0.85 mm-thick composite plate using three PZT sensors located at (100,100), (400,100) and (100,400), respectively. The impact is located at (300,140).

in Fig. 6.17 was (298.2,143.8), in close agreement with the actual location (300,140). A compilation of all localisation measurements based on the S_0 mode is shown in Fig. 6.18.

The feasibility of locating these same events using the A_0 mode at 250 kHz was also evaluated. The arrival times were determined using wavelet transform analysis. The measured arrival times deviated on average by 54 μs from the expected arrival times, resulting in highly inaccurate localisation, often with several ten of millimetres error. This was found to result from the interference of waves reflected from the plate edges, making it difficult to determine the actual arrival time of the direct wave. A representative case is shown in Fig. 6.19, which is the wavelet transform of the PZT_3 signal in Fig. 6.17.

The solution was to move the PZT sensors further away from the plate edges to new positions at (150,150), (350,150) and (150,350), respectively. A second round of lead breaks were then performed. The recorded signals had similar characteristics to those shown in Fig. 6.17. As before, impact localisation was first determined using the arrival times of the S_0 mode. The results were similar to those of the first round measurements, with an average error in measured arrival time of 2.2 μs. Representative loci for a single measurement and a compilation of all measurements are shown in Figs. 6.20 and 6.21, respectively.

Localisation of the same set of events was then repeated using the A_0 mode at 250 kHz. With the sensors in the new positions it was possible in most cases to determine the arrival time of the direct wave, so the impacts could be precisely

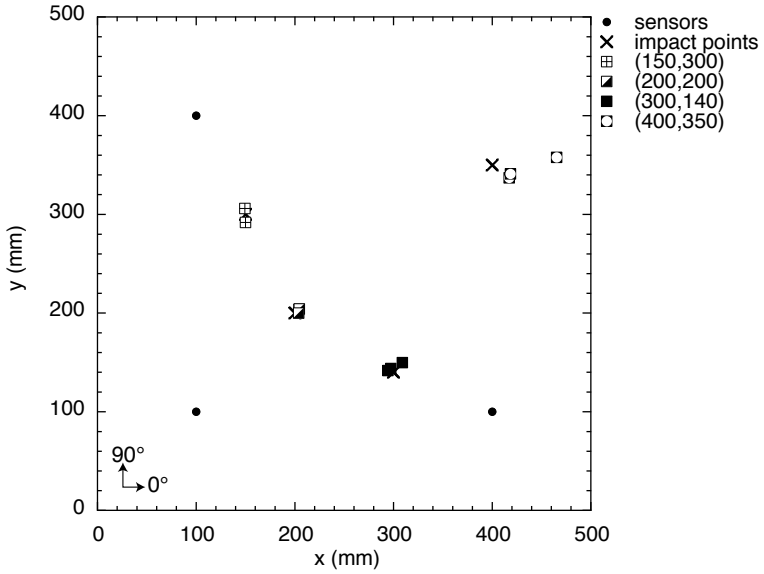

Figure 6.18: Compilation of the first round of impact localisation measurements in the 0.85 mm-thick composite plate, based on the arrival times of the S_0 mode at three PZT sensors (indicated by filled circles).

located. Representative loci and a compilation of all measurements are shown in Figs. 6.22 and 6.23, respectively. The large measurement spread for the impacts at (330,250) suggests that edge reflections still remain a problem for this location. If the three events at (330,250) are excluded, the average error in measured arrival time of all points is 2.9 μs (equivalent to about 4 mm).

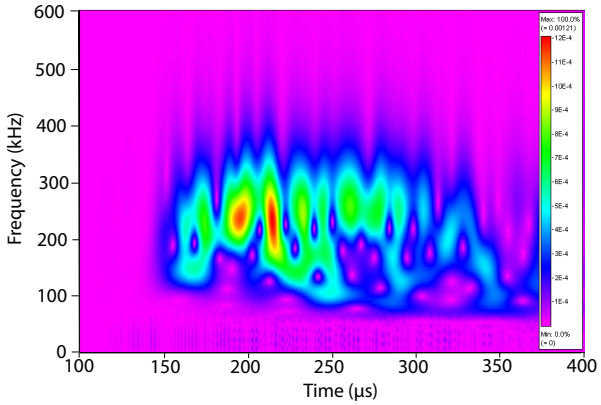

Figure 6.19: Time-frequency representation of the signal in Fig. 6.17, recorded by PZT_3. Multiple reflections interfere with the original pulse, which make it difficult to isolate the direct A_0 wave and precisely determine its arrival time.

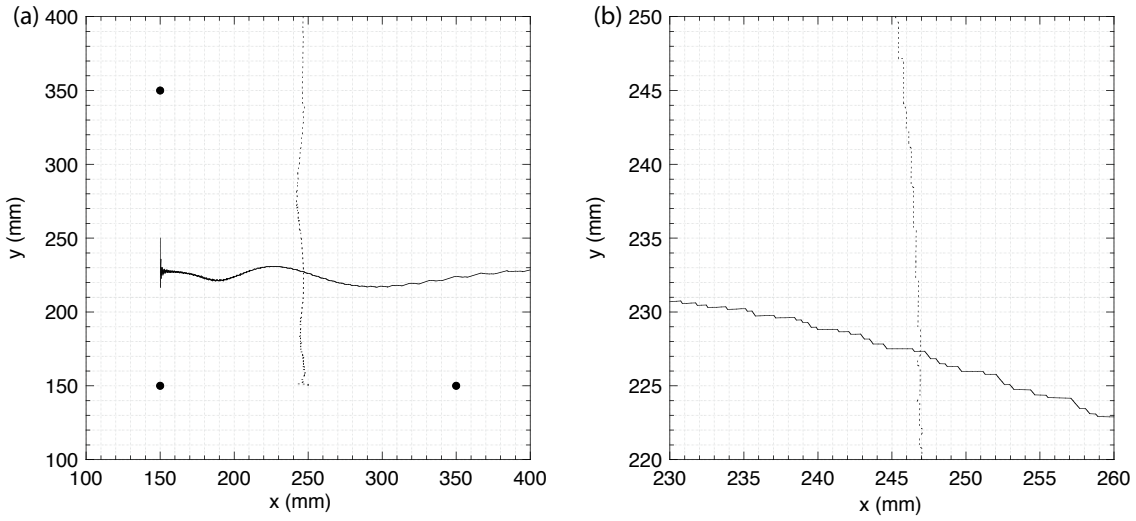

Figure 6.20: Experimentally-determined loci from pairs of PZT sensors on the 0.85 mm-thick composite plate, based on the arrival times of the S_0 mode: (a) large field of view, and (b) expanded region near the impact point, (240,230).

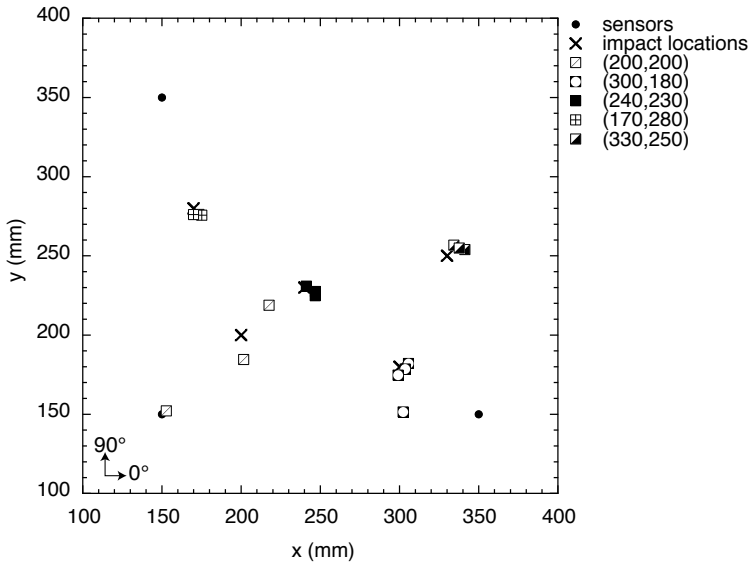

Figure 6.21: Compilation of the second round of impact localisation measurements in the 0.85 mm-thick composite plate, based on the arrival times of the S_0 mode at three PZT sensors (indicated by filled circles).

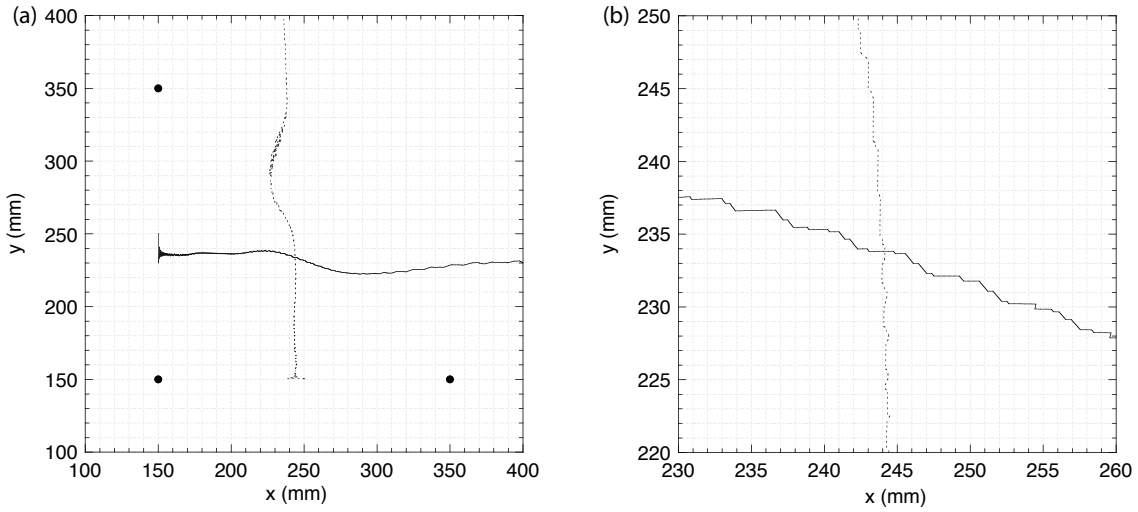

Figure 6.22: Experimentally-determined loci from pairs of PZT sensors on the 0.85 mm-thick composite plate, based on the arrival times of the A_0 mode at 250 kHz: (a) large field of view, and (b) expanded region near the impact point, (240,230).

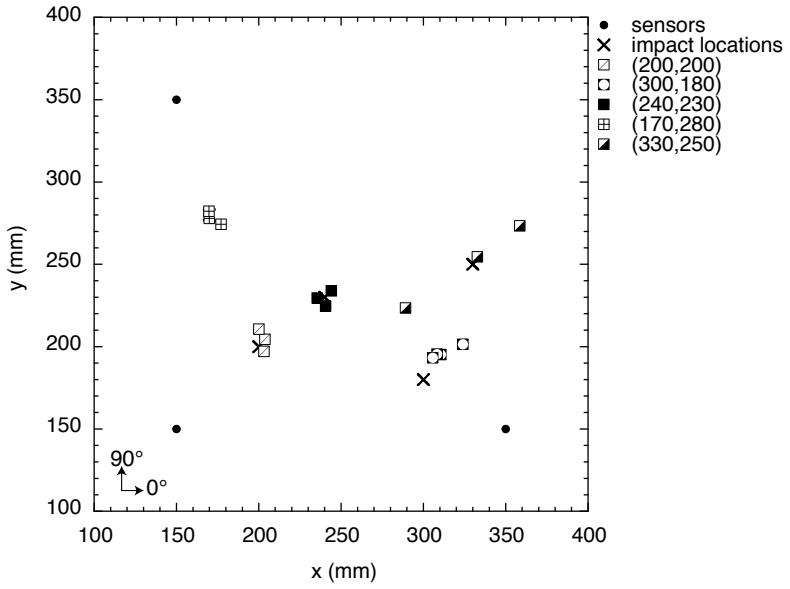

Figure 6.23: Compilation of the second round of impact localisation measurements in the 0.85 mm-thick composite plate, based on the arrival time of the A_0 mode at 250 kHz at three PZT sensors (indicated by filled circles).

6.5.4 Impact localisation with FBG sensors

Broadband light source

After having established a good understanding of the Lamb wave propagation characteristics and impact localisation in composite plates with PZT sensors, the attention is now turned to impact localisation with FBG sensors.

A direct comparison of PZT and FBG sensors was made prior to performing localisation tests with FBGs. A PZT sensor was mounted on the surface of the composite plate, adjacent to a 1532 nm FBG sensor illuminated with the broadband light source. The sample was impacted with a small metallic hammer 200 mm away from the two sensors and at an angle of 0° to the FBG's axis. Figure 6.24 shows the response of the sensors to the resultant shock wave. A 100 kHz lowpass filter, which removed high-frequency background noise on the FBG channel without affecting the main signal, was applied to both signals. The strain pulses measured by the two sensors are seen qualitatively to agree well. However the higher-frequency wave packet that arrived first is only visible in the PZT signal, and cannot be distinguished above the noise in the FBG signal. Comparing the amplitudes of the low- and high-frequency components in Fig. 6.24, the FBG sensor is about a factor 3 less sensitive. In consequence, the FBG sensor did not detect the small-amplitude oscillations seen by the PZT sensor at the start of the pulse train around 350 μs.

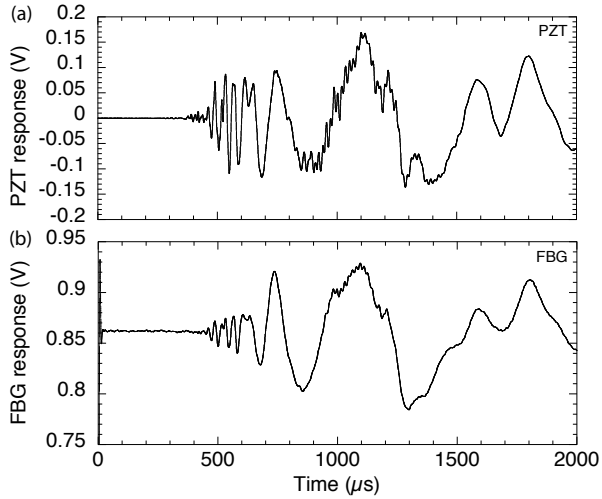

Figure 6.24: Example of signals detected simultaneously by (a) a PZT sensor and (b) an FBG sensor (illuminated with a broadband light source) mounted side-by-side on a 0.85 mm-thick composite plate. The impact was produced with a small metallic hammer at a distance of 200 mm and at an angle of 0° relative to the FBG axis. A 100 kHz lowpass filter was applied to both signals to suppress high-frequency noise on the FBG channel. There is an good correspondence of the strain pulses measured by the two sensors, although the first arriving higher frequency wave packet is not distinguishable above the noise in the case of the FBG sensor.

The sensitivity of the FBG sensor decreased as the angle between the FBG fibre axis and the impact direction was increased from 0° to 90°. This angular

dependence of the sensitivity was expected since a wave propagating parallel to the fibre axis causes a greater change in grating spacing than a wave of the same amplitude propagating perpendicular to the axis. These observations imply that the present FBG sensors, illuminated by a broadband light source, are not sufficiently sensitive to localise impacts from the small-amplitude S_0 mode waves.

The angular dependence of the wave velocity in a 0.85 mm-thick composite panel measured with FBG sensors illuminated with a broadband light source is shown in Fig. 6.25. A 100 kHz lowpass filter was applied to the signals. From the above discussion, these data are expected to correspond to low-frequency A_0 mode waves. Comparison with Figs. 6.15 and 6.16 confirms that the measured velocities are indeed characteristic of the slower A_0 mode. This was further confirmed with a time-frequency analysis of the signals, which showed predominant components in the range 20–40 kHz. However, this velocity profile is not a pure velocity profile for the A_0 mode, but rather an effective profile, which also accounts for the marked directional sensitivity of the FBG sensors.

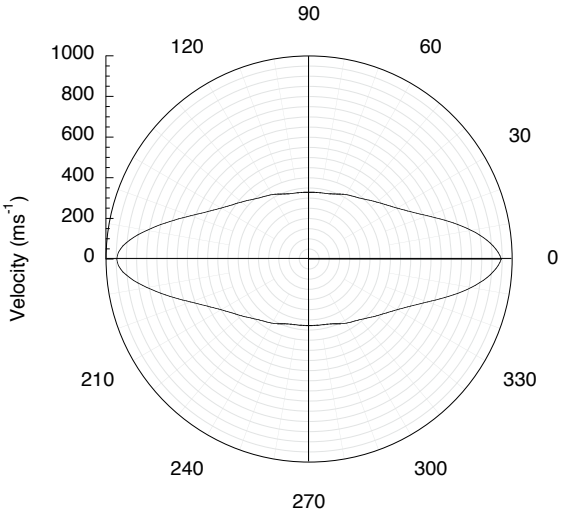

Figure 6.25: Angular dependence of the effective Lamb wave velocity in a 0.85 mm-thick composite panel measured with FBG sensors illuminated with a broadband light source. A 100 kHz lowpass filter is applied to the signals. Zero degrees corresponds to the direction parallel to the FBG axis and also to the carbon fibre axis in the top ply. The profile is an effective velocity profile, as it accounts for the directional sensitivity of the FBG sensors.

An initial series of impacts was performed with the setup shown in Fig. 6.4, using the broadband light source shown in Fig. 6.5. However, since the spectrum of the broadband light source is not flat across its wavelength range, each of the signals measured in the three photodetectors suffered from crosstalk, namely each photodetector responded to changes not only in its primary FBG sensor but also to changes in the other sensors. More sophisticated optical circuits could of course be designed to avoid this problem, for example, by detecting the reflected rather than transmitted signals from the FBG filters, which was originally chosen to maximise the detected light intensity. However for the present work a simpler approach

was adopted, namely to isolate each of the FBG sensors and to make independent measurements of each one for each location.

A series of impacts was made at the positions (200,200), (300,180), (240,230), (170,280) and (330, 250). The impact was repeated five times for each sensor and each location, totalling fifteen independent impacts per location, and the arrival times for each sensor were averaged. These arrival times and the velocity profile in Fig. 6.25 were then used to determine the impact locations. Representative individual signals detected by the FBG sensors for an impact at (300,180) and the corresponding loci determined from the average of five individual measurements are shown in Figs. 6.26 and 6.27, respectively. The error on this particular event is 10.2 mm in x and 1.5 mm in y. A compilation of the localisation measurements using FBG sensors and a broadband light source is shown in Fig. 6.28. The impact at (170,280) could not be located since the wave was incident at an angle almost orthogonal to FBG_3, resulting in a poor signal-to-noise ratio. The average error for the other four points was 16 mm in x and 4.5 mm in y.

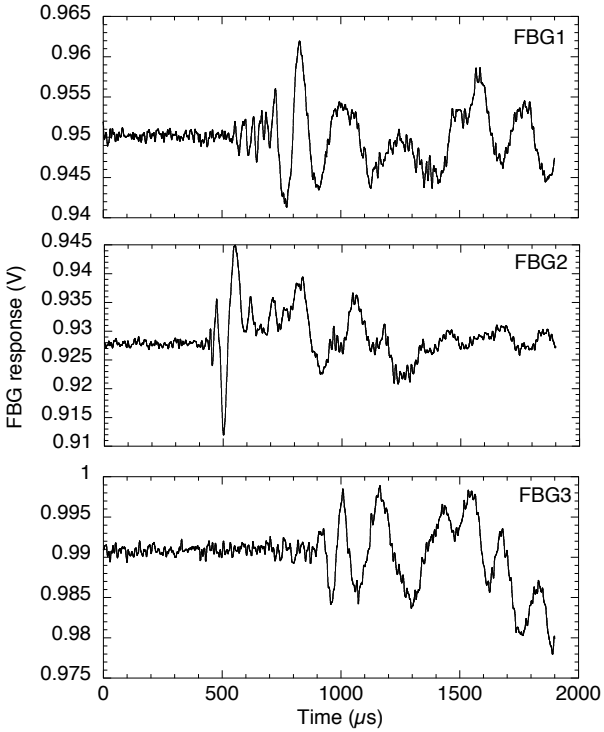

Figure 6.26: Example of individual signals measured in a 0.85 mm-thick composite plate using three FBG sensors located at (150,150), (350,150) and (150,350), respectively. The impact is located at (300,180). A 100 kHz lowpass filter is applied to all signals.

Narrowband laser light source

In order to improve the signal-to-noise ratio, the broadband light source was replaced with a tuneable narrowband laser. The setup was identical to that in Fig. 6.4, but

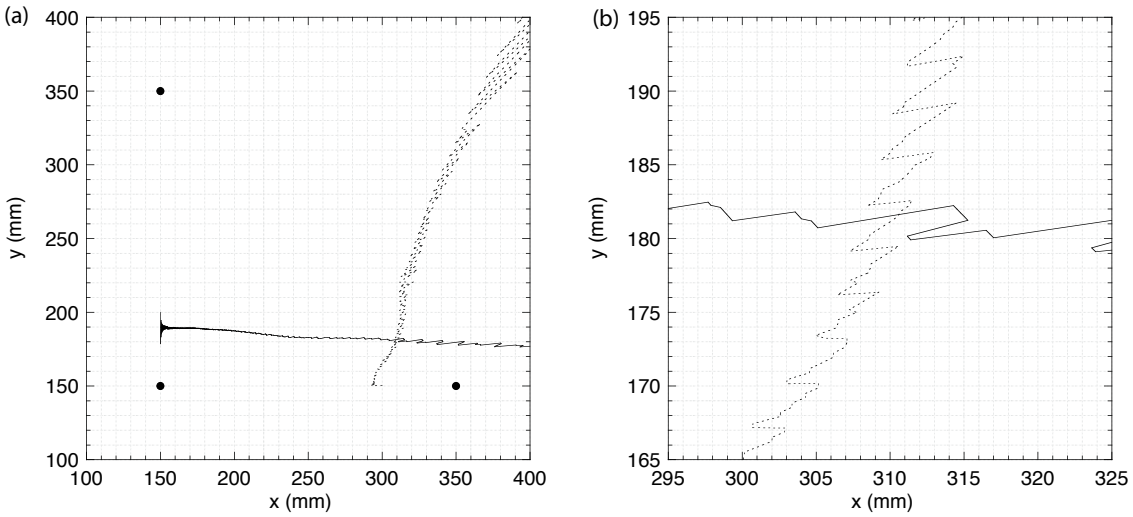

Figure 6.27: Experimentally-determined loci from pairs of FBG sensors for the data in Fig. 6.26: (a) large field of view, and (b) expanded region near the impact point, (300,180). The three solid circles in (a) show the locations of the FBG sensors.

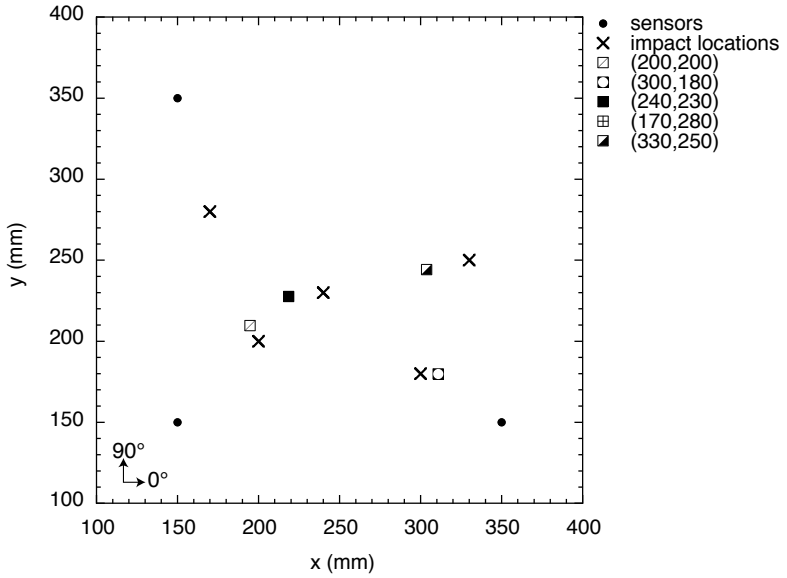

Figure 6.28: Compilation of the impact localisation measurements for a 0.85 mm-thick composite plate using three FBG sensors (indicated by filled circles) illuminated with broadband light. Each point corresponds to the average of five individual measurements.

without the presence of any FBG filters. The sensors were once again interrogated one at a time.

The sensitivities of the FBG-broadband system and the FBG-laser system were first compared. For the FBG-broadband system, each filter was progressively strained using the micrometer stages and the transmitted light was detected by a photodetector. For the FBG-laser system, the optical power of the laser was set to 4 mW[3], the laser wavelength was scanned over a range of about 4 nm, centred on the FBG Bragg wavelength, and the reflected light intensity was measured. The photodetector reading—which is directly proportional to the light intensity—versus wavelength of the FBG-broadband system and FBG-laser system are shown in Figs. 6.29 a and 6.29 b, respectively. The FBG-broadband system shows a 1.2% signal variation for a 0.1 nm strain change corresponding to $\sim$0.15 mV/$\mu\epsilon$ (Fig. 3.13). In contrast, the FBG-laser system shows a larger signal variation of around 15% for a 0.1 nm strain change, corresponding to $\sim$1.3 mV/$\mu\epsilon$ (Fig. 3.13), suggesting that the FBG-laser system will be more sensitive for impact localisation.

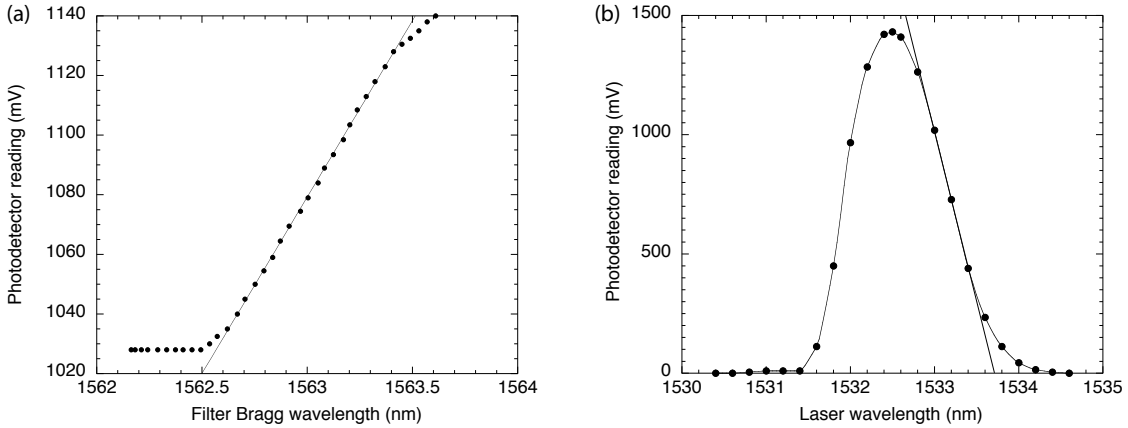

Figure 6.29: Variation of the detected light intensity versus wavelength for (a) the FBG-broadband system, and (b) the FBG-laser system.

Figure 6.30 shows a comparison of the FBG response when illuminated with (a) the broadband source and (b) the narrowband laser, and impacted at a distance of 200 mm and an angle of 0° to the fibre axis. The S_0 mode is clearly visible in the laser signal, arriving around 570 μs. In this exceptional case, there is also some indication of the S_0 mode above the noise level in the FBG-broadband data, most likely due to the force of the impact (c. f. Fig. 6.24).

The angular dependence of the velocity was then determined for the FBG-laser system, as described previously (Fig. 6.31). Due to the lower noise level, the lowpass filter for these data was raised to 300 kHz. A velocity of 6,060 m s^{-1} was measured in the 0° direction, corresponding well with the velocity of the S_0 mode previously measured with PZT sensors (Fig. 6.15 and Table 6.3). However, the lack of sensitivity in the 90° direction is still apparent, and the measured profile in Fig. 6.31 indicates that the FBG-laser system is relatively insensitive to the S_0 mode at other angles.

[3]The maximum input power of the photodetectors was 5 mW

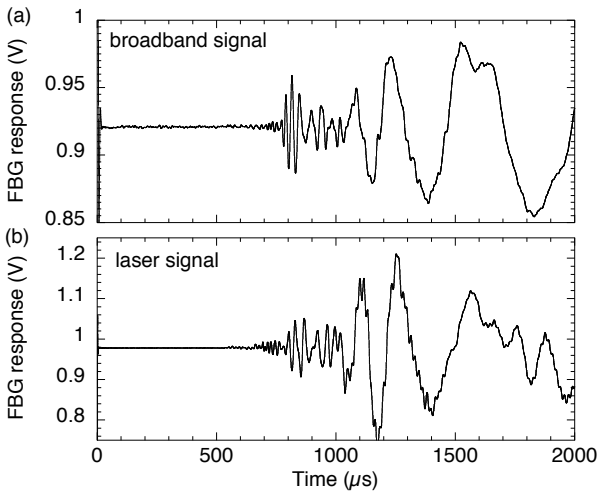

Figure 6.30: Comparison of the FBG response when illuminated with (a) a broadband light source, and (b) a narrowband laser. The impact was performed at a distance of 200 mm and at an angle of 0° relative to the FBG axis. A 300 kHz lowpass filter was applied to both signals. The fractional change of the laser signal is around a factor 4 larger than the broadband signal, in qualitative agreement with the measurements shown in Fig. 6.29.

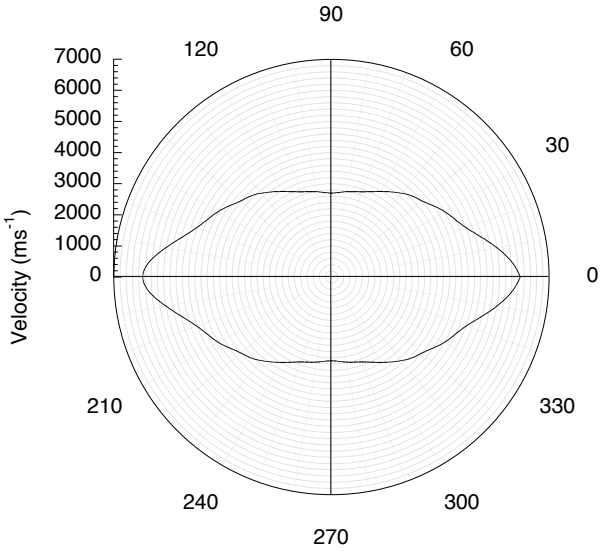

Figure 6.31: Angular dependence of the effective Lamb wave velocity in a 0.85 mm-thick composite panel measured with FBGs illuminated with a narrowband tuneable laser. A 300 kHz lowpass filter is applied to the signals. Zero degrees corresponds to the direction parallel to the FBG axis and also to the carbon fibre axis in the top ply.

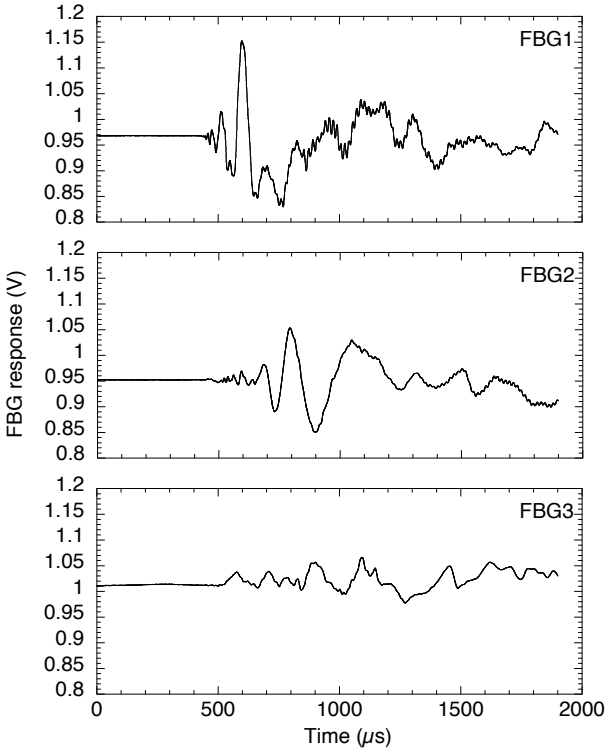

Figure 6.32: Example of individual signals measured in a 0.85 mm-thick composite plate using three FBG sensors located at (150,150), (350,150) and (150,350), respectively, with narrowband laser illumination. The impact is located at (200,200). A 300 kHz lowpass filter is applied to all signals.

Impacts were performed in the same locations as for the broadband system. Figure 6.32 shows representative signals detected by the three FBGs, in this case for an impact at (200,200). The weak signal in FBG_3 is largely due to the near-perpendicular angle of incidence. It is clear that the strong angular dependence on the FBG sensitivity, combined with the (related) strong angular dependence of the wave velocity (Fig. 6.31) will limit the sensitivity and precision of the impact localisation. This is confirmed by the compilation of impact localisations for the FBG-laser system (Fig. 6.33). The average error of these three localisations is 19 mm in x and 11 mm in y, i.e. comparable to those obtained with the broadband light source. It is likely that a more detailed measurement of the angular dependence of the velocity (Fig. 6.31), in 15° increments, could significantly improve this precision.

6.6 Discussion

The measurements presented in this chapter show that a sparse array of FBG strain sensors separated by distances of several tens of centimetres can be used to detect and locate impact events in composite panels, to within a few centimetres. These results have been obtained for realistic impacts, involving many frequency components, and of low energy, producing Lamb waves of small amplitude (typically a few tens of microstrain). Impacts that cause mechanical damage will in general involve

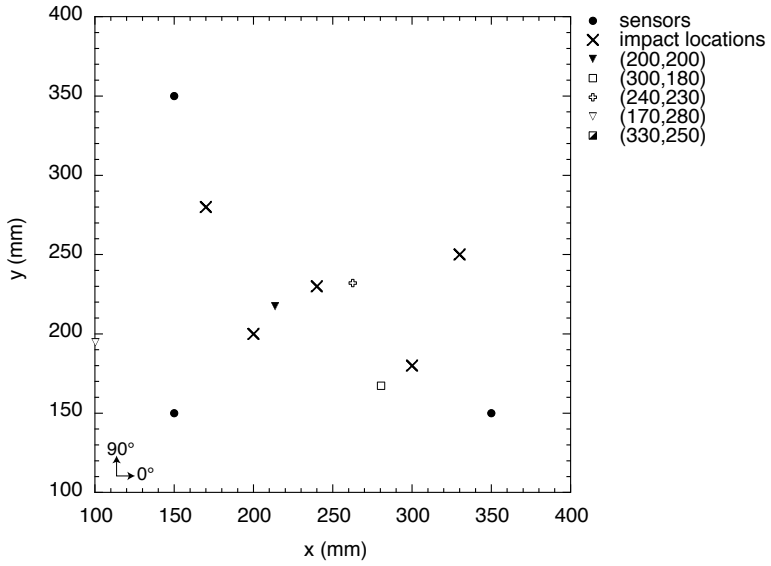

Figure 6.33: Compilation of the impact localisation measurements for a 0.85 mm composite plate using three FBGs (indicated by filled circles) with narrowband laser illumination.

substantially stronger shock waves, which are correspondingly easier to detect and measure. This precision is perfectly adequate for the present application in an Active Sensing and Repair Composite. In this context, once the impact has been located, the shape memory alloy wires covering the area around this point can be activated. The FBGs can then be used as temperature gauges, and provide a dynamic feedback loop to optimise the heating of the SMA wires.

Prior to using FBG sensors for locating the impacts, PZTs were used to confirm that impact events could be accurately located by monitoring propagating Lamb waves. Excellent results were obtained with the PZTs; the impacts were located to within a few millimetres precision. The PZTs show good high frequency response and uniform detection efficiency versus angle of incidence. The good agreement between the measured and known impact positions confirms the validity of the algorithm written in Matlab for localisation in an orthotropic composite plate [174]. The impact position can be located either by measurement of the leading edge of the S_0 mode or of the maximum amplitude of the frequency-selected A_0 mode. Due to its higher propagation velocity, the S_0 mode is less susceptible to confusion from the interference of waves reflected at the boundaries of the plate. However, the A_0 mode has a substantially-larger amplitude for surface impacts and so is less susceptible to noise, background vibrations or to attenuation of the waves as they propagate along the plate.

The application of FBG sensors for impact localisation can be further optimised to address two features, namely (a) the variation of detection sensitivity relative to the axis of the optical fibre, and (b) the overall sensitivity to high frequency and low amplitude S_0 Lamb waves. A promising way to improve the directional sensitivity is to use FBG rosettes, where three FBGs are present at the same point in the composite structure, with their axes aligned at relative angles of 60° [144]. In this

way there would always be one FBG per rosette oriented in an efficient direction for detection of any given impact. This directional effect could also be used to determine the principle propagation direction of the wave [144]. Improvements of the sensitivity of the FBG sensors can be achieved by using a low-noise light source, and through careful design of the optical system, based on the concepts developed in the present work.

Chapter 7

Integration of microcapsules and SMA wires in composite

7.1 Introduction

In this chapter, woven SMA wires and the microcapsule self-healing system are integrated in a carbon fibre composite. The samples are prepared with the post-cure schedule developed in Chapter 5. The compatibility of the microcapsule system with this schedule is first verified by preparing TDCB samples as described in Chapter 4, but post-curing them with the new schedule, and testing their healing performance. Carbon fibre composite samples with embedded SMA wires, microcapsules and Grubbs' catalyst are then made and damaged by low-energy impacts in an accelerated drop-weight impactor system. The ability of the SMA wires to close a delamination is qualitatively demonstrated by measuring the width of the delamination before and after SMA activation, under an optical microscope. Initial self-healing tests are then carried out. The healing performance is quantitatively evaluated with virgin, damaged and healed samples, tested in three-point bend.

7.2 Experimental techniques

7.2.1 Composite fabrication

Carbon fibre/epoxy composite plates both without and with woven SMA wires, microcapsules and Grubbs' catalyst were made. A simple $[0°/90°]_s$ stacking sequence of the carbon fibres was selected to simplify analysis of the repair process of the delaminations. Three different types of samples were prepared to evaluate the healing performance: (1) undamaged samples (2) damaged but unhealed samples and (3) damaged and healed samples. For the first two types of sample, the Grubbs' catalyst wax microspheres were replaced with pure wax microspheres, as these samples did not need to self-heal.

For the samples with SMA wires, the wires were manually woven into the dry carbon fibre bed. The wires were woven parallel to one another, orthogonal to the carbon fibres in the top ply, with a stitching step of about 2-3 mm and a spacing of 2 mm (Fig. 7.1). They were localised in a 20 mm-wide region at the centre of the

span of the three-point bend specimens, to reduce fabrication time. The DCPD microcapsules and the Grubbs' catalyst microspheres (or pure wax microspheres, depending on the sample type) were then mixed into the epoxy resin, in concentrations of 20 wt% and 5 wt%, respectively. After degassing, the mixture was injected between the two central plies of the samples using a syringe. The samples were then sealed in a vacuum bag, and cured at room temperature for 24 hr. Following this, they were removed from the vacuum bag and post-cured in two steps, with the first at 45°C for 6 hr and the second at 75°C for 45 min (this is the post-cure schedule developed in Chapter 5). The final sample thickness was about 1.05 mm, 200 μm more than that of the baseline carbon fibre/epoxy composite (0.85 mm)—due to the presence of the microcapsules. The samples were then cut using a diamond saw to dimensions of 80 mm in length and 25 mm in width, in accordance with ASTM standard D 790 M for three-point bend testing.

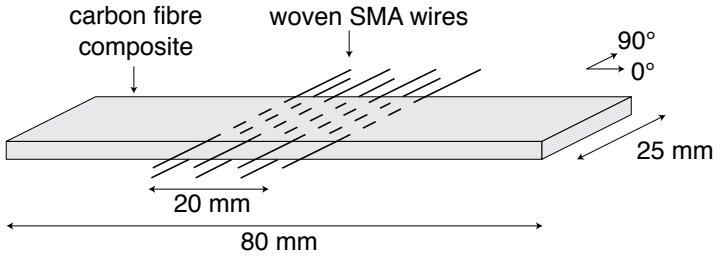

Figure 7.1: Schematic of the self-healing composite three-point bend sample geometry.

7.2.2 Impact testing

The samples were impacted at low energy (∼3 J) in a Rosand accelerated drop-weight impact tester (Fig. 7.2). The samples were individually placed at the base of the impact tower, under the drop-weight, and were held in place by two hydraulic annular steel clamps with a 23 mm inner diameter. The striker was accelerated towards the sample with a bungee cord. The mass of the striker was 171 g, and the total mass of the striker and the weight frame was 4,459 g. Event recording was triggered by a flag, attached to the drop mass, passing through an optical gate just before impact. A Kistler transducer in the striker recorded the force throughout the impact event. From this, the acceleration, velocity and displacement of the drop mass were calculated. Finally, the energy absorbed by the sample was calculated. The striker was caught upon rebound to prevent a second impact.

Impact energy

An impact energy that was sufficient to induce delamination without causing extensive fibre damage was sought. This was evaluated by clamping composite samples with a surface area of $50 \times 50\,\text{mm}^2$ in the 23 mm-diameter impactor clamps, impacting them at energies in the range 1–8 J, and then using ultrasonic C-scan

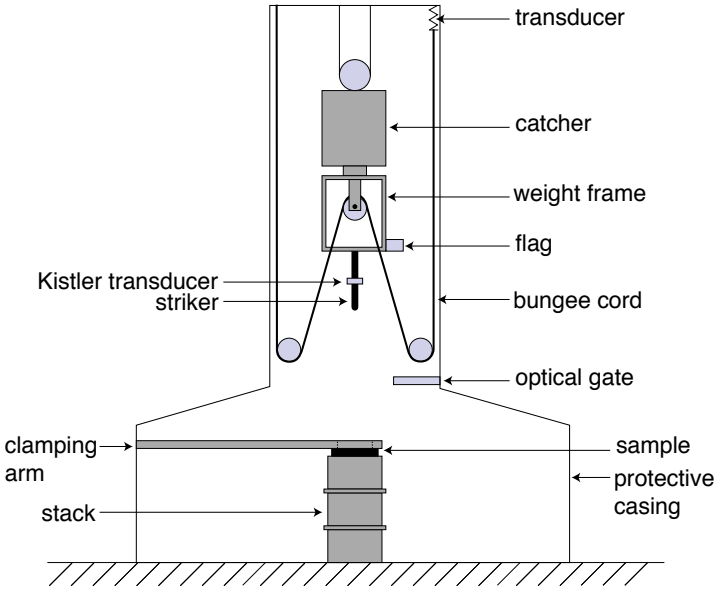

Figure 7.2: Schematic of the Rosand accelerated drop-weight system.

non-destructive testing to determine the extent of delamination. For C-scan analysis, the sample was mounted on a reflecting back plate, and placed in a water bath, which served as a coupling agent. A Harisonic piezoelectric transducer generating a 15 MHz signal was placed 35 mm above the sample. The transducer operated as both the emitter and the detector; it was used in the pulse-echo mode. The probe was scanned in a raster fashion over the surface of the sample. The propagating sound wave was attenuated by the damaged region. In this way, a 2D map (C-scan) of the composite damage was determined. Figure 7.3 shows representative C-scans for impacts at 0, 3 and 6 J. At 3 J, the delaminated zone had a diameter of about 10 mm, and at energies above about 3 J, cracks propagated radially from the impact point to the sample edges. An impact energy of 3 J was, therefore, selected.

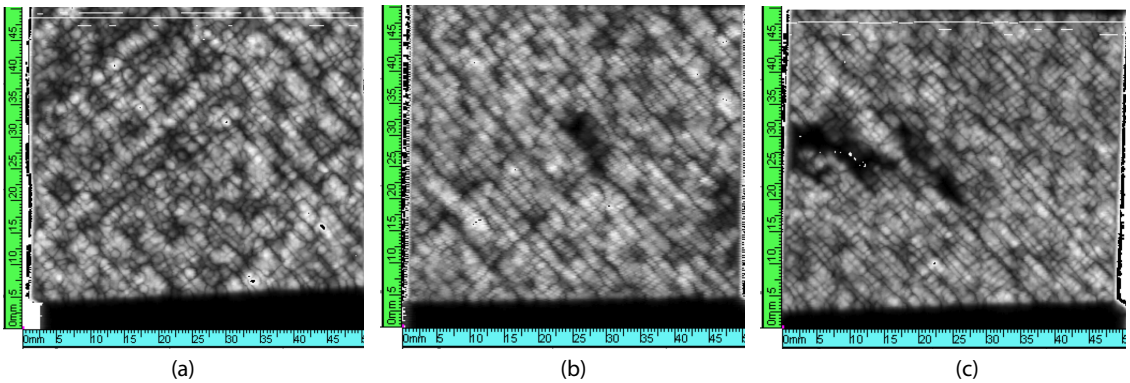

Figure 7.3: C-scan images of the composite plate (a) before impact and after impact at (b) 3J and (c) 6J. The units of the x- and y-axes are mm.

7.2.3 Delamination closure

Before performing self-healing tests, the ability of the SMA wires woven into the carbon fibre composite to close a delamination was tested. The carbon fibres in the composite have a resistivity of about 1,000-4,000 $\mu\Omega$cm, while the activated SMA wires have a resistivity of about 100 $\mu\Omega$cm (Fig. 3.12); the carbon fibres have a resistivity 10-40 times higher than that of the SMA wires. There should, therefore, be little current leakage in the material when the SMA wires are activated. Furthermore, the epoxy matrix is highly-insulating.

Samples were impacted as described in §7.2.2. Each sample was then cut in half—through the centre of the delaminated zone—with a diamond saw. This face of the sample was polished, for observation under optical microscope. The sample was placed edge-on under the microscope, so that the delamination was visible. The embedded SMA wires were connected in series to an electrical power supply, and a current of 0.3 A was applied. (Currents of 0.1 A per wire and 0.2 A per wire were first tested, but did not induce crack closure.) Microscope images of the delaminations before and after activation were taken, and the widths were compared.

7.2.4 Healing performance

The self-healing performance of the samples was evaluated with three-point bend tests, in accordance with ASTM standard D 790 M. Samples were prepared as described in §7.2.1. Virgin, damaged and healed samples were tested. The virgin samples were tested directly after fabrication. The damaged samples were impacted as described in §7.2.2 and then tested. Healing was impeded in these samples as they were prepared with pure wax microspheres rather than with Grubbs' catalyst wax microspheres. Finally, the healed samples were prepared by damaging them as described in §7.2.2, and then activating the embedded SMA wires for a 30 min healing period, with 0.3 A per wire. Following this, the samples were left at room temperature for 24 hr before testing in three-point bend.

For testing, the samples were supported horizontally at a span of 51 mm, and were loaded at the mid-point at a 5.1 mm/min rate of crosshead motion, in accordance with ASTM standard D 790 M. The load-deflection data was recorded. After testing, the maximum fibre stress, occurring at the mid-span, was determined for each sample, using

$$S = \frac{3PL}{2bd^2}\left[1 + 6\left(\frac{D}{L}\right)^2 - 4\left(\frac{d}{L}\right)\left(\frac{D}{L}\right)\right] \tag{7.1}$$

where P (N) is the load at a given point in the load-deflection curve, L (mm) is the support span, b (mm) is the beam width, d (mm) is the thickness of the beam and D (mm) is the deflection at the center-line of the specimen. The flexural strength of the material is the value of S at the moment of breaking, when $P = P_{crit}$. The flexural strain is given by

$$\epsilon_f = \frac{6Dd}{L^2} \tag{7.2}$$

and the flexural modulus is then the gradient of the plot of S versus ϵ_f.

7.3 Verification of microcapsule compatibility with post-cure schedule

Two TDCB samples, each with three embedded SMA wires and 5 wt% Grubbs' catalyst wax microspheres were prepared following the procedure described in §4.2.1, with the new post-cure schedule developed in Chapter 5. The samples were fractured a first time by tapping a razor blade into the crack groove with a hammer. The crack was then injected with 20 μl of DCPD. The standard heat cycle of 0.5 A per wire for 30 min was then applied to the wires, and the samples were re-tested after 24 hr. The samples had healed peak loads of 44.6 N and 58.2 N for fill factors of $\sim$1.5 and 2.4, respectively, in good agreement with the results in Fig. 4.18, confirming that the healing system is compatible with the new post-cure schedule. An example of a healed loading curve is shown in Fig. 7.4.

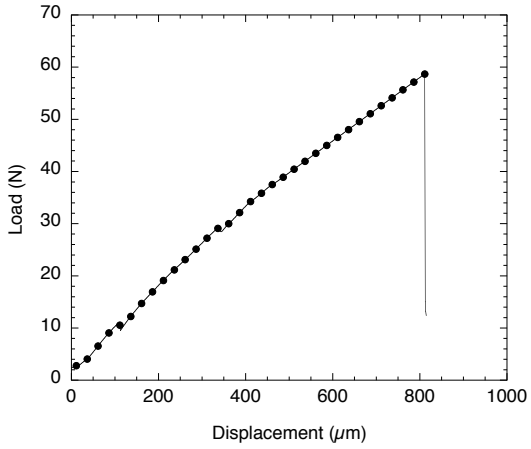

Figure 7.4: Healed load versus displacement for a TDCB sample prepared using the post-cure schedule developed in Chapter 5, with embedded Grubbs' catalyst and SMA wires, and injected with 20 μl of DCPD.

7.4 Delamination closure

Three carbon-fibre composite samples with woven SMA wires but without microcapsules were prepared as described in §7.2.1, with bundles of one, two and three wires, respectively. The samples had a thickness of about 0.85 mm, so the volume fraction of the SMA wires in the samples was about 1.2%, 2.4% and 3.6%, respectively. The samples were impacted as described in §7.2.2. The plots of impact force and energy absorbed by the samples versus time are shown in Fig. 7.5 and 7.6, respectively. There is indication from both of these plots that the resistance to impact damage was increased somewhat by the SMA wires: (i) In Fig. 7.5, the jagged peaks in the curve for the single wire sample indicate the occurrence of damage. These peaks become less pronounced with increasing volume fraction of SMA wires. (ii) Figure 7.6 indicates that the rebound energy increased with increasing SMA wire volume fraction, meaning that the total energy absorbed by the sample decreased.

These results, however, should only be taken as an indication; further tests would need to be performed to statistically confirm this trend.

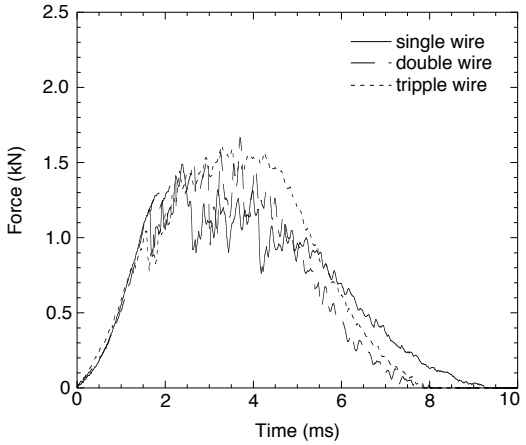

Figure 7.5: Striker force exerted on composite plates with woven SMA wires during impact.

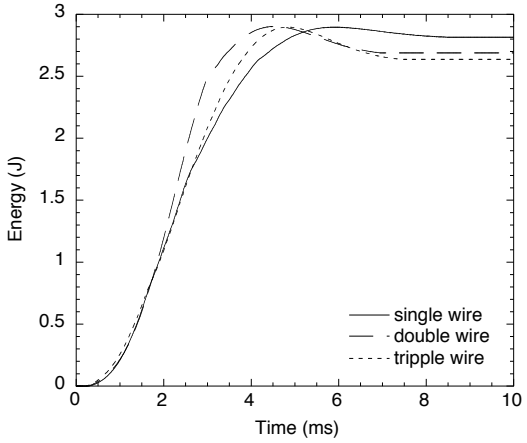

Figure 7.6: Energy absorbed by composite plates with woven SMA wires during impact.

The samples were then sectioned and polished as described in §7.2.3. The single-wire sample (SMA $V_f \simeq 1.2\%$) was then placed under an optical microscope and the SMA wires were activated as described in §7.2.3. Figure 7.7 shows a segment of the delamination, and a woven SMA wire can be seen bridging it in two locations. Figures 7.8 and 7.9 are the close-field view of Fig. 7.7, before and after SMA wire activation, respectively. It was difficult to obtain a perfectly-polished sample because the samples could not be embedded in a support resin during the polishing stage; the support resin would have had the effect of constraining the sample and, therefore, inhibiting crack closure by the SMA wires. Nonetheless, Figs. 7.8 and 7.9 clearly show that the crack faces were brought closer to one another upon activation of the SMAs. This was repeatable in other samples. Table 7.1 summarises the crack opening both before and after wire activation at the six points indicated in Fig. 7.8. On average, the crack volume was reduced by 45%.

Table 7.1: Comparison of the width of the delamination in Fig. 7.7 before and after SMA activation. The six locations are indicated on Fig. 7.8.

Location	Delamination width		
	Before SMA activation [μm]	After SMA activation [μm]	Reduction [%]
1	50.1	37	26
2	37.4	20.3	46
3	43.7	19.1	56
4	21.2	11.2	47
5	13.3	9.9	26
6	13.3	4.0	70

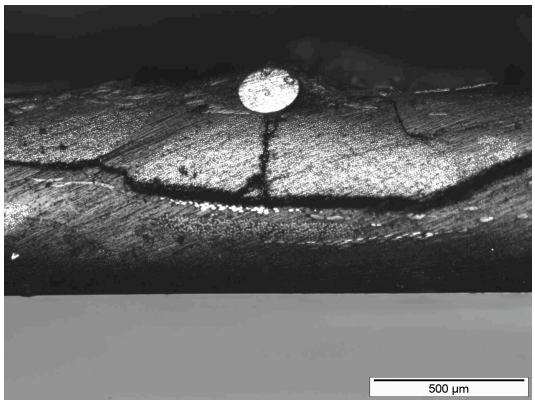

Figure 7.7: Global view of the delamination before SMA wire activation. The bright circle at the top centre of the image is a segment of SMA wire that has been polished. The SMA wire can be seen to weave through the carbon fibres (darker shadow), crossing the delamination plane twice, toward the two extremities of the image.

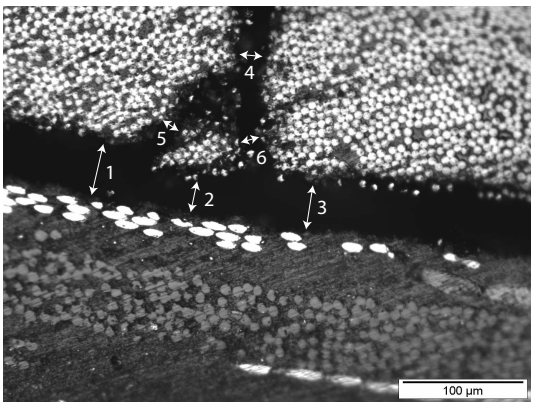

Figure 7.8: Expanded image of Fig. 7.7, before SMA wire activation.

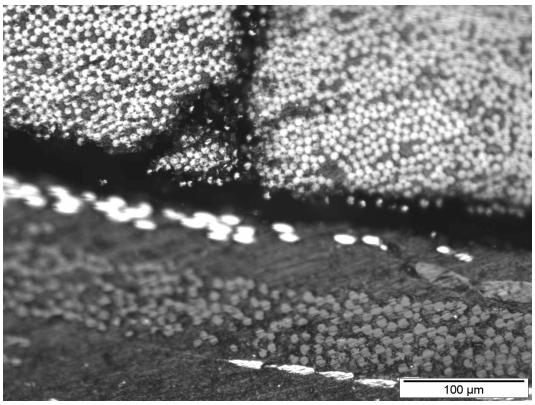

Figure 7.9: Expanded image of Fig. 7.7, after SMA wire activation.

7.5 SMA and microcapsule influence on composite mechanical properties

The influence of the microcapsules and the SMA wires on the flexural strength of the composite was evaluated with three-point bend tests. Three types of samples were prepared: (1) pure composite samples, (2) composite samples with embedded microcapsules and (3) composite samples with embedded, woven SMA wires. Each of these three samples were tested in three-point bend, both before and after impact. The test was repeated three times for each sample type, and the data were averaged. The results are summarised in Fig. 7.10. Addition of the microcapsules significantly reduced the flexural strength of the composite, as they degraded the interlaminar bonding of the samples. The SMA wires also somewhat reduced the flexural strength of the composite, as they induced some waviness in the carbon fibres. The flexural strength after impact of all three types of sample decreased proportionally.

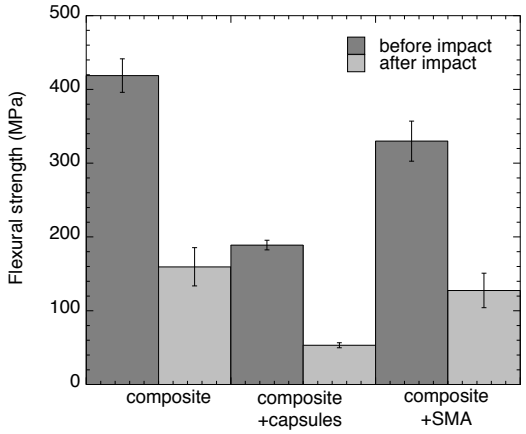

Figure 7.10: Flexural strength, measured with three-point bend tests, for (1) composite samples (2) composite samples with embedded microcapsules and (3) composite samples with embedded SMA wires, before and after impact.

7.6 Healing performance

The healing performance was evaluated with two types of carbon fibre composite sample: (1) samples with embedded microcapsules and Grubbs' catalyst and (2) samples with embedded microcapsules, Grubbs' catalyst and woven SMA wires. The samples were impacted, and tested in three-point bend both before and after healing. Three tests were repeated for each sample type, and the data were averaged. The fibre stress versus flexural strain plots for samples without SMA wires, before and after healing, are shown in Fig. 7.11 a and b, respectively, and the fibre stress versus flexural strain plots for samples with SMA wires, before and after healing, are shown in Fig. 7.12 a and b, respectively. The average failure strengths from these four plots are summarised in Fig. 7.13.

Both the samples without and with SMA wires recovered some of their original flexural strength after healing (Fig. 7.13). The addition of SMA wires improved the

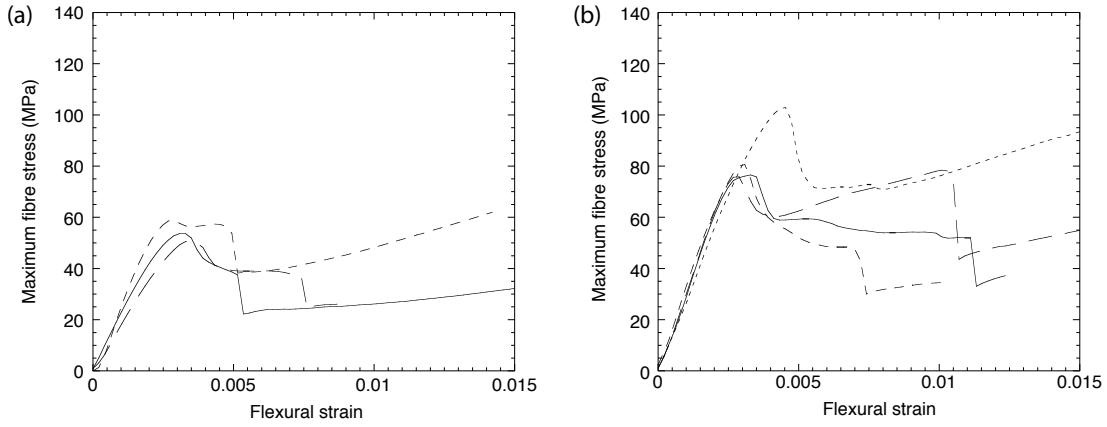

Figure 7.11: Three-point bend data for composite samples with embedded microcapsules and Grubbs' catalyst after impact and (a) before healing (b) after healing.

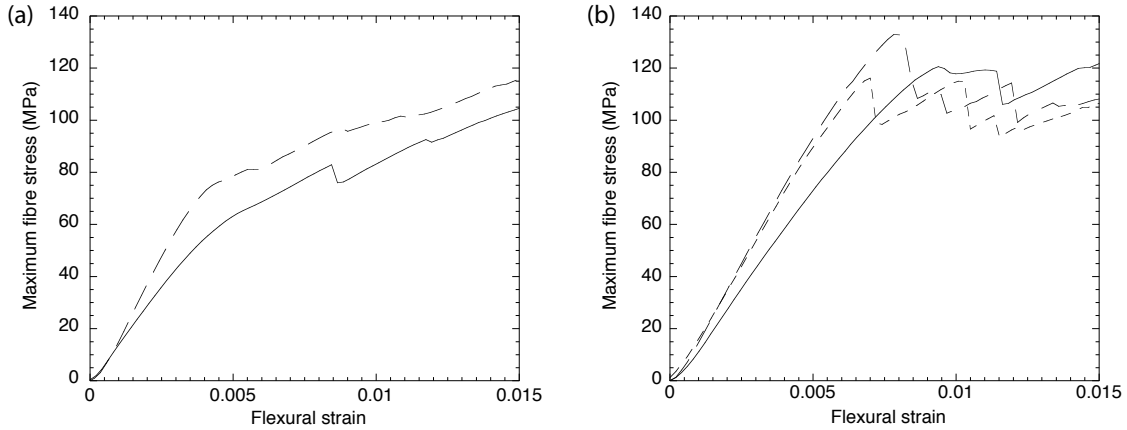

Figure 7.12: Three-point bend data for composite samples with embedded microcapsules, Grubbs' catalyst and SMA wires after impact and (a) before healing (b) after healing.

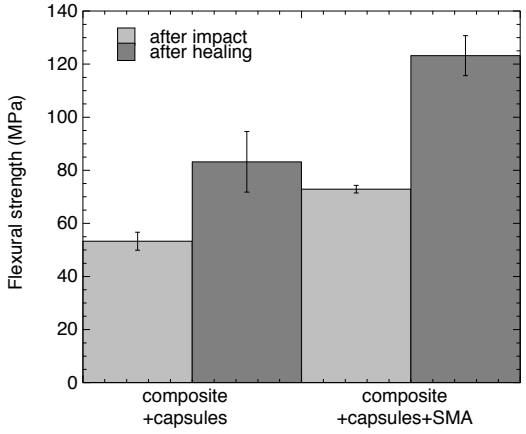

Figure 7.13: Summary of the data in Figs. 7.11 and 7.12.

healing performance, relative to a sample without wires. This is likely due to the combined effect of the SMA wires both increasing the resistance to delamination damage and improving the healing process once damage has occurred, by reducing the delamination volume and heating the healing agent. Although these first tests do demonstrate the potential benefit of the SMA wires, comparison of Figs. 7.10 and 7.13 confirm that significant optimisation of sample preparation (microcapsule distribution and SMA layup, for example) is needed in order to achieve healed properties that are comparable to the properties of the original material.

7.7 Discussion

Initial self-healing of carbon fibre composite samples containing both woven SMA wires and the microcapsule self-healing system was demonstrated. Samples were impacted at low energy, to induce delamination without causing extensive fibre damage. Delamination widths were significantly reduced by activation of the woven SMA wires. The healing performance was then evaluated with three-point bend tests, both before and after healing. These first tests have shown that the addition of SMA wires to the material increase the healing performance. This is likely due to a combination of increased resistance to delamination damage, and delamination closure and healing agent heating when the SMA wires are activated. Further tests would be necessary to understand the relative impacts of these two factors.

Although these first tests have demonstrated the feasibility of a self-healing composite with SMA wires and microcapsules, the system must be optimised so that healed properties approach those of the virgin material. Importantly, the microcapsules drastically reduced the interlaminar strength. This effect could be minimised by using smaller capsules, such as nano-capsules [32], that would have a better dispersion in the matrix, and would affect the interlaminar thickness less. In addition, delamination closure was achieved here with a relatively small volume fraction (1.2%) of SMA wires. However, as the stiffness of the composite material increases, the volume fraction and diameter of the SMA wires will need careful tailoring.

Chapter 8

Conclusion

The work presented here has demonstrated that a carbon fibre composite material with active sensing and repair functionality can be successfully prepared. This was achieved by incorporating three additional components in the structure: microcapsules containing a liquid healing agent (and a catalyst for its polymerisation), shape memory alloy wire actuators and fibre Bragg grating strain sensors.

Embedding active SMA wires in the self-healing epoxy matrix was shown not only to close cracks without the need for manual intervention, but also to substantially increase the healing performance of the material, by a factor of 1.6. Using a tapered double cantilever beam sample geometry and fracture test to evaluate the healed performance, the average healed peak load was 38 N and 60 N for samples without and with SMA wires, respectively. This corresponds an increase in healing efficiency from 49% without SMA wires to 77% with SMA wires, relative to the virgin material. The improved performance was found to be due both to a reduced crack volume and to an improved polymerisation of the healing agent.

A liquid composite moulding cure schedule compatible with epoxy containing embedded SMA wires was successfully developed. The cure schedule consisted of a room-temperature cure for 24 hr, followed by a two-step post-cure process with the first step at 45°C for 6 hr and the second step at 75°C for 45 min. The SMA wires were set in the epoxy resin upon gelation of the resin. This occurred at room temperature, where there was no risk of SMA activation. Subsequently, during the post-cure period, the maximum processing temperature exceeded the activation temperature of the SMA wires. However, the wires remained well-bonded to the matrix and, therefore, no longer required an external frame to prevent them from contracting. The resulting epoxy had excellent thermal and mechanical properties. In particular, the epoxy/SMA interface was found to have an interfacial shear strength well above the maximum interfacial shear stress an SMA wire activated at 80°C. Cyclic activation tests of a multi-SMA wire/epoxy sample confirmed that the SMA wires did indeed remain bonded to the matrix.

The use of FBG sensors to precisely locate remote impact sites on composite panels was also successfully demonstrated. Impacts on carbon fibre composite plates were located to within a few centimetres using a sparse array of FBG strain sensors spaced several tens of centimetres apart. This precision is sufficient for application in an active sensing and repair composite, allowing selective activation of only those SMA wires that cross the region of damage. This work involved the development of

a simple and elegant technique to read out the FBGs at sampling rates of 10 MHz, using a broadband light source and twinned FBGs acting as sensor-analyser pairs. Impacts were located by relative time-of-flight measurements of the Lamb waves generated by the impact to the sensors. An algorithm for locating impacts in orthotropic plates [174] was written in Matlab and implemented. Impacts were first located using the more commonly used piezo-ceramic sensors. Excellent results were obtained, confirming firstly that the impacts were generating Lamb waves an secondly the validity of the algorithm. The impacts could be located using either the S_0 mode or the frequency-selected A_0 mode. While the S_0 mode is less susceptible to confusion from to boundary reflections, due to its higher velocity, the A_0 mode has a larger amplitude and, therefore, is less susceptible to attenuation, and has a better signal-to-noise ratio.

Finally, prototype self-healing carbon-fibre composite samples were fabricated, containing woven SMA wires, embedded microcapsules and Grubbs' catalyst. These first tests on the combined material successfully demonstrated the closure of delaminations upon SMA activation, confirming the suitability of SMA weaving for this application.

The next step is now to integrate these components into a single material, and to optimise both the material's processing and its final properties. One key processing issue will be how to weave the SMA wires into the material. They could either be incorporated into the carbon fibre fabric as these are being woven, in one step, or in a separate stitching step, following the fabrication of the carbon fibre fabric. Another important processing issue will be to determine when the microcapsules should be incorporated, to ensure a homogeneous distribution in the matrix. They could either be laid out in the dry carbon fibre bed, before infusion, or they could be mixed into the epoxy resin and infused. In the case of the latter, however, the viscosity of the epoxy/microcapsule mixture is currently too high. One likely solution to this will be to explore other mechanisms for the delivery of the healing agent and its hardener, that are more compatible with current composite processing routes, and, furthermore, capable of multiple healing events. Impact localisation with FBG sensors can be further optimised by laying the FBGs in a rosette configuration, which will effectively minimise the directional sensitivity of these sensors. In terms of the final properties of the material, the volume fractions of each of the three additional components should be optimised so that they are most effective at performing their respective functions and they increase the sensing and healing performance of the structure without detrimentally affecting the mass per unit volume of the final material.

In conclusion, all the components of the proposed Active Sensing and Repair Composite have been successfully developed and, moreover, shown to substantially improve its self-healing performance. This outcome was by no means clear when the concept for this material was originated at the start of this thesis research work, four years ago. The results obtained in this thesis successfully validate the scientific concept of the material.

Appendix A

Localisation equations for isotropic plate

The impact localisation problem in an isotropic plate is solved using a classical triangulation procedure, developed by Tobias *et al.* [171]. Consider a thin isotropic plate with three strain sensors placed arbitrarily on it in a triangle at positions S_0, S_1 and S_2 with known co-ordinates (0,0), (x_1,y_1) and (x_2,y_2), respectively, Fig. A.1. An impact at a point P(x,y) causes a strain pulse to radiate out from this point. The pulse is detected by the three sensors, where the time-of-flight is proportional to the sensors' respective distances r, $r+\delta_1$ and $r+\delta_2$ from P, i. e. P is located at the point of intersection of three circular loci around S_0, S_1 and S_2 with radii r, $(r+\delta_1)$ and $(r+\delta_2)$, respectively. The equations of these loci are

$$x^2 + y^2 = r^2 \tag{A.1}$$

$$(x-x_1)^2 + (y-y_1)^2 = (r+\delta_1)^2 \tag{A.2}$$

$$(x-x_2)^2 + (y-y_2)^2 = (r+\delta_2)^2 \tag{A.3}$$

We seek the values of r and θ in Fig. A.1. Subtracting Eq. A.1 from Eqs. A.2 and A.3:

$$2xx_1 + 2yy_1 = \left({x_1}^2 + {y_1}^2 - {\delta_1}^2\right) - 2r\delta_1 \tag{A.4}$$

$$2xx_2 + 2yy_2 = \left({x_2}^2 + {y_2}^2 - {\delta_2}^2\right) - 2r\delta_2 \tag{A.5}$$

and changing Eqs. A.4 and A.5 to polar co-ordinates gives

$$2r\left(x_1\cos\theta + y_1\sin\theta + \delta_1\right) = A_1 \tag{A.6}$$

$$2r\left(x_2\cos\theta + y_2\sin\theta + \delta_2\right) = A_2 \tag{A.7}$$

where

$$A_1 = {x_1}^2 + {y_1}^2 - {\delta_1}^2 \tag{A.8}$$

$$A_2 = {x_2}^2 + {y_2}^2 - {\delta_2}^2 \tag{A.9}$$

From Eqs. A.6 and A.7

$$\begin{aligned} r &= \frac{A_1}{2\left(x_1\cos\theta + y_1\sin\theta + \delta_1\right)} \\ &= \frac{A_2}{2\left(x_2\cos\theta + y_2\sin\theta + \delta_2\right)} \end{aligned} \tag{A.10}$$

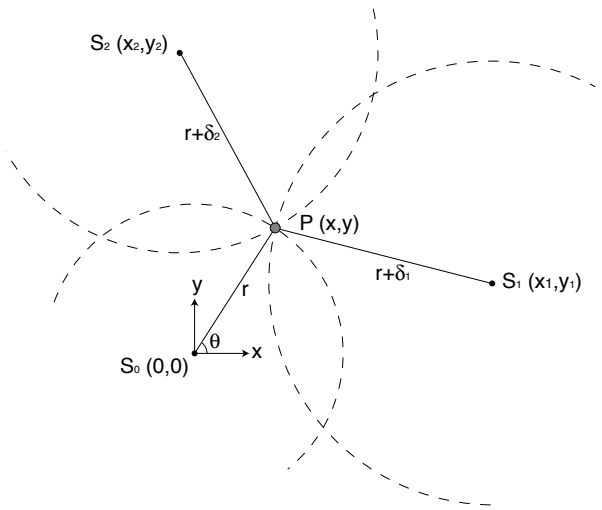

Figure A.1: Impact localisation geometry in an isotropic plate with three sensors (S_i, $i = 1, 2, 3$) [171]. The impact occurs at point P(x,y), causing a strain pulse to propagate through the material. The sensors detect the pulse at a time proportional to their distance from the source (r, (r+δ_1) or (r+δ_2)).

where the distances δ_1 and δ_2 are experimenally-determined from the difference in times-of-flight, Δt_1 and Δt_2, between the two sensor pairs S_0/S_1 and S_0/S_2, respectively, as the group velocity is known. So θ is the only unknown. From Eq. A.10

$$(A_1x_2 - A_2x_1)\cos\theta + (A_1y_2 - A_2y_1)\sin\theta \;=\; A_2\delta_1 - A_1\delta_2 \tag{A.11}$$

Dividing by $B = \left[(A_1x_2 - A_2x_1)^2 + (A_1y_2 - A_2y_1)^2\right]^{1/2}$ and defining $K = A_2\delta_1 - A_1\delta_2/B$ gives Eq.A.11 in the form

$$\cos(\theta - \phi) \;=\; K \tag{A.12}$$

where

$$\tan\phi \;=\; \frac{A_1y_2 - A_2y_1}{A_1x_2 - A_2x_1} \tag{A.13}$$

Eq. A.13 defines a unique solution for ϕ, and θ is then

$$\theta \;=\; \phi + \cos^{-1}K \tag{A.14}$$

This value of θ is then substituted into Eq. A.10 to give r, thereby fully defining the impact location, where the cartesian co-ordinates are given by

$$x = r\cos\theta \tag{A.15}$$

$$y = r\sin\theta \tag{A.16}$$

Appendix B

Localisation equations for orthotropic plate

A closed-form triangulation method cannot be used for locating impact events in orthotropic plates, due to the directional dependence of the Lamb wave velocity. Instead, an iterative algorithm based on an optimisation scheme that minimises an error function is implemented [174]. The only necessary prior knowledge is the position of the three sensors and the Lamb wave velocity profile. Figure B.1 is a schematic of the geometry on which the algorithm is based. The difference in arrival time of the wave at the S_0 and S_1 sensors is first considered, and a locus of possible solutions whose points satisfy this difference is determined. This is then repeated for the S_0 and S_2 sensor couple. The intersection of the two loci is the calculated impact point.

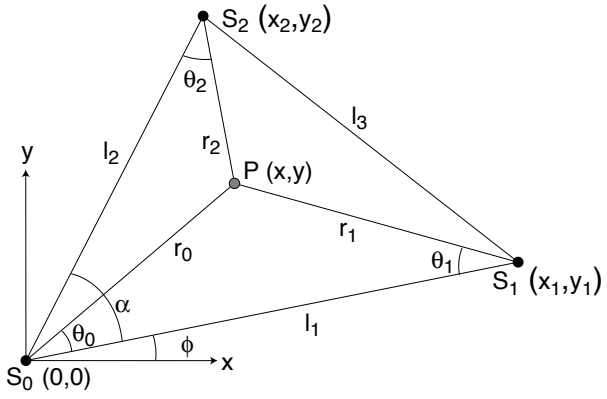

Figure B.1: Impact localisation geometry for an orthotropic plate with three sensors (S_i, i = 0,1,2) [174]. The impact occurs at the point P(x,y).

The wave propagation directions are

$$PS_0 \quad : \quad \theta_0 + \pi + \phi \tag{B.1}$$

$$PS_1 \quad : \quad 2\pi - \theta_1 + \phi \tag{B.2}$$

$$PS_2 \quad : \quad \theta_2 + \alpha + \phi \tag{B.3}$$

Consider first the S_0 and S_1 sensor pair. The difference in arrival time is

$$\Delta t_1 = t_1 - t_0 = \frac{r_1}{c_{g1}} - \frac{r_0}{c_{g0}} \tag{B.4}$$

where c_{g0} and c_{g1} are the group velocities in the PS_0 and PS_1 directions, respectively. From the sine law

$$\frac{\sin\theta_0}{r_1} = \frac{\sin\theta_1}{r_0} = \frac{\sin(\theta_0+\theta_1)}{l_1} \tag{B.5}$$

which gives us

$$r_0 = \frac{l_1 \sin\theta_1}{\sin(\theta_0+\theta_1)} \tag{B.6}$$

$$r_1 = \frac{l_1 \sin\theta_0}{\sin(\theta_0+\theta_1)} \tag{B.7}$$

Eqs. B.6 and B.7 are then substituted in Eq. B.4 to give

$$\frac{l_1 \sin\theta_0}{c_{g1}\sin(\theta_0+\theta_1)} - \frac{l_1 \sin\theta_1}{c_{g0}\sin(\theta_0+\theta_1)} = \Delta t_1 \tag{B.8}$$

However, since the group velocity depends on the propagation direction, Eq. B.8 does not have an analytical solution. Instead, a numerical method must be used. To do so, Eq. B.8 is rearranged to define a cost function (J_1):

$$J_1 = \left| l_1 c_{g0}\sin\theta_0 - l_1 c_{g1}\sin\theta_1 - \Delta t c_{g0} c_{g1}\sin(\theta_0+\theta_1) \right| \tag{B.9}$$

For a fixed θ_0, θ_1 is iterated through and J_1 is calculated each time. A small increment is then made to θ_0 and the process is repeated. For each θ_0, the θ_1 that minimises J_1 is recorded. These θ_0-θ_1 pairs are then used in the equations

$$x = r_0\cos(\theta_0+\phi) = \frac{l_1\sin\theta_1}{\sin(\theta_0+\theta_1)}\cos(\theta_0+\phi) \tag{B.10}$$

$$y = r_0\sin(\theta_0+\phi) = \frac{l_1\sin\theta_1}{\sin(\theta_0+\theta_1)}\sin(\theta_0+\phi) \tag{B.11}$$

to produce a locus of possible impact locations. This process is repeated for the S_0 and S_2 sensor pair, yielding a second cost function and the equations

$$x = r_0\cos(\theta_0+\phi) = \frac{l_2\sin\theta_2}{\sin(\alpha-\theta_0+\theta_2)}\cos(\theta_0+\phi) \tag{B.12}$$

$$y = r_0\sin(\theta_0+\phi) = \frac{l_2\sin\theta_2}{\sin(\alpha-\theta_0+\theta_2)}\sin(\theta_0+\phi) \tag{B.13}$$

which produce a second locus. The impact point is where the two loci intersect.

Appendix C

Academic work

Papers

- E.L. Kirkby, J.D. Rule, V.J. Michaud, N.R. Sottos, S.R. White, J.-A. Månson: Embedded shape memory alloy wires for improved performance of self-healing polymers. *Advanced Functional Materials* **18**, 2253-2260 (2008).

- E.L. Kirkby, V.J. Michaud, N.R. Sottos, S.R. White, J.-A. Månson: Performance of self-healing epoxy with microencapsulated healing agent and shape memory alloy wires. Accepted for publication in *Polymer*.

- E.L. Kirkby, J. O'Keane, R. de Oliveira, V.J. Michaud, J.-A. E. Månson: Tailored processing of epoxy with embedded shape memory alloy (SMA) wires. Submitted to *Smart Materials and Structures*.

Conferences

- SPIE Smart Structures and Materials, 14^{th} international symposium, March 18–22 2007, San Diego, California. Active repair of self-healing polymers with shape memory alloy wires. *Invited speaker*.

- First International Conference on Self-Healing Materials, April 18–20 2007, Noordwijk, The Netherlands. Active repair of self-healing polymers using shape memory alloy wires. *Oral presentation*.

- Thirteenth European Conference on Composite Materials, June 2–5 2008, Stockholm, Sweden. Low temperature moulding of adaptive composites with embedded shape memory alloy wires. *Oral presentation by Dr. V. Michaud*.

- Nineteenth International Conference on Adaptive Structures and Technologies, October 6–9 2008, Ascona, Switzerland. Damage sensing in a self-healing material using fibre Bragg grating sensors. *Oral presentation by Dr. V. Michaud*.

- Second International Conference on Self-Healing Materials, June 28–July 1 2009, Chicago, United States. *Oral presentation by Dr. V. Michaud*.

Doctoral school courses

- Principles of chemical surface characterization of materials, Prof. H.J. Mathieu (2004; 3 credits).
- Non-destructive evaluation techniques, Dr. Thomas Lüthi (2005; 2 credits).
- Composite processing and modelling, Dr. V. Michaud, Prof. J. Nairn (2005; 1 credit).
- Intensive SEM training, Prof. P. Buffat *et al.* (2006; 2 credits).
- Management and innovation of technology, Prof. J.-J. Palthenghi *et al.* (2007; 3 credits).
- Science and technology of UV-induced polymerization, Dr. Y. Leterrier *et al.* (2008; 1 credit).

Undergraduate projects

- L. Germond: Fermeture de fissure par une fibre d'alliage à mémoire de forme dans une matrice époxy. Bachelors project, Summer semester (2005).
- M. Stuer: Pull-out d'un fil d'alliage à mémoire de forme d'une matrice époxy. Bachelors project, Winter semester (2005).
- D. Watson. Summer internship (2008).

Graduate projects

- J. O'Keane: Liquid Composite Moulding of Adaptive Composites. Masters diploma project, Winter semester (2006).

Press

- Les 'smart composites': des matériaux intelligents. *Horizons*, March 2007.
- Les matériaux deviennent intelligents et pourront bientôt s'autoréparer. *Le Temps*, November 2007.
- Self-healing hulls. *IEEE Spectrum*, November 2008.

Bibliography

[1] D. Hull, T.W. Clyne: An Introduction to Composite Materials, Second Edition. Cambridge University Press, Cambridge. (1996)

[2] K.K. Chawla: Composite Materials: Science and Engineering, Second Edition. Springer-Verlag New York, LLC. (1998).

[3] www.boeing.com

[4] S.R. White, N.R. Sottos, P.H. Geubelle, J.S.Moore, M.R. Kessler, S.R. Sriram, E.N. Brown, S. Viswanathan: Autonomic healing of polymer composites. *Nature* **409**, 794-797 (2001).

[5] J.D.Rule, S.R. White, N.R. Sottos: Effect of microcapsule size on the performance of self-healing polymers. *Polymer* **48**, 3520-3529 (2007).

[6] Z.G. Wei, R. Sandström, S. Miyazaki: Review: Shape memory materials and hybrid composites for smart systems. Part II: Shape-memory hybrid composies. *Journal of Materials Science* **33**, 3763-3783 (1983).

[7] J. Schrooten, V. Michaud, J. Parthenios, G. Psarras, C. Galiotis, R. Gotthardt, J.-A. Månson, J. Van. Humbeeck: Progress on composites with embedded shape memory alloy wires. *Materials Transactions JIM* **43**, 961-973 (2002).

[8] K.A. Tsoi: Thermomechanical and transformational behaviour and applications of shape memory alloys and their composites. *PhD thesis*, University of Sydney, Sydney, Australia (2002).

[9] J. Schrooten, V. Michaud, Y. Zheng, J.A. Baltá, J.-A. Månson: Shape memory alloy wires turn composites into smart structures. Part 1: Material requirements. *Proc. SPIE* **4698**, 395-405 (2003).

[10] V. Michaud, J. Schrooten, M. Parlinska, R. Gotthardt, J.E. Bidaux: Shape memory alloy wires turn composites into smart structures Part 2: Manufacturing and properties. *Proc. SPIE* **4698**, 406-415 (2003).

[11] C.A. Rogers, C. Liang, S. Li: Active damage control of hybrid material systems using induced strain actuators. *Proc. AIAA 32nd Structures, Structural Dynamics and Materials Conference*, Paper No. AIAA 91-1145-CP, Baltimore, 1190-1203 (1991).

[12] G. Zhou, L.M. Sim, P.A. Brewster, A.R. Giles: Through-the-thickness mechanical properties of smart quasi-isotropic carbon/epoxy laminates. *Composites Part A* **35**, 797-815 (2004).

[13] D.W. Jensen, J. Pascual, J.A. August: Performance of graphite/bismaleimide laminates with embedded optical fibres. Part I: uniaxial tension. *Smart Materials and Stuctures* **1**, 24-30 (1992).

[14] A. Dasgupta, Y. Wan, S. Sirkis: Prediction of resin pocket geometry for stress analysis of optical fibres embedded in laminated composites. *Smart Materials and Structures* **1**, 101-107 (1992).

[15] Y. Okabe, T. Mizutani, S. Yashiro: Detection of microscopic damages in composite laminates with embedded small-diameter fiber Bragg grating sensors. *Composites Science and Technology* **62**, 951-958 (2002).

[16] J. Botsis: Internal strain measurement in polymer composites using FBG sensors, merits and limitations. Internal document, Laboratory of Applied Mechanics and Reliability Analysis, School of Engineering, Swiss Federal Institute of Technology, Lausanne, Switzerland.

[17] H. Tsuda, N. Toyama, K. Urabe, J. Takatsubo: Impact damage detection in CFRP using fiber Bragg gratings. *Smart Materials and Structures* **13**, 719-724 (2004).

[18] H. Tsuda: Ultrasound and damage detection in CFRP using fiber Bragg grating senors. *Composites Science and Technology* **66**, 676-683 (2006).

[19] S.D. Bergman, F. Wudl: Mendable polymers. *Journal of Materials Chemistry* **18**, 41-62 (2008).

[20] M.R. Kessler: Self-healing: a new paradigm in materials design. *Proc. IMechEJ., Part G: Aerospace Engineering* **221**, 479-495 (2007).

[21] R.S. Trask, H.R. Williams, I.P. Bond: Self-healing polymer composites: mimicking nature to enhance performance. *Bioinspired Biomimaterials* **2**, 1-9 (2007).

[22] S.R. White, M.M. Caruso, J.S. Moore: Autonomic Healing of Polymers. *MRS Bulletin* **33**, 766-769 (2008).

[23] R.P. Wool: Self-healing materials: a review. *Soft Matter* **4**, 400-418 (2008).

[24] D.Y. Wu, S. Meure, D. Solomon: Self-healing polymeric materials: A review of recent developments. *Progress in Polymer Science* **33**, 479-522 (2008).

[25] Y.C. Yuan, T. Yin, M.Z. Rong, M.Q. Zhang: Self healing in polymers and polymer composites. Concepts, realization and outlook: A review. *eXPRESS Polymer Letters* **2**, 238-250 (2008).

[26] E.N. Brown, M.R. Kessler, N.R. Sottos, S.R. White: In situ poly(urea-formaldehyde) microencapsulation of dicyclopentadiene. *Journal of Microencapsulation* **20**, 719-730 (2003).

[27] M.W. Keller, N.R. Sottos: Mechanical properties of microcapsules used in a self-healing polymer. *Experimental Mechanics* **46**, 725-733 (2006).

[28] E.N. Brown, S.R. White, N.R. Sottos: Retardation and repair of fatigue cracks in a microcapsule toughened epoxy composite – Part I: Manual Infiltration. *Composites Science and Technology* **65**, 2466-2473 (2005).

[29] E.N. Brown, S.R. White, N.R. Sottos: Retardation and repair of fatigue cracks in a microcapsule toughened epoxy composite – Part II: In situ self-healing. *Composites Science and Technology* **65**, 2474-2480 (2005).

[30] E.N. Brown, S.R. White, N.R. Sottos: Fatigue crack propagation in microcapsule-toughened epoxy. *Journal of Materials Science* **41**, 6266-6273 (2006).

[31] A.S. Jones, J.D. Rule, J.S. Moore, N.R. Sottos, S.R. White: Life extension of self-healing polymers with rapidly growing fatigue cracks. *Journal of the Royal Society Interface* **4**, 395-403 (2007).

[32] B.J. Blaiszik, N.R. Sottos, S.R. White: Nanocapsules for self-healing materials. *Composites Science and Technology* **68**, 978-986 (2008).

[33] J.D. Rule, E.N. Brown, N.R. Sottos, S.R. White, J.S. Moore: Wax-protected catalyst microspheres for efficient self-healing materials. *Advanced Materials* **17**, 205-208 (2005).

[34] J.M. Kamphaus, J.D. Rule, J.S. Moore, N.R. Sottos, S.R. White: A new self-healing epoxy with tungsten (VI) chloride catalyst. *Journal of the Royal Society Interface* **5**, 95-103 (2008).

[35] M.W. Keller, S.R. White, N.R. Sottos: A self-healing poly(dimethyl siloxane) elastomer. *Advanced Functional Materials* **17**, 2399-2404 (2007).

[36] G.O. Wilson, J.S. Moore, S.R. White, N.R. Sottos, H.M. Andersson: autonomic healing of epoxy vinyl esters via ring opening metathesis polyerization. *Advanced Functional Materials* **18**, 44-52 (2008).

[37] M.M. Caruso, D.A. Delafuente, V. Ho, N.R. Sottos, J.S. Moore, S.R. White: Solvent-promoted self-healing epoxy materials. *Macromolecules* **40**, 8830-8832 (2007).

[38] M.M. Caruso, B.J. Blaiszik, S.R. White, N.R. Sottos, J.S. Moore: Full recovery of fracture toughness using a nontoxic solvent-based self-healing system. *Advanced Functional Materials* **18**, 1898-1904 (2008).

[39] S.H. Cho, H.M. Andersson, S.R. White, N.R. Sottos, P.V. Braun: Polydimethylsiloxane-based self-healing materials. *Advanced Materials* **18**, 997-1000 (2006).

[40] T. Yin, M.Z. Rong, M.Q. Zhang, G.C. Yang: Self-healing epoxy composites—Preparation and effect of the healant consisting of microencapsulated epoxy and latent curing agent. *Composites Science and Technology* **67**, 201-212 (2007).

[41] T. Yin, L. Zhou, M.Z. Rong, M.Q. Zhang: Self-healing woven glass fabric/epoxy composites with the healant consisting of micro-encapsulated epoxy and latent curing agent. *Smart Materials and Structures* **17**, 1-8 (2008).

[42] M.R. Kessler, S.R. White: Cure kinetics of the ring-opening metathesis polymerization of dicyclopentadiene. *Journal of Polymer Science Part A* **40**, 2373-2383 (2002).

[43] M.R. Kessler, G.E. Larin, N. Bernklau: Cure characterization and viscosity development of ring-opening metathesis polymerized resins. *Journal of Thermal Analysis and Calorimetry* **85**, 7-12 (2006).

[44] J.D. Rule, J.S. Moore: ROMP reactivity of endo- and exo-dicyclopentadiene. *Macromolecules* **35**, 7878-7882 (2002).

[45] T.C. Mauldin, J.D. Rule, N.R. Sottos, S.R. White, J.S. Moore: Self-healing kinetics and the stereoisomers of dicyclopentadiene. *Journal of the Royal Society Interface* **4**, 389-393 (2007).

[46] E.N. Brown, N.R. Sottos, S.R. White: Fracture testing of a self-healing polymer composite. *Experimental Mechanics* **42**, 372-379 (2002).

[47] E.N. Brown, S.R. White, N.R. Sottos: Microcapsule induced toughening in a self-healing polymer composite. *Journal of Materials Science* **39**, 1703-1710 (2004).

[48] S. Mostovoy, P.B. Crosley, E.J. Ripling: Use of crack-line-loaded specimens for measuring plane-strain fracture toughness. *Journal of Materials* **2**, 661-681 (1967).

[49] M.R. Kessler, S.R. White: Self-activated healing of delamination damage in woven composites. *Composites Part A* **32**, 683-699 (2001).

[50] M.R. Kessler, N.R. Sottos, S.R. White: Self-healing structural composite materials. *Composites Part A* **34**, 743-753 (2003).

[51] C. Dry: Procedures developed for self-repair of polymer matrix composite materials. *Composite Structures* **35** 263-269 (1996).

[52] C.M. Dry, N.R. Sottos: Passive self-smart repair in polymer matrix composite materials. *Proc. SPIE* **1916**, 438-444 (1993).

[53] J.W.C. Pang, I.P. Bond: A hollow fibre reinforced polymer composite encompassing self-healing and enhancing damage visibility. *Composites Science and Technology* **65**, 1791-1799 (2005).

[54] R.S. Trask, I.P. Bond: Biomimetic self-healing of advanced composite structures using hollow glass fibres. *Smart Materials and Structures* **15**, 704-710 (2006).

[55] R.S. Trask, G.J. Williams, I.P. Bond: Bioinspired self-healing of advanced composite structures using hollow glass fibres. *Journal of the Royal Society Interface* **4**, 363-371 (2007).

[56] G. Williams, R. Trask, I. Bond: A self-healing carbon fibre reinforced polymer for aerospace applications. *Composites Part A* **38**, 1525-1532 (2007).

[57] K. Toohey, J.A. Lewis, J.S. Moore, S.R. White, N.R. Sottos: Self-healing materials with microvascular networks. *Nature Materials* **6**, 581-585 (2007).

[58] J.A. Lewis, G.A. Gratson: Direct writing in three dimensions. *Materials Today* **7**, 32-39 (2004).

[59] H.R. Williams, R.S. Trask, I.P. Bond: Self-healing composite sandwich structures. *Smart Materials and Structures* **16**, 1198-1207 (2007).

[60] H.R. Williams, R.S. Trask, I.P. Bond: Self-healing sandwich panels: Restoration of compressive strength after impact. *Composites Science and Technology* **68**, 3171-3177 (2008).

[61] X. Chen, M.A. Dam, K. Ono, A. Mal, H. Shen, S.R. Nutt, K. Sheran, F.A. Wudl: Thermally remendable cross-linked polymeric material. *Science* **295**, 1698-1702 (2002).

[62] X. Chen, F. Wudl, A.K. Mal, H. Shen, S.R. Nutt: New thermally remendable highly cross-linker polymeric materials. *Macromolecules* **36**, 1802-1807 (2003).

[63] S.A. Hayes, F.R. Jones, K. Marshiya, W. Zhang: A self-healing thermosetting composite material. *Composites Part A* **38**, 1116-1120 (2007).

[64] S.A. Hayes, W. Zhang, M. Branthwaite, F.R. Jones: Self-healing of damage in fibre-reinforced polymer matrix composites. *Journal of the Royal Society Interface* **4**, 381-387 (2007).

[65] K. Worden, W.A. Bullough, J. Haywood: Smart Technologies. World Scientific Publishing Co., London (2003).

[66] L.C. Chang, T.A. Read: Plastic deformation and diffusionless phase changes in metals — The gold-cadmium beta phase. *Trans. AIME* **189**, 47-52 (1951).

[67] W.J. Buehler, J.W. Gilfrich, R.C. Wiley: Effect of low-temperature phase changes on the mechanical properties of alloys near composition TiNi. *Journal of Applied Physics* **34**, 1475 (1963).

[68] K.A. Tsoi, J. Schrooten, R. Stalmans: Part I: Thermomechanical characteristics of shape memory alloys. *Materials Science and Engineering Part A* **368**, 286-298 (2004).

[69] Z.G. Wei, R. Sandström, S. Miyazaki: Review: Shape-memory materials and hybrid composies for smart systems. Part I: Shape memory materials. *Journal of Materials Science* **33**, 3743-3762 (1983).

[70] K. Otsuka, X. Ren: Recent developments in the research of shape memory alloys. *Intermetallics* **7**, 511-528 (1999).

[71] K. Otsuka, T. Kakeshita: Science and technology of shape-memory alloys: New developments. *MRS Bulletin* **2**, 91-100 (2002).

[72] J.S. Paine, C.A. Rogers: The effect of thermoplastic composite processing on the performance of embedded nitinol actuators. *Journal of Thermoplastic Composite Materials* **4**, 102-122 (1991).

[73] D.A. Hebda, M.E. Whitlock, J.B. Ditman, S.R. White: Manufacturing of adaptive graphite/epoxy structures with embedded nitinol wires. *Journal of Intelligent Materials Systems and Structures* **6**, 220-228 (1995).

[74] K.D. Jonnalagadda, N.R. Sottos, M.A. Qidwai, D.C. Lagoudas: Transformation of embedded shape memory alloy ribbons. *Journal of Intelligent Materials Systems and Structures* **9**(5), 379-390 (1998).

[75] K.A. Tsoi, R. Stalmans, J. Schrooten: Transformation behaviour of constrained shape memory alloys. *Acta Materialia* **50**, 3535-3544 (2002).

[76] R. Stalmans, K.A. Tsoi, J. Schrooten: The transformational behaviour of shape memory wires embedded in a composite matrix. *Proc. SPIE* **4073**, 88-96 (2000).

[77] Y. Zheng, J. Schrooten, L. Cui, J. Van Humbeeck: Constrained thermoelastic martensitic transformation studied by modulated DSC. *Acta Materialia* **51**, 5467-5475 (2003).

[78] Y. Zheng, L.Cui, D. Zhu, D. Yang: The constrained phase transformation of prestrained TiNi fibres embedded in metal matrix smart structures. *Materials Letters* **43**, 91-96 (2000).

[79] Y.J. Zheng, L.S. Cui, J. Schrooten: Basic design guidelines for SMA/epoxy smart composites. *Materials Science and Engineering Part A* **390**, 139-143 (2005).

[80] Y.J. Zheng, J. Schrooten, K.A. Tsoi, R. Stalmans: Thermal response of glass fibre/epoxy composites with embedded TiNiCu alloy wires. *Materials Science and Engineering Part A* **335**, 157-163 (2002).

[81] K.A. Tsoi, J. Schrooten, Y. Zheng, R. Stalmans: Part II: Thermomechanical characteristics of shape memory alloy composites. *Materials Science and Engineering Part A* **368**, 299-310 (2004).

[82] K. Lau, A.W. Chan, S. Shi, L. Zhou: Debond induced by strain recovery of an embedded NiTi wire at a NiTi/epoxy interface: Micro-scale observation. *Materials and Design* **23**, 265-270 (2002).

[83] A. Kelly: Interface Effects and the Work of Fracture of a Fibrous Composite. *Proceedings of the Royal Society Part A* **319**, 95-116 (1970).

[84] S. Zhandarov, E. Mäder: Characterization of fiber/matrix interface strength: Applicability of different tests, approaches and parameters. *Composites Science and Technology* **65**, 149-160 (2005).

[85] B. Miller, P. Muri, L. Rebenfeld: A microbond method for determination of the shear strength of a fiber/resin interface. *Composites Science and Technology* **28**, 17-32 (1987).

[86] C.T. Chou, U. Gaur, B. Miller: Fracture mechanisms during fiber pull-out for carbon-fiber-reinforced thermosetting composites. *Composites Science and Technology* **48**, 307-316 (1993).

[87] E.J. Chen, J.C. Young: The microdebonding testing system: A method of quantifying adhesion in real composites. *Composites Science and Technology* **42**, 189-206 (1991).

[88] Y.A. Gorbatkina: Adhesive strength in fibre-polymer systems. Ellis Horwood, New York (1992).

[89] G.P. Tandon, N.J. Pagano: Micromechanical analysis of the fiber push-out and re-push test. *Composites Science and Technology* **58**, 1709-1725 (1998).

[90] C.K.Y. Leung, V.C. Li: New strength-based model for the debonding of discontinuous fibres in an elastic matrix. *Journal of Materials Science* **26**, 5996-6010 (1991).

[91] J.A.Nairn: Analytical fracture mechanics analysis of the pull-out test including the effects of friction and thermal stresses. *Advanced Composite Letters* **9**, 373-383 (2000).

[92] C.H. Liu, J.A. Nairn: Analytical and experimental methods for a fracture mechanics interpretation of the microbond test including the effects of friction and thermal stresses. *International Journal of Adhesion Adhesives* **19**, 59-70 (1999).

[93] R.J. Scheer, J.A. Nairn: A comparison of several fracture mechanics methods for measuring interfacial toughness with microbond tests. *Journal of Adhesion* **53**, 45-68 (1995).

[94] C. DiFranca, T.C. Ward. R.O. Claus: The single-fibre pull-out test. 1: Review and interpretation. *Composites Part A* **27**, 597-612 (1996).

[95] J.A. Baltá: Adaptive composites with embedded shape memory alloy wires. *PhD thesis*, Swiss Federal Institute of Technology, Lausanne, Switzerland (2003).

[96] J.S.N. Paine, C.A. Rogers: Characterization of interfacial shear strength between SMA actuators and host composite material in adaptive composite material systems. *Adaptive Structures and Material Systems ASME*, **35**, 63-70, (1993).

[97] K. Jonnalagadda, G.E. Kline, N.R. Sottos: Local displacements and load transfer in shape memory alloy composites. *Experimental Mechanics* **37**(1), 78-86 (1997).

[98] B. Gabry: Topographic study of shape memory alloy wires used as actuators in smart materials. *Journal of Intelligent Systems and Structures* **11**, 592-602 (2000).

[99] K. Lau, W. Tam, X. Meng, L. Zhou: Morphological study on twisted NiTi wires for smart composite systems. *Materials Letters* **57**, 364-368 (2002).

[100] E. Umezaki: Improvement in separation of SMA from matrix in SMA embedded smart structures, *Materials Science and Engineering Part A* **285**, 363-369 (2000).

[101] N.A. Smith, G.G. Antoun, A.B. Ellis, W.C. Crone: Improved adhesion between nickel-titanium shape memory alloy and polymer matrix via silane coupling agents. *Composites Part A* **35**, 1307-1312 (2004).

[102] Z. Chaudhry, C.A. Rogers: Response of composite beams to an internal actuator force. *Journal of Mechanical Design* **114**(3), 343-349 (1992).

[103] J.A. Baltá, J. Simpson, V. Michaud, J.-A. Månson, J. Schrooten: Embedded shape memory alloys confer aerodynamic profile adaptivity. *Smart Materials Bulletin* **12**, 8-12 (2001).

[104] F. Daghia, G. Faiella, V. Antonucci, M. Giordano: Thermomechanical modelling and experimental testing of a shape memory alloy hybrid composite plate. *Advances in Science and Technology* **59**, 41-46 (2008).

[105] J.E. Bidaux, J.-A.E. Månson, R. Gotthardt: Active stiffening of composite materials by embedded shape memory alloy fibres. *Materials Research Society Symposium Proceedings* **459**, 107-117 (1997).

[106] C.A. Rogers: Active vibration and structural acoustic control of shape memory alloy hybrid composites: Experimental results. *Journal of Acoustical Society of America* **88**, 2803-2811 (1990).

[107] D.E. Hodgson: Damping applications of shape-memory alloys. *Materials Science Forum* **394-395**, 69-74 (2002).

[108] I. Schmidt, R. Lammering: Damping behaviour of superelastic NiTi components. *Materials Science and Engineering Part A* **378**, 70-75 (2004).

[109] J.A. Baltá, V. Michaud, M. Parlinska, R. Gotthardt J.-A. Månson: Adaptive composites with embedded NiTiCu wires. *Proc. SPIE* **4333**, *Smart Structures and Materials*, 377-386 (2001).

[110] P. Scherrer, J.E. Bidaux, A. Kim, J.-A.E. Månson, R. Gotthardt: Passive vibration damping in an alpine ski by integration of shape memory alloys. *Journal de Physique IV* **9**, 393-400 (1999).

[111] R. Gotthardt, P. Scherrer, R. Stalmans: *Proc. International Symposium on Shape Memory Materials*. Kanazawa, Japan, 475 (1999).

[112] M. Parlinska, J.A. Baltá, V. Michaud, J.E. Bidaux, J.-A. Månson, R. Gotthardt: Vibrational response of adaptive composites. *Journal de Physique IV* **11**, 129-134 (2001).

[113] R. Gotthardt, M. Parlinska: Vibrational properties of adaptive polymer matrix composites with embedded shape-memory alloy wires. *Materials Science Forum* **394-395**, 475-482 (2002).

[114] A. Shimamoto, H.Y. Zhao, H. Abe: Fatigue crack propagation and local crack-tip strain behaviour in TiNi shape memory fiber reinforced composite. *International Journal of Fatigue* **26**, 533-542 (2004).

[115] A. Shimamoto, H. Ohkawara, F. Nogata: Enhancement of mechanical strength by shape memory effect in Ti Ni fiber-reinforced composites. *Engineering Fracture Mechanics* **71**, 737-736 (2004).

[116] D. Uttamchandani: Fibre-optic sensors and smart structures: developments and prospects. *Electronics and Communication Engineering Journal* **6**(5), 237-246 (1994).

[117] A.D. Kersey: A review of recent developments in fiber optic sensor technology. *Optical Fiber Technology* **2**, 291-317 (1996).

[118] Y.J. Rao: In-fibre Bragg grating sensors. *Measurement Science and Technology* **8**, 355-375 (1997).

[119] Y.L. Lo: Using in-fiber Bragg grating sensors for measuring axial strain and temperature simultaneously on surfaces of structures. *Optical Engineering* **37**, 2272-2276 (1998).

[120] M. Song, S.B. Lee, S.S. Choi, B. Lee: Simultaneous measurement of temperature and strain using two fiber Bragg gratings embedded in a glass tube. *Optical Fiber Technology* **3**, 194-196 (1997).

[121] W.W. Morey, G. Meltz, J.M. Welss: *Proc. 8th International Conference on Optical Fibre Sensors*, Monterey, CA, USA (1992).

[122] B.O. Guan, H.Y. Tam, H.L.W. Chan, C.L. Choy, M. Süleyman Demokan: Discrimination between strain and temperature with a single fiber Bragg grating, *Microwave and Optical Technology Letters* **33**, 200-202 (2002).

[123] M.G. Xu, J.L. Archambault, L. Reekie, J.P. Dakin: Discrimination between strain and temperature effects using dual-wavelength fibre grating sensors. *Electronics Letters* **30**, 1085-1087 (1994).

[124] S.W. James, M.L. Dockney, R.P. Tatam: Simultaneous independent temperature and strain measurements using in-fibre Bragg grating sensors. *Electronics Letters* **32**, 1133-1134 (1996).

[125] O.V. Mazurin, M.V. Streltsina, T.P. Shvaiko-Shavaikoskaya: Handbook of Glass Data. Elsevier Science, Amsterdam (1985).

[126] K. Shima, K. Himeno, T. Sakai, S. Okude, A. Wada, R. Yamauchi: A novel temperature-insensitive long-period fiber grating using a boron-codoped-germanosilicate-core fiber. *OFC '97Technical Digest*, 347-348 (1997).

[127] Y.G. Han, C.S. Kim, K. Oh, U.C. Paek, Y. Chung: *Proc. SPIE* **3746**, 170-173 (1999).

[128] P.M. Cavaleiro, F.M. Araújo, L.A. Ferreira, J.L. Santos, F. Farahi: Simultaneous measurement of strain and temperature using Bragg gratings written in germanosilicate and boron-codoped germanosilicate fibres. *IEEE Photonics Technology Letters* **11**, 1635-1637 (1999).

[129] B.O. Guan, H.Y. Tam, S.L. Ho, W.H. Chung, X.Y. Dong: Simultaneous strain and temperature measurement using a single fibre Bragg grating. *Electronics Letters* **36**, 1018-1019 (2000).

[130] V. Michaud, J.A. Baltá, F. Bosia, J. Botsis, J.-A. Månson: In-situ strain measurement in adaptive composites using fiber Bragg grating sensors. Internal document, Laboratory for Polymer and Composite Technology, Institute of Materials, Swiss Federal Institute of Technology, Lausanne, Switzerland.

[131] H.K. Kang, D.H. Kang, H.J. Bang, C.S. Hong, C.G. Kim: Cure monitoring of composite laminates using fiber optic sensors. *Smart Materials and Structures* **11**, 279-287 (2002).

[132] J.S. Leng, A. Asundi: Real-time cure monitoring of smart composite materials using extrinsic Fabry-Perot interferometer and fiber Bragg grating sensors. *Smart Materials and Structures* **11**, 249-255 (2002).

[133] H.T. Hahn: Effects of residual stresses in polymer matrix composites. *Journal of the Astronautical Sciences* **32**, 253-267 (1984).

[134] M.J. O'Dwyer, G.M. Maistros, S.W. James, R.P. Tatam, I.K. Partridge: Relating the state of cure to the real-time internal strain development in a curing composite using in-fibre Bragg gratings and dielectric sensors. *Measurement Science and Technology* **9**, 1153-1158 (1998).

[135] N. Takeda, S. Ogihara: Initiation and growth of delamination from the tips of transverse cracks in CFRP cross-ply laminates. *Composites Science and Technology* **52**, 309-318 (1994).

[136] G. Zhou, L.M. Sim: Damage detection and assessment in fibre-reinforced composite structures with embedded fibre optic sensors — Review. *Smart Materials and Structures* **11**, 925-939 (2002).

[137] Y. Okabe, S. Yashiro, T. Kosaka, N. Takeda: Detection of transverse cracks in CFRP composites using embedded fiber Bragg grating sensors. *Smart Materials and Structures* **9**, 832-838 (2000).

[138] Y. Okabe, R. Tsuji, N. Takeda: Application of chirped fiber Bragg grating sensors for identification of crack locations in composites. *Composites Part A* **35**, 59-65 (2004).

[139] H. Tsutsui, A. Kawamata, T. Sanda, N. Takeda: Detection of impact damage of stiffened composite panels using embedded small-diameter optical fibres. *Smart Materials and Structures* **13**, 1284-1290 (2004).

[140] S. Takeda, S. Minakuchi, Y. Okabe, N. Takeda: Delamination monitoring of laminated composites subjected to low-velocity impact using small-diameter FBG sensors. *Composites Part A* **36**, 903-908 (2005).

[141] W.W. Morey, G. Meltz, W.H. Glenn: Fiber Bragg grating sensors. *Proc. SPIE* **1169**, Fiber Optic and Laser Sensors VII, 98-107 (1989).

[142] W.W. Morey, J.R. Dunphy, G. Meltz: Multiplexing fiber Bragg grating sensors. *Proc. SPIE* **1586**, Distributed and Multiplexed Fiber Optic Sensors, 216-224 (1991).

[143] G. Wild, S. Hinckley: Acousto-ultrasonic optical fiber sensors: Overview and state-of-the-art. *IEEE Sensors Journal* **8**, 1184-1193 (2008).

[144] B. Culshaw, G. Thursby, D. Betz, B. Sorazu: The detection of ultrasound using fiber-optic sensors. *IEEE Sensors Journal* **8**, 1360-1367 (2008).

[145] D.C. Betz, G. Thursby, B. Culshaw, W.J. Staszewski: Acoutso-ultrasonic sensing using fiber Bragg gratings. *Smart Materials and Structures* **12**, 122-128 (2003).

[146] D.C. Betz, G. Thursby, B. Culshaw, W.J. Staszewski: Identification of structural damage using multifunctional Bragg grating sensors: I. Theory and implementation. *Smart Materials and Structures* **15**, 1305-1312 (2006).

[147] D.C. Betz, G. Thursby, B. Culshaw, W.J. Staszewski: Structural damage identification using multifunctional Bragg grating sensors: II. Damage detection results and analysis. *Smart Materials and Structures* **15**, 1313-1322 (2006).

[148] H. Tsuda, J.-R. Lee: Strain and damage monitoring of CFRP in impact loading using a fiber Bragg grating sensor system. *Composites Science and Technology* **67**, 1353-1361 (2007).

[149] J.-R. Lee, H. Tsuda, N. Toyama: Impact wave and damage detections using a strain-free fiber Bragg grating ultrasonic receiver. *NDT&E International* **40**, 85-93 (2007).

[150] S.S. Kessler, S.M. Spearing, C. Soutis: Damage detection in composite materials using Lamb wave methods. *Smart Materials and Structures* **11**, 269-278 (2002).

[151] N. Takeda, Y. Okabe, J. Kuwahara, S. Kojima, T. Ogisu: Development of smart composite structures with small-diameter fiber Bragg grating sensors for damage detection: Quantitative evaluation of delamination length in CFRP laminates using Lamb wave sensing. *Composites Science and Technology* **65**, 2575-2587 (2005).

[152] K. Diamanti, C. Soutis, J.M. Hodgkinson: Piezoelectric transducer arrangement for the inspection of large composite structures. *Composites Part A* **38**, 1211-1130 (2007).

[153] E.N. Brown: Fracture and fatigue of a self-healing polymer composite material. *PhD thesis*, University of Illinois at Urbana-Champaign, Illinois, USA (2003).

[154] R.H. Grubbs: Handbook of Metathesis. Wiley-VCH, Germany (2003).

[155] P. Schwab, R.H. Grubbs, J.W. Ziller: Synthesis and Applications of $RuCl_2(=CHR')(PR_3)_2$: The Influence of the Alkylidene Moiety on Metathesis Activity. *Journal of the American Chemical Society* **118**(1), 100110 (1996).

[156] C.W. Macosco: RIM, Fundamentals of Reaction Injection Molding. Wiley-VCH, New York (1989).

[157] A.S. Jones, J.D. Rule, J.S. Moore, S.R. White, N.R. Sottos: Catalyst morphology and dissolution kinetics of self-healing polymers. *Chemistry of Materials* **18**, 1312-1317 (2006).

[158] R. Stalmans, V. Michaud, J.E. Bidaux, R. Gotthardt, J.-A. Månson: Adaptive composites with embedded shape memory alloy wires. *Proc. 4th European Conference on Smart Structures and Materials*, 801-804 (1998).

[159] S.R. Sriram: Development of self-healing polymer composites and photoinduced ring opening metathesis polymerization. *PhD thesis*, University of Illinois at Urbana-Champaign, Illinois, USA (2002).

[160] J. Verrey: Resin transfer moulding of complex shaped composites using carbon fibre non-crimp fabrics. *PhD Thesis*, Swiss Federal Institute of Technology, Lausanne, Switzerland (2004).

[161] V. Michaud, J.-A. Månson: Progress on processing and design of composites with embedded shape memory alloy wires. *Transactions of the Materials Research Society of Japan* **29**(7), 3043-3048 (2004).

[162] Y. Xu, K. Otsuka, H. Nagai, H. Yoshida, M. Asai, T. Kishi: A SMA/CFRP hybrid composite with damage suppression effect at ambient temperature. *Scripta Materialia* **49**, 587-593 (2003).

[163] V. Michaud, J. O'Keane, E. Kirkby, R. de Oliveira, J.-A. Månson: Low temperature moulding of adaptive composites with embedded shape memory alloy wires. *Proceedings ICCM*, Paper number 1719 (2008).

[164] H. Cox: The elasticity and strength of paper and other fibrous materials. *British Journal of Applied Physics* **3**, 72-79 (1952).

[165] D.-A. Mendels, Y. Leterrier, J.-A. Månson: Stress transfer model for single fibre and platelet composites. *Journal of Composite Materials* **33**, 1525-1543 (1999).

[166] D.-A. Mendels, Y. Leterrier, J.-A. Månson: The influence of internal stresses on the microbond test I: Theoretical analysis. *Journal of Composite Materials* **36**, 347-363 (2002).

[167] D.-A. Mendels, Y. Leterrier, J.-A. Månson: The influence of internal stresses on the microbond test II: Physical aging and adhesion. *Journal of Composite Materials* **36**, 1655-1676 (2002).

[168] J.C. Salamone: Polymeric Materials Encyclopedia. Bausch & Lomb, Rochester, New York.

[169] H. Lamb: On waves in an elastic plate. *Proceedings of the Royal Society, London* **93**, 114-128 (1917).

[170] J. Rose: Ultrasonic waves in solid media. Cambridge University Press, Cambridge. (1999).

[171] A. Tobias: Acoustic-emission source location in two dimensions by an array of three sensors. *Non-destructive testing* **9**, 9-12 (1976).

[172] T. Kundu, S. Das, K.V. Jata: Point of impact prediction in isotropic and anisotropic plates from the acoustic emission data. *Journal of the Acoustical Society of America* **122**, 2057-2066 (2007).

[173] T. Kundu, S. Das, S.A. Martin, K.V. Jata: Locating point of impact in anisotropic fiber reinforced composite plates. *Ultrasonics* **48**, 193-201 (2008).

[174] H. Jeong, Y.S. Jang: Wavelet analysis of plate wave propagation in composite laminates. *Composite Structures* **49**, 443-450 (2000).

[175] L. Wang: Elastic wave propagation in composites and least-squares damage localization technique. *Master thesis*, North Carolina State University, Raleigh, North Carolina (2004).

[176] P.T. Coverley, W.J. Staszewski: Impact damage location in composite structures using optimized sensor triangulation procedure. *Smart Materials and Structures* **12**, 795-803 (2003).

[177] M.G. Baxter, R. Pullin, K.M. Holford, S.L. Evans: Delta T source location for acousting emission. *Mechanical Systems and Signal Processing* **21**, 1512-1520 (2007).

[178] H. Yamada, Y. Mizutani, H. Nishino, M. Takemoto, K. Ono: Lamb wave source location of impact on anisotropic plates. *Journal of Acoustic Emission* **18**, 51-60 (2000).

[179] D.C. Betz, G. Thursby, B. Culshaw, W.J. Staszewski: Structural damage location with fiber Bragg grating rosettes and Lamb waves. *Structural Health Monitoring* **6**, 299-308 (2007).

[180] K.F. Graff: Wave motion in elastic solids. Universities Press, Belfast (1975).

[181] W.H. Prosser: The propagation characteristics of the plate modes of acoustic emission waves in thin aluminium plates and thin graphite/epoxy composite plates and tubes. *PhD thesis*, The Johns Hopkins University, Baltimore, Maryland (1991).

[182] J.W. Whitney: Structural analysis of laminated anisotropic plates. Technomic Publishing Co., Lancaster (1987).

[183] J.-M. Berthelot: Materiaux composites, comportement mecanique et analyse des structures. Masson, Paris (1992).

[184] H. Suzuki, T. Kinjo, Y. Hayashi, M. Takemoto, K. Ono, Appendix by Y. Hayashi: Wavelet Transform of Acoustic Emission Signals. *Journal of Acoustic Emission* **14**(2), 69-84 (1996).

[185] C.K. Chui: An introduction to wavelets. Academic Press, San Diego (1992).

[186] K.H. Ip, P.W. Tse, H.Y. Tam: Extraction of patch-induced Lamb waves using a wavelet transform. *Smart Materials and Structures* **13**, 861-872 (2004).

[187] H. Jeong: Analysis of plate waves propagating in aniostropic laminates using a wavelet transform. *NDT&E International* **34**, 185-190 (2001).

[188] K. Kishimoto, H. Inoue, M. Hamada, T. Shibuya: Time frequency analysis of dispersive waves by means of wavelet transform. *Journal of Applied Mechanics* **62**, 841-846 (1995).

[189] S.W. Tsai, H.T. Hahn: Introduction to Composite Materials. Technomic Publishing Co., Lancaster (1980).